ABSTRACT

Title of Dissertation / Thesis: **FAILURE PREDICTION OF WIRE BONDS DUE TO FLEXURE**

Karumbu Nathan Meyyappan, Ph.D., 2004

Dissertation / Thesis Directed By: **Associate Professor Patrick McCluskey, Department of Mechanical Engineering**

Solid state power modules are subjected to harsh environmental and operational loads. Identifying the potential design weakness and dominant failure mechanisms associated with the application is very critical to designing such power modules. Failure of the wedge-bonded wires is one of the most commonly identified causes of failures in power modules. This can occur when wires flex in response to a thermal cycling load. Since the heel of the wire is already weakened due to the ultrasonic bonding process, the flexing motion is enough to initiate a crack in the heel of the wire. Owing to the prevalence of this failure mechanism in power modules, a generalized first-order physics-of-failure based model has been developed to quantify these flexural/bending stresses. A variational calculus approach has been employed to determine the minimum energy wire profiles. The difference in curvatures corresponding to the wire profiles before and after thermal cycling provide the flexural stresses. The stresses/strains determined from the load transformation model are then used in a damage model to determine the cycles to failure. The model has been validated against temperature cycling test results. The effects

of residual stresses, that are introduced during the loop formation, (on the thermal cycling life) of these wires also has been studied.

It is believed that the ultrasonic wirebonding process renders the wires weaker at the heel. Efforts have been made to simulate the wirebonding mechanism using Finite element analysis. The key parameters that influence the wirebonding process are identified. Flexural stresses are determined for various heel cross-sectional profiles that correspond to different bond forces.

Additional design constraints may prevent some of the wedge-bonded wires from being aligned parallel to the bond pads. The influence of having the bond pads with a non-zero width offset has been studied through finite element simulations. The 3D minimum energy wire profiles used in the modeling has been obtained through a new energy minimization based model.

FAILURE PREDICTION OF WIRE BONDS DUE TO FLEXURE

By

Karumbu Nathan Meyyappan

Thesis or Dissertation submitted to the Faculty of the Graduate School of the
University of Maryland, College Park, in partial fulfillment
of the requirements for the degree of
Doctor of Philosophy
2004

Advisory Committee:
Associate Professor Patrick McCluskey, Chair
Prof. Michael Pecht
Prof. Sung Lee
Associate Professor Bongtae Han
Assistant Professor Donald Robbins

© Copyright by
Karumbu Nathan Meyyappan
2004

Dedication

To my

Wife and my Parents

Acknowledgements

First and foremost I would like to thank my advisor, mentor and well wisher, Dr. Patrick McCluskey. Without his able support, advice and encouragement this research might have not materialized. I deeply appreciate his efforts to take time off his busy schedule to set me on the right path. I am also deeply indebted to Dr. Don Robbins for his invaluable suggestions and guidance. I would also like to thank my other committee members, Dr. Bongtae Han, Prof. Sung Lee and Prof. Michael Pecht for evaluating my work and also providing invaluable suggestions. In addition, I would also like to thank Prof. Abhijit Dasgupta for some of the lively discussions and the invaluable suggestions in refining the work.

I would also like to thank the over 30 members of the CALCE Electronic Products and Systems Consortium for their support of this research and particularly Grundfos Management A/S for its technical and financial leadership. Special thanks to Peter Hansen at Grundfos A/S for providing continuous feedback and suggestions in this research. I would also like to express my gratitude to Mr. Zeke Topolosky and Mr. Witaly Zeiler for their assistance with some of the validation testing.

Special thanks to all my friends and colleagues, Manikandan Ramasamy, Ragunath Sankaranarayanan, Kaushik Ghosh, Seungmin Cho, Ron DiSabatino, Yunqi Zheng, Vidyasagar Shetty, Sudhir Kumar, Shirish Gupta, Anshul Shrivastava, Casey O'Connor, Arvind Chandrasekharan, Keith Rogers, Sanjay Tikku etc. etc. for all their help and support during my stay here. Another person who deserves special acknowledgement is my late friend, Swaminathan Gowrisankaran, who has been very

instrumental in the work. I still remember those wonderful days when we used to have inspiring discussions related to the thesis.

Most of all I specially wish to thank my wife, Nagalaxmi, and my parents for supporting me all through these years and also giving me able support and comfort when I needed them most.

Table of Contents

Dedication ii

Acknowledgements iii

Table of Contents v

List of Tables viii

List of Figures ix

Chapter 1: Introduction and Literature Review 1
- 1.1 Background 1
- 1.2 Wirebonding in Microelectronics 4
- 1.3 Wire Material 7
- 1.4 Ultrasonic Wedge Bonding of Aluminum Wires 8
- 1.5 Failure Mechanism 12
- 1.6 Virtual Qualification 15
- 1.7 Scope of the Current Thesis 17
- 1.8 Nomenclature and Terminology used 18

Chapter 2: Wire Flexure Failure and Life Prediction Models 23
- 2.1 Review of existing Fatigue Models and Limitations 24
- 2.2 Load Transformation Model 25
  - 2.2.1 Wire Loop Profile 28
  - 2.2.2 Hermite Polynomial to represent the Wire Profile 29
  - 2.2.3 Cubic Spline to represent the Wire Loop Profile 31
- 2.3 Residual Stresses during Loop Formation 36
  - 2.3.1 Inelastic Bending of Curved Beams 36
  - 2.3.2 Residual Stresses in a Curved Beam 40
  - 2.3.3 Residual Stresses for a Sample Wire Profile 42
- 2.4 Damage Model 46
  - 2.4.1 Effect of Residual Stresses on the Fatigue Life 46
  - 2.4.2 Stress Based Life Approach 47
  - 2.4.3 Strain Based Approach to Total Life 49

Chapter 3: Assumptions and Validation Studies 53
- 3.1 Introduction 53
- 3.2 FE Validation of the Energy Based Approach 53
- 3.3 Thermal Cycling Tests 55
  - 3.3.1 Comparison with the Analytical Model 57
- 3.4 Sensitivity Analysis 58

3.4.1 Effect of Wire Length on the Wire Life ... 59
3.4.2 Effect of Bond Pad Height ... 61
3.4.3 Effect of Wire Span ... 63
3.4.4 Effect of Wire Thickness ... 64
3.4.5 Effect of Thermal Load ... 65
3.5 Significance of Frame Displacement ... 66
3.5.1 Effect of Frame Displacements on the Flexural Stresses ... 69
3.5.2 Effect of CTE on the Heel Stresses in the Wire ... 70
3.6 Model Assumptions ... 76
3.6.1 Further Limitations, if using the Hermite Interpolation Scheme ... 78
3.6.2 Disadvantages of the CUBIC Interpolation Scheme ... 80

Chapter 4: Ultrasonic Bonding and its Effect on Wire Flexural Failure ... 81
4.1 Introduction ... 81
4.2 Ultrasonic Bonding Mechanism ... 82
4.3 Bond Formation Patterns ... 86
4.4 Wire Bond Process Parameters ... 88
4.5 Wire Properties when subjected to Ultrasonic Energy ... 90
4.6 Effect of Tool Shape on Wedge Bonding ... 93
4.7 Wire Deformation and its Effect on Flexural Stresses ... 98
4.8 Effect of Wire Deformation on the Wire Fatigue Model ... 108

Chapter 5: Effect of Wire Twisting ... 111
5.1 Loop Profile ... 112
5.1.1 Minimization of Strain Energy of the Cubic Spline ... 116
5.2 Case Study ... 120

Chapter 6: Contributions and Suggestions for Future Work ... 135
6.1 Major Accomplishments ... 135
6.2 Suggestions for Future Work ... 138
6.2.1 Effect of Wire Heating ... 138
6.2.2 Effect of Silicone Gel Encapsulant ... 138
6.2.3 Plastic Deformation of the Wire ... 139
6.2.4 Wire Twisting with no Constraints in the Three Dimensional Plane ... 140
6.2.5 Determination of Optimum Wirebonding Process Parameters ... 140
6.2.6 Characterization of Wire Material Properties for Low Cycle Fatigue ... 141

Appendix A ... 142
A.1 Frame Displacement Model ... 142

Appendix B ... 146
B.1 Derivation of Wire Loop Profile using a Cubic Spline ... 146

Appendix C ... 150
C.1 Simple Cubic Spline Model ... 150
C.1.1 Location of Reference Point in Wire Geometry ... 150

Appendix D 154
D.1 Modeling a Reliable Wirebonded Interconnection 154
D.1.1 Imposed Constraints... 154
D.1.1 Wire Flexural Stresses 155

References.. 158

List of Tables

Table 4-1 Tool dimensions 90

Table D-1Upper and lower bounds of geometric parameters.. 155

List of Figures

Figure 1-1 Hybrid power modules 2

Figure 1-2 Schematics of power module 3

Figure 1-3 Critical failure sites in a typical power module 4

Figure 1-4 Wires bonded in different years 5

Figure 1-5 Ball bond 6

Figure 1-6 Wedge bond 6

Figure 1-7 Wire selection chart 8

Figure 1-8 Ultrasonic bonding process 9

Figure 1-9 Ultrasonic wedge tool 10

Figure 1-10 Unidirectional wire bonds in a hybrid power module 10

Figure 1-11 Wires bonded with twist in hybrid power modules 11

Figure 1-12 View of the wire bond near the heel 11

Figure 1-13 IC failures 12

Figure 1-14 Wire heel crack 14

Figure 1-15 Failure of wire near the heel for a twisted wire 15

Figure 1-16 Terminology used 22

Figure 2-1 Typical power module 23

Figure 2-2 Wire label definitions 27

Figure 2-3 Rectangular beam in bending 37

Figure 2-4 Finite element simulation of deformation 39

Figure 2-5 Stress distribution across fibers 40

Figure 2-6 Curved bar in pure bending 41

Figure 2-7 Wire profile 43

Figure 2-8 Curvature plot.. 44

Figure 2-9 Shift of neutral axis 44

Figure 2-10 Residual stress plot in the wire.. 45

Figure 2-11 S-N curve for a 15 mil wire.. 48

Figure 2-12 Strain amplitude vs. cycles to failure 51

Figure 2-13 Flowchart of model 52

Figure 3-1 Deformed wire profile from energy-based model and FE 54

Figure 3-2 Module with the bond # shown 55

Figure 3-3 Thermal cycling load profile 56

Figure 3-4 Heel crack failure in wire #9 after 1125 cycle 56

Figure 3-5 Comparison of output from model and experiment 58

Figure 3-6 Effect of wire length on wire life (H=3.5 mm) 59

Figure 3-7 Cycles to failure for various wire lengths (lower bond pad).......................... 60

Figure 3-8 Cycles to failure for various wire Lengths (upper bond pad) 61

Figure 3-9 Wire profiles for varying bond pad height offset.. 62

Figure 3-10 Cycles to failure at the upper bond pad.. 63

Figure 3-11 Effect of wire span on wire life (upper bond pad) 64

Figure 3-12 Effect of wire thickness... 65

Figure 3-13 Effect of stepwise increase in temperature.. 66

Figure 3-14 Finite element mesh 67

Figure 3-15 Displacement contour... 68

Figure 3-16 Frame displacements at the various lead numbers 69

Figure 3-17 Frame displacement model 71

Figure 3-18 Heel stresses 71

Figure 3-19 Wire heel stresses at the upper bond pad for various frame CTE's. 74

Figure 3-20 Bending stresses at the wire heel for various frame CTE's 75

Figure 3-21 Variation in model output due to variation of top point definition 79

Figure 3-22 Life of wire dependent on wire span length 79

Figure 4-1 Ultrasonic transducer 82

Figure 4-2 Stress vs. elongation for aluminum crystals 84

Figure 4-3 Bond pad lift-off pattern for non-optimized process parameters 87

Figure 4-4 Bond wedge profile 89

Figure 4-5 Wedge groove profile for large bonding wires 89

Figure 4-6 Stress-strain curves at room and high temperature 92

Figure 4-7 Modulus at various temperatures 92

Figure 4-8 Finite element simulation of contact between wire and pad 93

Figure 4-9 Displacement contour for the 60 V-groove tool 95

Figure 4-10 60° groove angle 96

Figure 4-11 50° groove Angle 96

Figure 4-12 70° Groove angle 97

Figure 4-13 90° Groove angle 97

Figure 4-14 Wedge bonding for fine pitch applications 98

Figure 4-15 Front view of the cross-sectioned wire 99

Figure 4-16 Top view of the cross-sectioned wire 100

Figure 4-17 3D Finite element model of the tool-wire-pad 101

Figure 4-18 Deformed wire profile 103

Figure 4-19 Bending stress distribution in the wire 105

Figure 4-20 Bending stresses near the upper bond pad 105

Figure 4-21 Wire deformation for various tool displacements 107

Figure 4-22 B/2r for various tool displacements 107

Figure 4-23 Flexural stress for various B/2r 108

Figure 4-24 Thermal cycling results revalidated 110

Figure 5-1 Twisted wires 111

Figure 5-2 Critical regions in a twisted wire 112

Figure 5-3 Wire profile with parameters 114

Figure 5-4 Wire profile for D=20, H=10 and W=2 119

Figure 5-5 Wire loop profile on the two dimensional plane 122

Figure 5-6 Three dimensional wire loop profile 122

Figure 5-7 Deformed wire profile with boundary conditions 124

Figure 5-8 Maximum stresses near the heel for a wire with zero width offset 125

Figure 5-9 Maximum bending stresses at the heel 126

Figure 5-10 Curvature at the heel of the wire 127

Figure 5-11 Sections of wire where stresses are plotted 128

Figure 5-12 Stresses at cross section of wire away from the heel 129

Figure 5-13 Location of neutral plane for width offset 0 mm 130

Figure 5-14 Location of neutral plane for width offset 8 mm 131

Figure 5-15 Stresses at nodes on the top side of wire 131

Figure 5-16 Stresses at nodes on the bottom side of wire 132

Figure 5-17 Stresses at nodes on the left side of the wire 133

Figure 5-18 Stresses at nodes on the right side of the wire 133

Figure 6-1 Cycles to failure with/without gel 139

Figure A- 1 Frame geometry parameters 142

Figure A-2 Bowing of frame 143

Figure B-1 Wire loop profile parameters 146

Figure C-1 Location of reference point for varying wire lengths 152

Figure C-2 Location of reference point for varying bond height offsets 152

Figure D-1 Flexural stress for height offset of 3 mm 156

Figure D-2 Flexural stresses for various height offsets 157

Chapter 1: Introduction and Literature Review

1.1 Background

Solid-state power modules are incorporated in a variety of electronic products where they are typically used for power control/adjustment. Understanding and controlling the reliability of such power modules under harsh environments, is one of the challenges facing designers. Such knowledge is essential for maximizing performance and minimizing life cycle cost.

Figure 1-1 shows two typical power modules. Figure 1-2 shows a schematic of a power module in cross-section with all the salient features labeled. These power modules typically contain a silicon die, direct bonded copper substrate, high lead solder and wire bonds. The die is attached to the direct bonded copper substrate using high lead solder.

The attachment material, high lead solder, serves mechanical, electrical, and thermal functions [Pecht, 1991]. Direct bonded copper refers to the process of bonding copper film to a ceramic substrate at a very high temperature between 1065-1085°C such that a very secure bond is formed by a copper oxide - aluminum oxide eutectic joint. The DBC ensures electrical insulation while providing thermal conduction. One other common feature in these high power devices is the wirebonding interconnection. Due to the high current passed through these devices, thick aluminum wires varying from 5-15 mil in diameter are typically used in such applications. Some of the power modules also have a compliant coating of silicone gel, used to protect the die from moisture and the package from vibration.

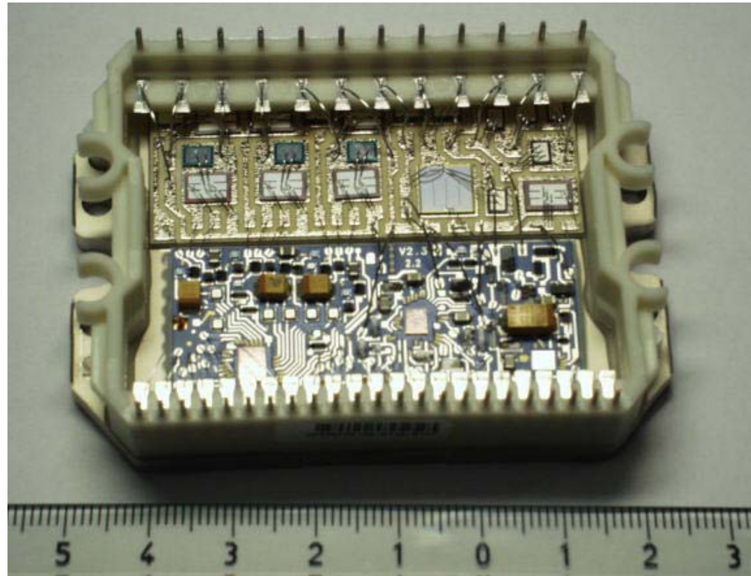

Courtesy: Grundfos A/S

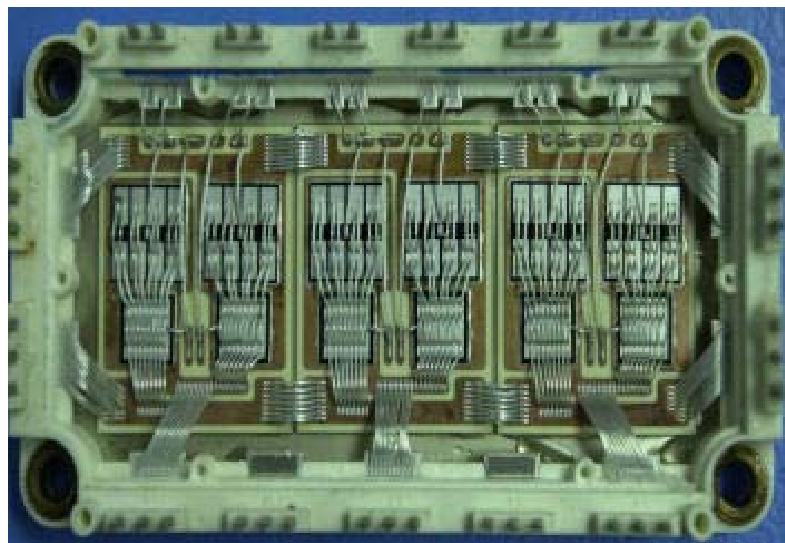

Courtesy: Eupec Inc.

Figure 1-1 Hybrid power modules

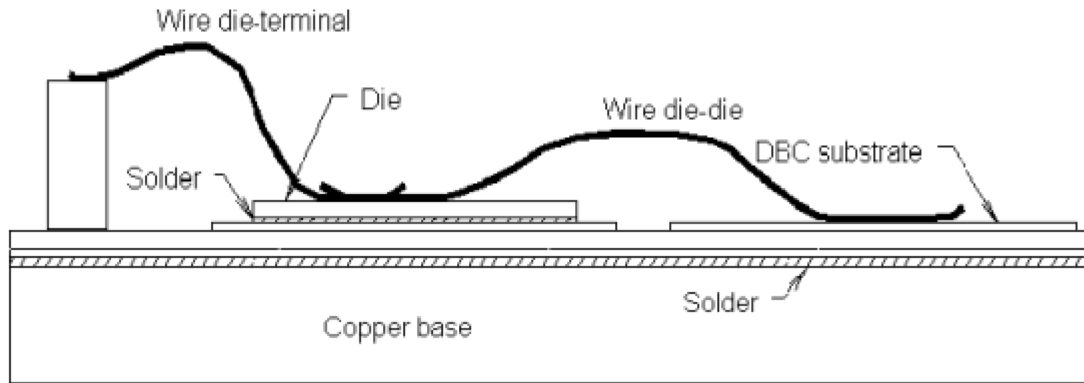

Figure 1-2 Schematics of power module

The environmental and operational loads place severe thermo-mechanical stresses on these devices. One of the critical phases in the design would be to identify the design weaknesses and dominant failure mechanisms associated with the application. Some of the critical failure sites (Figure 1-3) identified in such a power module are

- Cracking of the DBC substrate
- Delamination of the copper from the DBC substrate
- Failure of bond wires at the heel
- Failure of bond wires near the frame
- Failure of bond wires near the die pad
- Fatigue failure of the Die/Substrate attach

Thermal cycling of DBC substrates can cause debonding of the copper surface from the ceramic. Tests have revealed that cracks initiate at the outside edges of the copper foils, coalesce around the entire perimeter of the foil, and then work their way in along the interface [Yoshino, 1992, Mikkelsen, 2001]. The coefficient of thermal expansion mismatch between the different layers coupled with the thermal cycling environment can also cause weakening of the solder joints. However, the predominant

failure site observed in these power modules is the fatigue failure of the bond wires [Hu et al., 1991]. Also, thermal cycling of field samples revealed wire bond failures as the dominant failure mechanism.

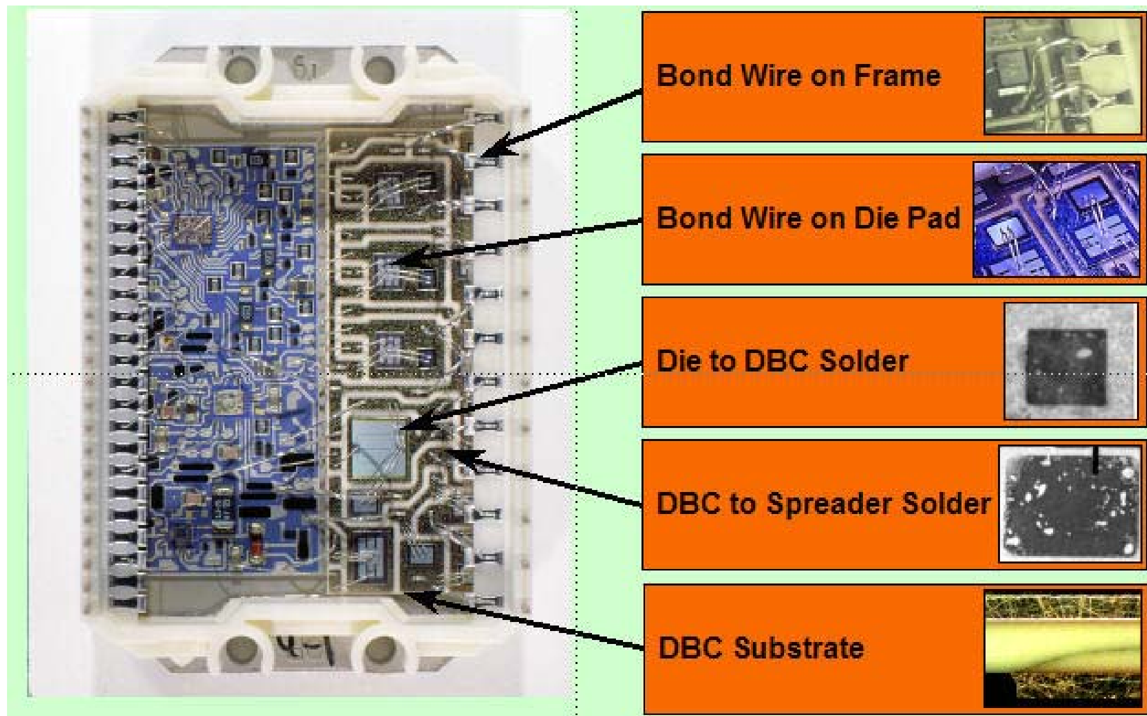

Figure 1-3 Critical failure sites in a typical power module

1.2 Wirebonding in Microelectronics

Wire bonding today is used throughout the microelectronics industry as a means of interconnecting bond pads on the die to the internal lands of package leadframes or bond pads on a substrate using thin wire and a combination of heat, pressure and/or ultrasonic energy. Wire bonding continues to be the dominant bonding technologies in industry. It was estimated in 1996 that about 4×10^{12} wires were bonded per year

[Harman 1997]. Figure 1-4 shows the number of wires bonded between the years 1984-98.

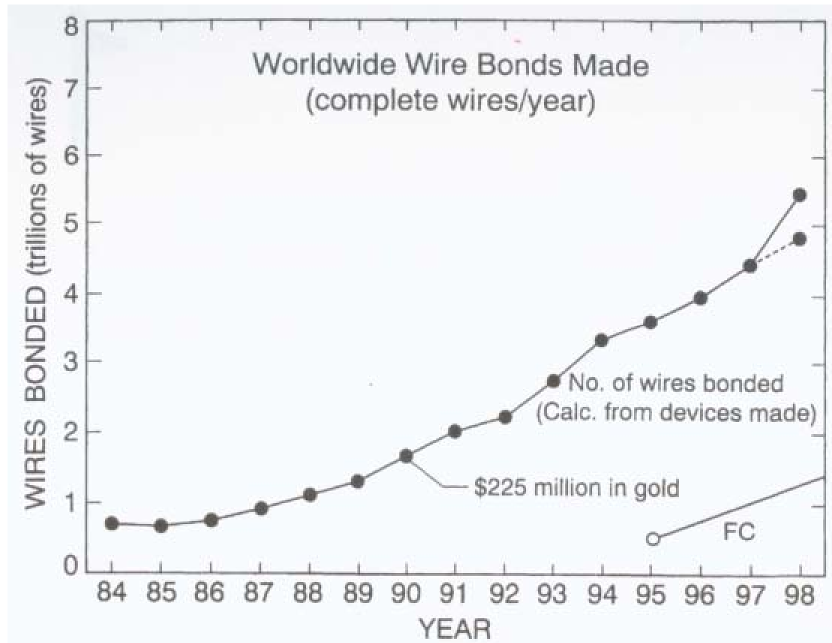

Source: Harman, "Wirebonding in Microelectronics"
Figure 1-4 Wires bonded in different years

Wirebonds are of two forms (viz. ball or wedge bond) as shown in Figure 1-5 and Figure 1-6, respectively. About 90% of all electronic packages and assemblies are produced using gold ball bonds while about 10% are produced with wedge bonds. Ball bonding facilitates smaller bond pads, smaller pitch and hence a very high I/O, very desirable in the semiconductor industry.

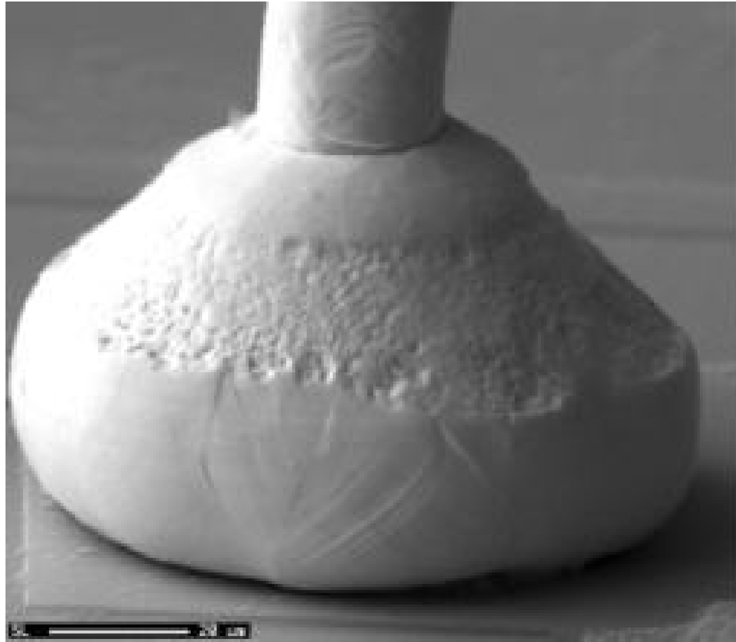

Source: Chandrasekaran, A., “Effect of mold compound on Au-Al wirebond-bond pad intermetallic formation”, Masters Thesis 2004, University of Maryland-College Park

Figure 1-5 Ball bond

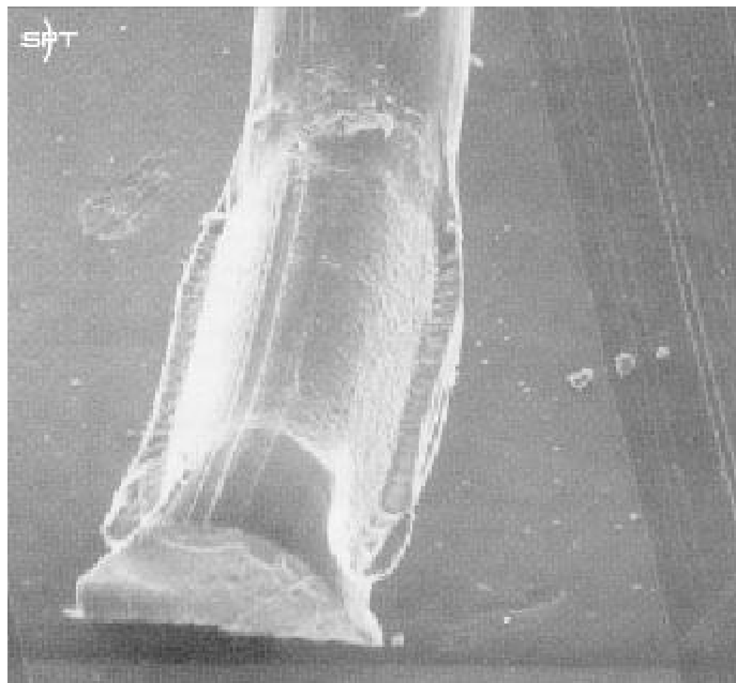

Source: Small Precision tool, Large Wire bonding tools Catalog, Revised 02-96-3

Figure 1-6 Wedge bond

For high power devices, however, thick aluminum wires are needed to carry the larger currents. These wires can only be wedge-bonded.

Ultrasonic (Wedge-Wedge) bonding is done at room temperature with the application of ultrasonic energy. A temperature rise has been reported due to the ultrasonic bonding process. However, these temperature rise have been attributed mainly due to non-optimized bonding parameters, discussed in Chapter 4.

This is in contrast to the technologies used widely for gold wire bonding. Thermo-compression (Ball-Stitch) bonding is done at a very high temperature with the application of heat and thermosonic (suited for Ball-Stitch) bonding is done at around 100-150°C along with the ultrasonic energy.

Henceforth, the discussions would be limited to ultrasonically wedge bonded aluminum wires.

1.3 Wire Material

Al wires are classified as fine wires (0.7 –3 mil) and the heavy wires used on power modules (> 3 mil) based on the thickness as shown in Figure 1-7 [Kulicke & Soffa, 2003]. Al as such is not used in its pure form since it is too soft to be drawn into a small wire. Al is often alloyed with 1% Si or 1% Mg to increase its strength. Si is not in a solid solution below ~500°C. It appears as finely divided particles and tends to grow with heat treatment. These can act as stress raisers. 1% Mg added to the Al wire stays in solid solution at room temperature and hence has better fatigue resistance. However, for heavy Al wires high purity Al, either 4-nine or 5-nine (99.99, 99.999% pure), with small

amounts of titanium, copper or other elements are commonly used [Held et al., 1999]. These wires are supplied in the annealed condition [Harman, 1997].

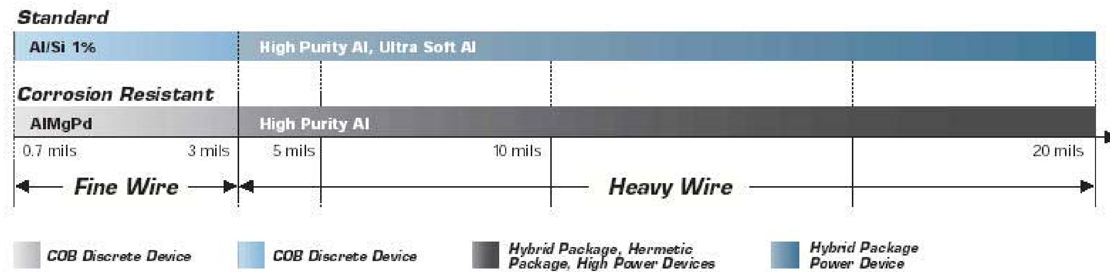

Source: Bonding Wire Products Catalogue, Kulicke and Soffa
Figure 1-7 Wire selection chart

1.4 Ultrasonic Wedge Bonding of Aluminum Wires

Figure 1-8 illustrates the steps involved in a wedge-wedge ultrasonic bond. A typical wedge bonding tool used in the operation is shown in Figure 1-9. The illustration helps us better understand the bonding mechanism, which is crucial in studying the reliability of wedge-bonded wires. After creating the first ultrasonic bond between the aluminum wire and the aluminum pad, the tool moves the wire to form a loop, ending at the next bond pad. The tool then comes down and ultrasonically welds the aluminum wire to the second pad. The tool then clamps the wire and pulls up, breaking the wire at the heel.

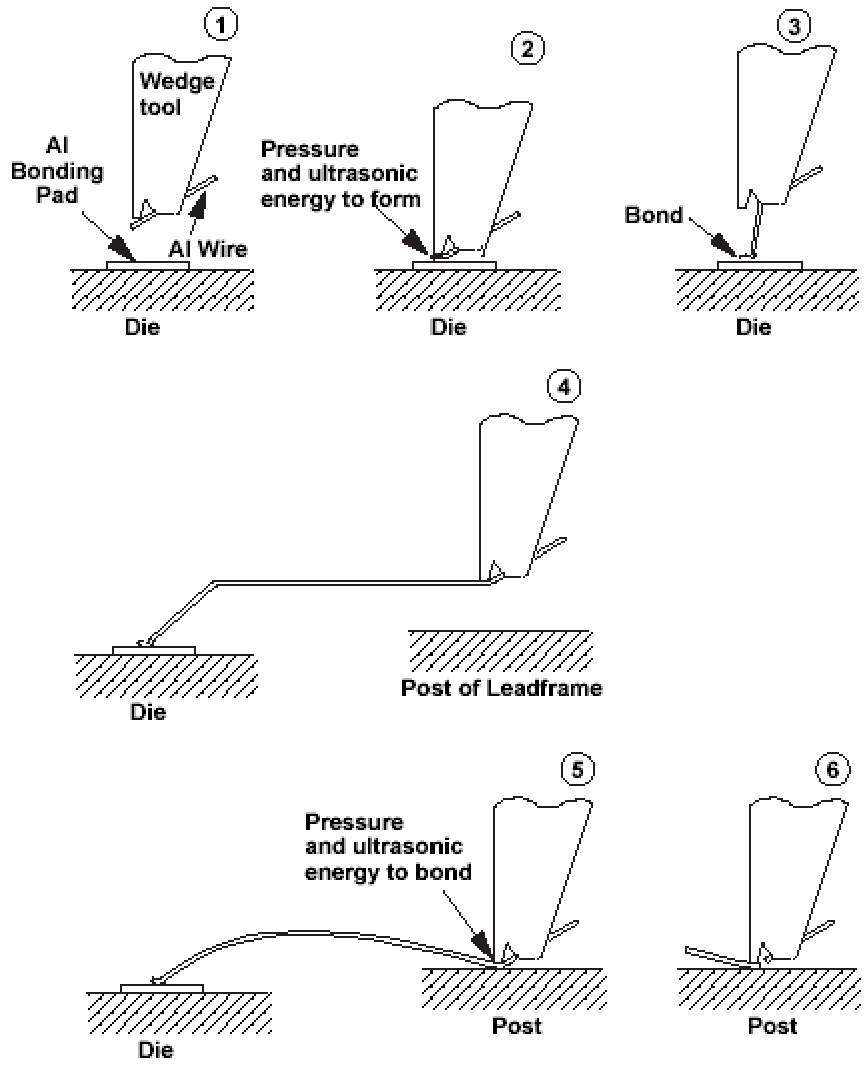

Figure 1-8 Ultrasonic bonding process

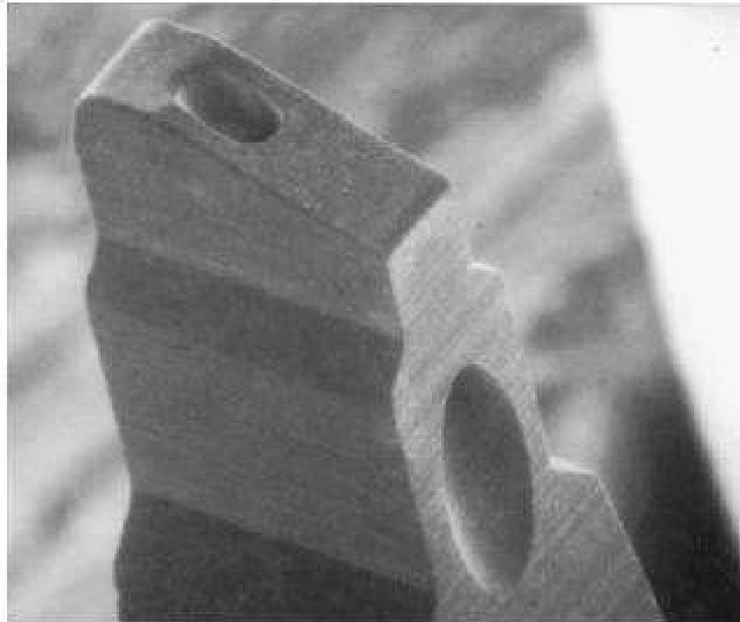

Source: Micro Swiss/
ICE, "Roadmaps of Packaging Technology"

Figure 1-9 Ultrasonic wedge tool

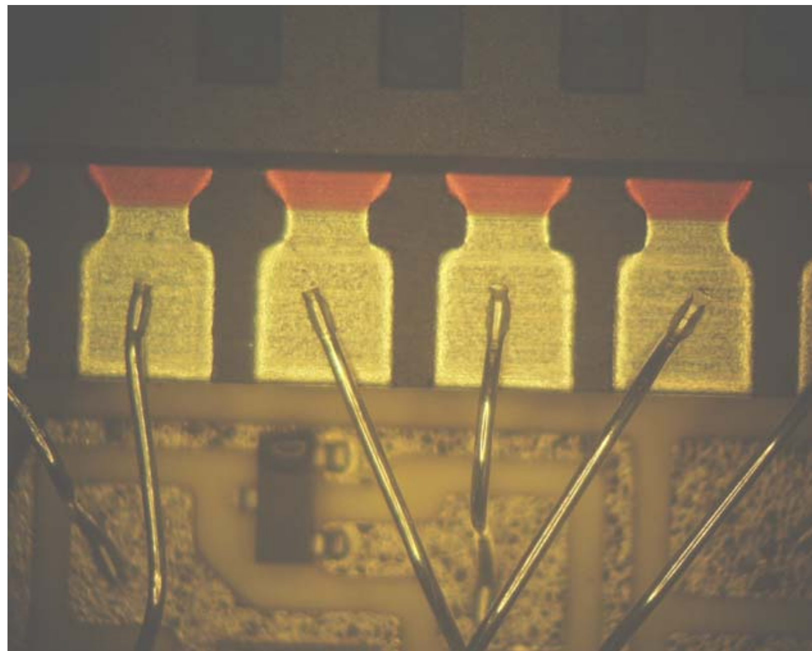

Figure 1-10 Unidirectional wire bonds in a hybrid power module

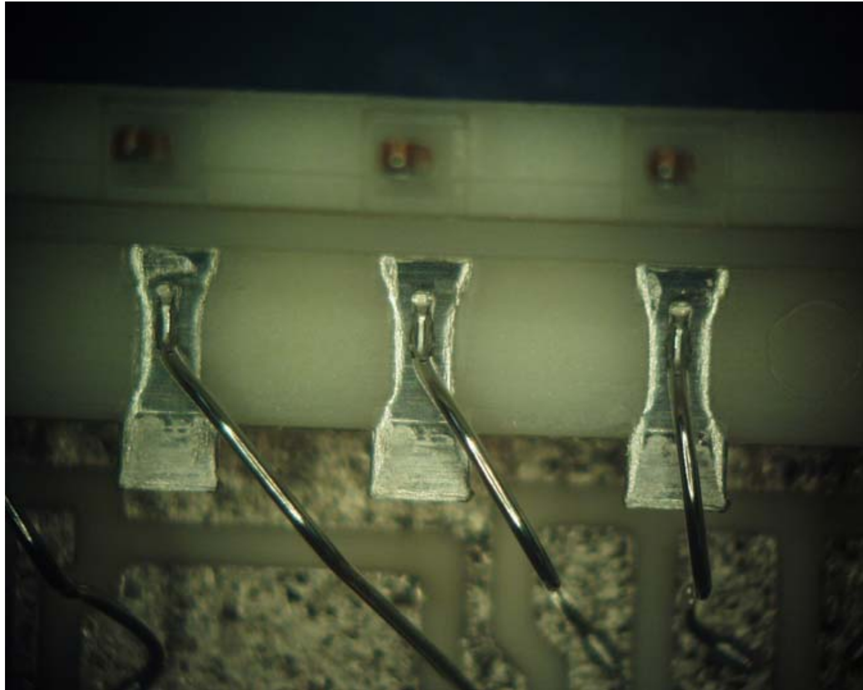

Figure 1-11 Wires bonded with twist in hybrid power modules

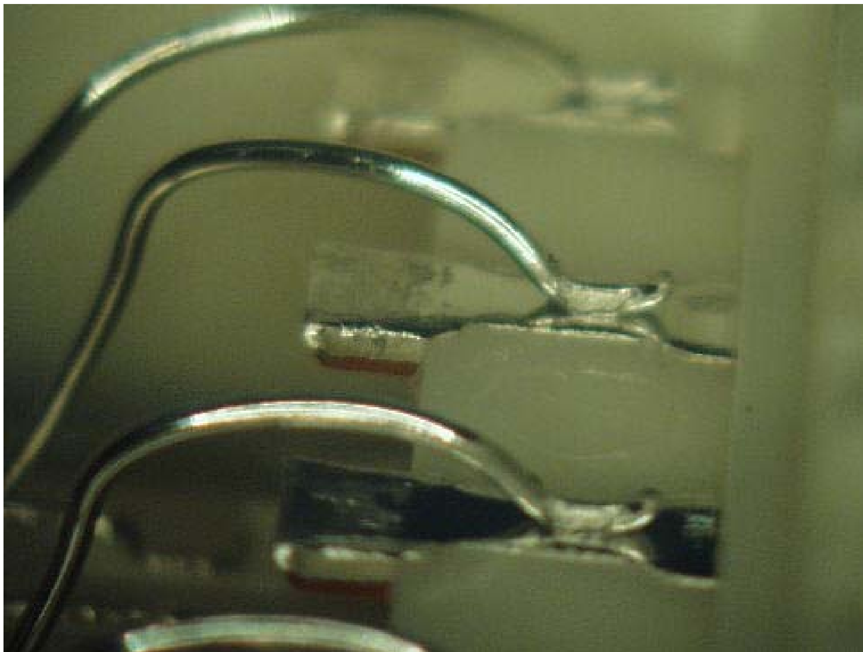

Figure 1-12 View of the wire bond near the heel

Figure 1-10 shows actual ultrasonically wedge bonded wires used in a hybrid power module. Ultrasonic wedge bonding is generally used to bond wires between bond pads that are aligned parallel to one other. However with rotary bond heads, wires can be bonded between non-aligned bond pads as shown in Figure 1-11. Figure 1-12 shows the side view of the bond to illustrate the change in cross section of the wire near the heel due to the wedge bonding tool.

1.5 Failure Mechanism

In spite of the universal use of wirebonding, and its high volume, it is also the most common source of failure for an IC. Wirebonding failures constitute around 26% of all IC failures as shown in Figure 1-13.

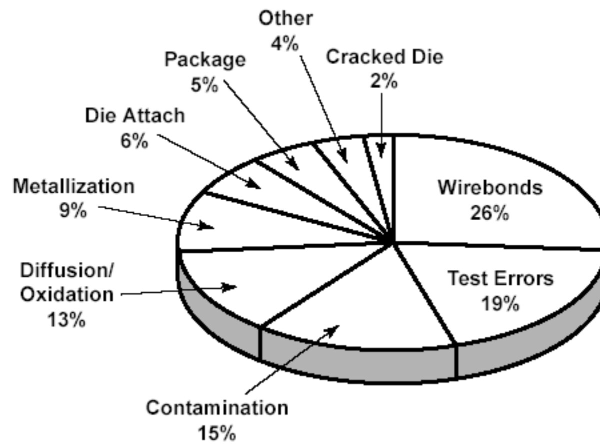

Source: ICE, "Roadmaps of Packaging Technology"
Figure 1-13 IC failures

In the past the number of failures due to wirebonds were numerous and the number of failure mechanisms identified were limited. Currently around a dozen failure mechanisms have been identified for Al-Al bonds [Harman, 1997]. These failure mechanisms include: corrosion, wire flexure, wire bond lift-off, cratering, dendritic growth and electrical leakage.

Corrosion of passive and active microelectronic devices by ionic contaminants can result in problems ranging from a loss in strength to a change in thermal properties. Pecht [Pecht, 1990] provides a foundation to which prior and future corrosion models can be compared.

Thermal cycling can cause wires to lift-off due to shear stresses generated between the bond pad-wire interface and between bond pad–substrate interface. This can be reduced if the coefficient of thermal expansion (CTE) mismatch between the materials at the interface is reduced. Ramminger [Ramminger et al., 2003] and Hu [Hu et al., 1991] have developed physics-of-failure based models to study wire lift-off failures.

The thermal cycling environment can also cause the wires to flex in response to the rise in temperature. The flexing motion of the wire when exposed to a power cycling environment was captured by Ravi [Ravi et al. 1972]. The flexing motion produces stress reversals in the heel of the bond wire thus causing cracks to appear at this location. The heel of the wire is already weakened due to the ultrasonic bonding and the flexing motion is enough to initiate a crack in the heel of the wire. Cracks in the heel of the wire can also arise due to: a sharp-heeled bonding tool, by operator motion, bonding machine vibration or due to the wire loop formation. It is very important to decide and produce an optimum loop profile since a sub optimal loop profile can cause unnecessary flexing of the wire.

Also, an asymmetrically bonded wire (wires bonded with a height offset) promotes cracking more than a wire bonded without any height offset [Harman, 1997]. The bond pull strength should be indicative enough of the weakening of the wire at the heel of the wire due to cracking.

Thermal cycling experiments were conducted on power modules similar to the one shown in Figure 1-3. Some of the wires were twisted as shown earlier in Figure 1-11. Twisting was introduced by bonding wires between non-aligned bond pads. All the experiments resulted in wire flexure failures (Figure 1-14 and Figure 1-15). Figure 1-14 shows the crack initiation site. Hence, in the current thesis, it was decided to focus specifically on this failure mechanism.

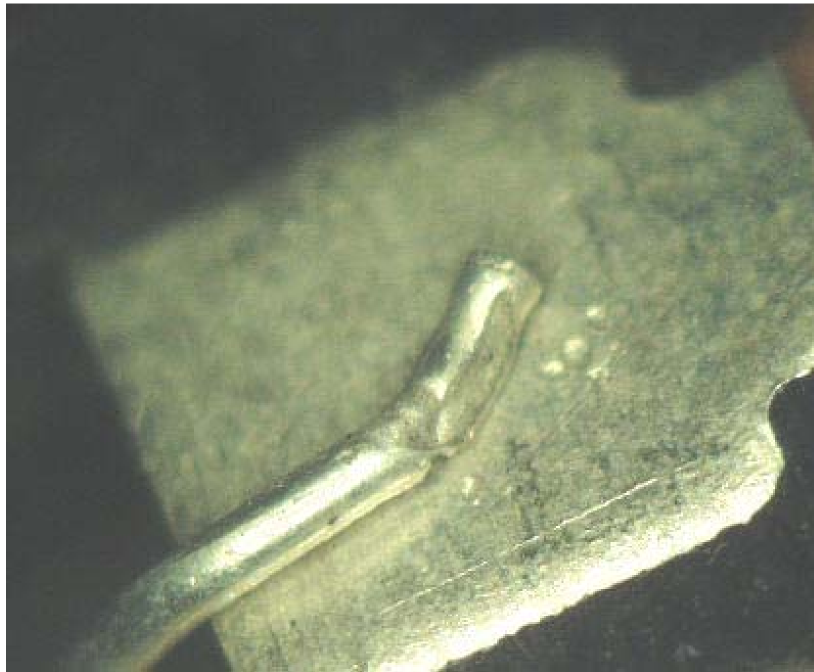

Figure 1-14 Wire heel crack

Figure 1-15 Failure of wire at the heel for a twisted wire

1.6 Virtual Qualification

Wire bonding evaluation criteria vary depending on application requirements. The visual method of inspection uses an optical microscope, scanning electron microscope (SEM) and other analytical instruments to find the defective bonds. Mechanical testing is used to evaluate the strength of the bonds. Evaluation methods can be found in several published standards, but the most common standard is MIL-STD-883. They include:

- Internal visual (Method 2010; Test condition A and B)
- Delay measurements (Method 3003)
- Destructive bond pull test (Method 2011)
- Nondestructive bond pull test (Method 2023)

- Ball bond shear test
- Temperature cycling test (Method 0101, Test Condition C)
- Constant acceleration (Method 2001; Test condition E)
- Random vibration (Method 2026)
- Mechanical shock (Method 2002)
- Stabilization bake (Method 1008)
- Moisture resistance (Method 1004)

The temperature cycling tests subject the wirebond interconnects to alternatively changing temperatures. The failure mechanisms addressed by the temperature cycling test include flexure failure of the wire at the heel, bond pad-substrate shear failure, wire-substrate shear failure.

This thesis focuses primarily on the flexural fatigue failures of wedge bonded wires commonly seen in power devices. The approach explained in this thesis to study the flexural fatigue failure is generic and can be extended to cover any semiconductor device with wedge-bonded wire interconnections.

A typical power module has traditionally been required to sustain 1000 thermal cycles between –40°C and +125°C in order to be qualified for use. This procedure is meant to detect modules that are likely to fail by wire flexure fatigue in operational life when the assembly is subjected to cyclic strain as a result of thermal (i.e., temperature and power) cycling.

While this traditional procedure is well accepted, it has two major shortcomings. First, the selection of the temperature cycle magnitude and duration is arbitrary and they do not correspond to a particular field life. Second, the procedure is costly and time

consuming and is therefore undesirable in today's product development environment of shortened design cycles and quick time-to-market. It is no longer acceptable to make a prototype, subject it to a series of standardized tests, analyze the failures, fix the design, and test again. Instead, a fundamental model is needed to assess the susceptibility of module designs to wire flexure fatigue without conducting such extensive qualification tests. Such a model should be based on a fundamental understanding of the thermo-mechanical mechanism that causes wire flexure failure in electronic systems. The use of such models to qualify assemblies for field use is known as virtual qualification.

1.7 Scope of the Current Thesis

Focus on this thesis would be limited to flexure-induced failure of wedge-bonded interconnections. The outcome of this research is a model which can be used to produce guidelines for reliable wirebonded interconnections. In addition to identifying the prime factors affecting the reliability of the wirebonds, this research also identified the optimum values of design parameters based on the available constraints. The models are energy-based since every physical system would prefer to take up a configuration where it would store minimum potential energy. Identifying the most stable configuration can help decide the best loop profile. This information can be fed to the wirebonder; to produce reliable wire bonded interconnections.

Chapter 2 describes a first order physics-of-failure (PoF) based wire flexure model. The chapter describes a load transformation model and a damage model. The load transformation model determines the cyclic strain at the heel of the wire during

temperature cycling. The damage model calculates the life based on the strain cycle magnitude and the elastic-plastic fatigue response of the wire.

The validation of the analytical model, sensitivity analysis and model limitations are explained in Chapter 3.

Chapter 4 deals exclusively with one of the limitations explained in Chapter 3, the effect of ultrasonic bonding of wires on the flexural stresses, which has not been modeled in the first order PoF model, but has been addressed using an FEM model of the ultrasonic bonding of wires. The critical bonding parameters that could influence the wire flexural stresses are identified.

Chapter 5 deals with another possible factor that could influence the flexural stresses, the effect of wire twisting. A new, energy-based, approach has been developed for determining the minimum energy profile in a Euclidean three-space, R^3. The heel stresses are determined for such geometries using FEA.

The thesis is concluded in Chapter 6 with the list of contributions and suggestions for future work.

1.8 Nomenclature and Terminology used

ε = Strain at the wire heel due to wire flexure

ε_{low}= Bending strains at lower bond pad

ε_{high}= Bending strains at upper bond pad

σ = Stress at the wire heel due to wire flexure

σ_{low}= Bending stresses at lower bond pad

σ_{high}=	Bending stresses at upper bond pad
e=	offset of neutral axis from centroidal axis
F_T=	Resultant reaction force on top section of wire
F_B=	Resultant reaction force on bottom section of wire
M_{ult}=	Ultimate resisting moment
σ_f'=	Fatigue strength coefficient
b=	Fatigue strength exponent
ε_f'=	Fatigue ductility coefficient
c=	Fatigue ductility exponent
σ_{ys}=	Yield stress
σ_0=	Mean stresses
y_R=	Distance of outermost fiber from neutral axis
R =	Radius of curvature from the neutral axis
r =	Radius of wire
$\bar{r}$ =	Radius of curvature from centroidal axis
π=	Potential energy
λ=	Lagrange parameter
ρ_I =	Radius of curvature before heating
ρ_f =	Radius of curvature after heating
ψ_i =	Take off angle before heating
ψ_f =	Take off angle after heating
κ_i =	The curvature at the heel of the wire before heating

$\kappa_f =$ The curvature at the heel of the wire after heating

$\alpha(u) =$ Differentiable curve parameterized by u

$\beta(v) =$ Differentiable curve parameterized by v

$d_i =$ The x co-ordinate of the reference point, defining the loop height, before heating

$h_i =$ The y co-ordinate of the reference point, defining the loop height, before heating

$D_i =$ The span of the wire before heating

$H_i =$ The bond pad height offset of the wire before heating

$d_f =$ The x co-ordinate of the reference point, defining the loop height, after heating

$h_f =$ The y co-ordinate of the reference point, defining the loop height, after heating

$D_f =$ The span of the wire after heating

$H_f =$ The bond pad height offset of the wire after heating

$\alpha_{sub} =$ Thermal expansion coefficient of the heat spreader

$\alpha_{glue} =$ Thermal expansion coefficient of the glue

$\alpha_{ply} =$ Thermal expansion coefficient of the plastic frame

$\alpha_{dbc} =$ Thermal expansion coefficient of the DBC layer

$E =$ Modulus of elasticity of Al wire

$\Delta T =$ Temperature load cycle applied

FL= Tool flat length

BF=	Bond Flat
B=	Wire deformation due to bonding
d =	The x co-ordinate of the reference point
h =	The y co-ordinate of the reference point
D =	The span of the wire
H =	The bond pad height offset of the wire
w=	The z co-ordinate of the reference point
W=	Width offset of Bond pad
I=	Moment of Inertia of Wire
L=	Length of wire
L_1=	Length of first curve
L_2=	Length of second curve

Figure 1-16 shows a cross sectional view of a typical power module with some of the commonly used terminology seen throughout the text of the report.

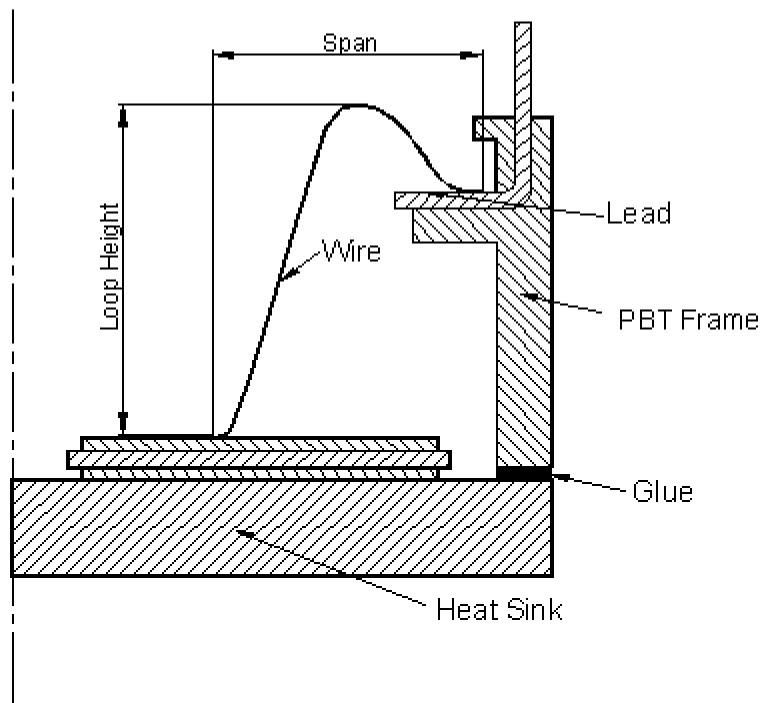

Figure 1-16 Terminology used

Chapter 2: Wire Flexure Failure and Life Prediction Models

Experiments and theory have proved that the heel of the wire is highly susceptible to fatigue failure due to flexure of the wire. The flexing of the wire changes the curvature near the heel and this produces strains in the wire. This chapter describes a physics-of-failure based analytical model for studying wire failure due to cumulative damage resulting from repeated flexure during thermal cycling.

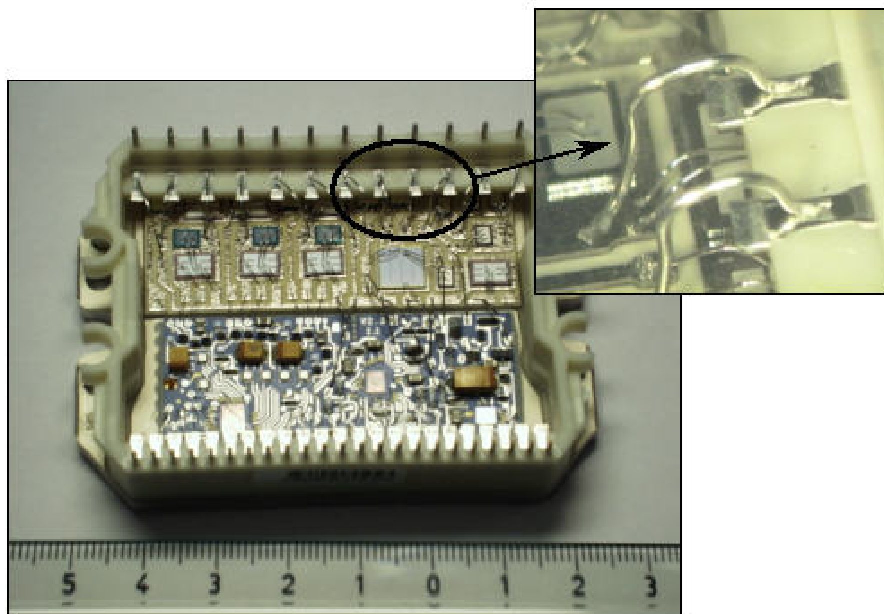

Figure 2-1 Typical power module

The thermal cycling environment produces stress reversals in the heel of the bond wire and eventually results in fatigue failure of the wire. The life prediction model consists of a load transformation model and a damage model.

The load transformation model computes the stresses and the strains from the change in curvature of the wire near the heel. The change in curvature is more dominant in the heel of the wire near the upper bond pad, for a wire that is bonded with a bond pad height offset [Harman, 1997].

2.1 Review of existing Fatigue Models and Limitations

The first failure prediction model for wire bonds was explained in 1989 [Pecht et al., 1989]. The strains were a function of the change in take-off angles of the wire near the heel. The impracticality in measuring the take-off angles [Pecht et al., 1989] near the heel of the wire necessitated further efforts in this direction. In 1991, a new energy based model [Hu et al., 1991], was proposed to predict strains for wires bonded without any height offset. The theory of curved beams was used to predict strains near the heel of the wire. However, in wires bonded with a height offset, the wire is more strained near the heel of the elevated bond bad. Also, procedures for determination of wire loop profiles are limited in literature. They are mostly based on mapping of wire loop profiles in existing power modules. These loop profiles are very essential for use in analytical tools like finite element.

Based on the limitations mentioned, it is also necessary for the new first-order wire flexure model to incorporate the following,

- A well defined procedure to determine the wire loop profiles
- To account for the height offset between the bond pads
- To eliminate the need to measure take-off angles

2.2 Load Transformation Model

The load transformation model is essentially used to predict the bending strains/stresses in the wire. These strains are derived based on the theory of curved beams. Pure bending strains, at any section offset from the neutral axis, would be equal to the ratio of change in length to the original length of the curved section, given by,

$$\varepsilon = \frac{y_R d\psi}{\rho_i \psi_i} \tag{2-1}$$

where, y_R is the distance of the outermost fiber from the neutral axis, $d\psi$ is the change in angle subtended by the curved beam and ρ_i is the curvature of the section at the surface of the beam before deformation (note: - the suffixes i and f are used to denote the variables described before and after deformation of the wire). Hence, $\rho_i\psi_i$ would indicate the original length of curved beam. The strains in the upper surface of the wire, given in Eq. 2-1, can be rewritten in terms of the new curvature after deformation, ρ_f and the radius of curvature of the neutral axis, R, by,

$$\varepsilon = \frac{(R-\rho_f)d\psi}{\rho_i \psi_i} \approx \frac{(\bar{r}-\rho_f)d\psi}{\rho_i \psi_i} = \frac{r(\psi_i - \psi_f)}{\rho_i \psi_i} \tag{2-2}$$

where, $\bar{r}$ is the radius of curvature of the wire from the centroidal axes (Figure 2-2) and r is the radius of the cross-section of the wire.

The curvature in the beam results in an offset of the neutral axis of the wire from its centroidal axis. The location of the neutral axis follows from the condition that the summation of the forces perpendicular to the section must be zero. The location of the neutral axis for a curved beam with a circular cross-section is,

$$R = \frac{\bar{r} + \sqrt{\bar{r}^2 - r^2}}{2} \qquad \text{2-3}$$

However, for all practical purposes R can be equated to $\bar{r}$ as done in Eq. 2-2, since the wire has a high radius of curvature when compared to the wire radius near the heel.

Assuming no appreciable change in a small curved length of the wire, δs, before and after deformation, the radii of curvatures and the take off angles can be related by the expression,

$$\delta s = \rho_i \psi_i \approx \rho_f \psi_f \qquad \text{2-4}$$

From Eq. 2-2 and Eq. 2-4 the expressions for the strains can be rewritten as,

$$\varepsilon = \frac{r(\rho_f - \rho_i)}{\rho_i \rho_f} = r(\kappa_i - \kappa_f) \qquad \text{2-5}$$

where κ_i and κ_f are the curvatures of the wire and they are inversely proportional to the radius of curvature. It is evident from Eq. 2-5 that the strains are a function of the change in curvature. This dependence of heel crack failures on the loop geometry has also been shown experimentally [Ramminger et al., 2000]. Hence, one of the most important aspects in the model would be the accurate prediction of the geometry.

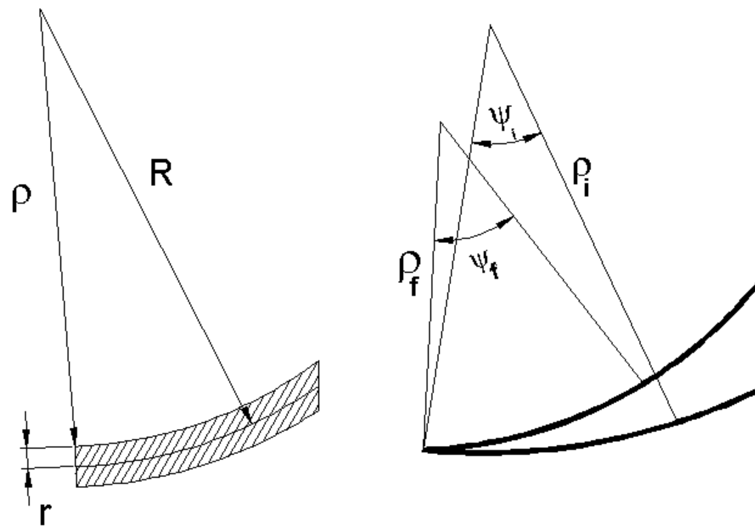

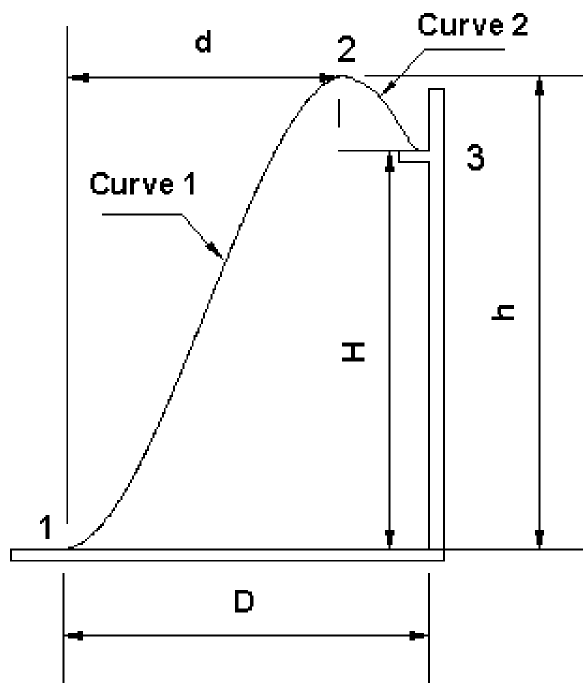

Figure 2-2 Wire label definitions

2.2.1 Wire Loop Profile

The wedge-bonded wires currently studied are all ultrasonically bonded. A non-zero bond foot length (length of the base of the ultrasonic wedge tool that presses the wire) ensures a zero vertical displacement at all ends that are pressed. It is easy to understand that this would force the conditions of zero slopes and zero displacements at ends where the wire is bonded. Also, the length of the wire is always provided as a constraint (this requirement would become clearer in the later sections). Therefore, any suitable wire geometry that is obtained should satisfy the admissibility conditions i.e. the boundary conditions and the length constraint.

For representing the wire profile, a single polynomial of a very high order would be an obvious choice. These curves are smooth in the sense of being maximally differentiable and represented through the Lagrange interpolating polynomial. However with all the constraints provided, the curve will have more stationary points. The oscillation of the interpolating polynomial can be reduced by using piecewise interpolating curves. However, the first derivatives in the interpolating points are discontinuous and hence more interpolating points are needed to represent the wire geometry. Hence, one of the possible solutions would be to represent the wire geometry using a piecewise interpolating polynomial of third order which is differentiable at least to the first order, at the interpolating points.

A Hermite polynomial [Meyyappan et al., 2003] was initially used and the wire was represented using two curves as shown in Figure 2-2. The bond point locations are given by points, 1(0, 0) and 3(D, H). Point 2 is chosen to be arbitrary with co-ordinates (d, h). Hereafter, the notations point 1, point 2 (sometimes also referred as the reference

point defining the loop height) and point 3 are reserved and cross-referenced to the Figure 2-2 throughout the text.

A Hermite interpolation polynomial satisfies a C^1 continuity (continuity of y and y'). Due to the lower order continuity requirement, the solution process is much easier but more interpolation points would be needed for representing the wire geometry more accurately.

A cubic spline satisfies a y'' continuity in addition to the y and y' continuity provided by the Hermite Interpolation polynomial. Therefore, it would be sufficient to use much fewer interpolation points in between the bond point locations. Also, it can be proved that the cubic spline is the smoothest possible curve through a set of points and it would always minimize the strain energy [Spath 1974, de Boor 2001]. Hence, one can now combine all these features with a cubic spline: i.e. weaker oscillations, a C^2 continuity, and minimum the strain energy for the chosen interpolating point (point 2).

However, for the sake of completeness both the approaches, Hermite polynomial and the Cubic spline approach [Meyyappan et al., 2003] have been explained.

2.2.2 Hermite Polynomial to represent the Wire Profile

The wire loop geometry is fitted through a Hermite interpolation polynomial. For simplicity, the model described is not energy-based and hence is less accurate. This approach requires the reference point, point 2, to be provided by the user. The curves $\alpha(u)$ and $\beta(v)$ are used to map the parameters u and v to the curves 1-2 and 2-3 respectively shown in Figure 2-2.

Let $\alpha,\beta:I\rightarrow R^2$ be differentiable curves parameterized by u and v respectively such that,

$$\alpha(u) = (ud, h(3u^2-2u^3)) \tag{2-6}$$

$$\beta(v) = (v(D-d)+d, h+3(H-h)v^2-2(H-h)v^3) \tag{2-7}$$

Eq. 2-6 and Eq. 2-7 have been derived based on the boundary conditions (slopes and co-ordinates of the data points that define the Hermite Polynomial). The detailed derivations have been omitted for the sake of simplicity. For a regular parameterized curve, the curvature $\kappa(u)$ is given by,

$$\kappa(u) = \frac{\left|\alpha(u)' \wedge \alpha(u)''\right|}{\left|\alpha(u)'\right|^3} \quad , \quad \kappa(v) = \frac{\left|\beta(v)' \wedge \beta(v)''\right|}{\left|\beta(v)'\right|^3} \tag{2-8}$$

Substituting u=0 in Eq. 2-8 provides the curvature of the wire at point 1 while v=1 provides the curvature of the wire at point 3. Simplifying the equations for the curvature, κ_{low_0} (curvature at u=0) and κ_{high_0} (curvature at v=1) can be written as,

$$\kappa_{low_0} = \frac{6h}{d^2} \quad , \quad \kappa_{high_0} = \frac{6(h-H)}{(D-d)^2} \tag{2-9}$$

The "low_0" and "high_0" suffixes are used to represent the terms at lower and elevated bond pad for a wire bonded with a height offset before heating. Similarly, κ_{low_1} and κ_{high_1}, is determined after thermal cycling the wire. The strains are then expressed as a function of the change in curvatures as shown in Eq. 2-5.

After simplification, the strains in the lower and upper bond pads are given by,

$$\varepsilon_{low} = 6r\left(\frac{h_i}{d_i^{\,2}} - \frac{h_f}{d_f^{\,2}}\right) \quad , \quad \varepsilon_{high} = 6r\left(\frac{h_i - H_i}{(D_i - d_i)^2} - \frac{h_f - H_f}{(D_f - d_f)^2}\right) \qquad \text{2-10}$$

The displacement of the bond pads on the package frame due to thermal cycling (explained in Appendix A) is embedded in the variables D_f, H_f. For a wire bonded without any height offset and when the reference point 2 is located at mid span, the ε_{low} and ε_{high} are observed to be the identical as expected (see Eq. 2-10).

2.2.3 Cubic Spline to represent the Wire Loop Profile

In this approach, the wire profile is represented by means of a cubic spline. One of the biggest disadvantages in the Hermite polynomial approach was the location of point 2, which is very difficult to measure. Also, a few load cycles can make the wire take up a different configuration, regardless of the original loop profile obtained after the bonding process. Hence, it becomes essential to use an energy-based approach to determine the stress free state. Point 2 is assumed arbitrary and is determined such that strain energy of the wire is minimized.

The interpolating polynomial between any two points with co-ordinates (x0, y0) and (x1, y1) respectively can be written as,

$$p_o(x) = \frac{-y_0}{h_0}(x - x_1) + \frac{y_1}{h_0}(x - x_0) \qquad \text{2-11}$$

$$+ \frac{S_0 - \tilde{S}_0}{h_0^2}(x - x_0)(x - x_1)^2 + \frac{S_1 - \tilde{S}_0}{h_0^2}(x - x_1)(x - x_0)^2$$

where, S_0 and S_1 represent the slopes at the two end points. $\tilde{S}_0$ represents the gradient of a straight line passing through the two points. The representation of the polynomial using Lagrange parameter automatically ensures a C^1 continuity (continuity of y and y′). This procedure is very much similar to how the C^1 continuous beam elements with displacement and slope continuity are derived in the finite element method. The point 2 acts as a common point lying on the boundary of the curves 1 & 2 (see Figure 2-2). By equating the second order derivative of Eq. 2-11 at point 2 from the two curves (1 & 2) a second order continuity is automatically enforced. The execution of these steps yield the value of S_1 as,

$$S_1 = \frac{3}{2D}\left[\frac{(H-h)d}{(D-d)} - \frac{(d-D)h}{d}\right] \tag{2-12}$$

A more detailed derivations have been provided in Appendix B. Substitution of Eq. 2-12 in Eq. 2-11, yields the equation for the curve 1 (defined by points 1 & 2) as,

$$y = \frac{hx}{d} - \frac{\frac{h}{d}x(x-d)^2}{d^2} + \frac{S_1 - (\frac{h}{d})}{d^2}(x-d)x^2 \tag{2-13}$$

Similarly, the equation of curve 2 is given by (defined by points 2 & 3),

$$y = \frac{h(x-D)}{d-D} + \frac{H(x-d)}{D-d} + \frac{S_1 - \left(\frac{H-h}{D-d}\right)}{(D-d)^2}(x-d)(x-D)^2 - \frac{H-h}{(D-d)^3}(x-D)(x-d)^2 \tag{2-14}$$

The curvatures are then determined for points 1 and 3. The curvatures at any point on the curve is given by,

$$\kappa = \frac{y''}{\left(1 + y'^2\right)^{3/2}} \quad \text{2-15}$$

Minimization of Strain Energy of the Cubic spline

The potential energy of the wire, represented by the piecewise cubic spline, is given by,

$$\Pi = \frac{EI}{2}\int_0^d \kappa_1(x)^2\, ds + \frac{EI}{2}\int_d^D \kappa_2(x)^2\, ds \quad \text{2-16}$$

where, EI is the flexural rigidity of the wire, κ_i's are the corresponding curvatures and ds is the incremental length of the wire (Note:- for a wire with varying cross section the moment of inertia, I, has to lie within the integral). The lengths of the curves 1 and 2 respectively are given by L_1 and L_2 (=$L-L_1$) and $ds=(1+y'^2)^{0.5}dx$. Other than the admissibility conditions, the dependent variables should also satisfy the following constraint equation,

$$G = L - (L_1 + L_2) = L - \left(\int_0^d (1 + y'^2)^{0.5}\, dx + \int_d^D (1 + y'^2)^{0.5}\, dx\right) = 0 \quad \text{2-17}$$

G = 0 is enforced through a Lagrange parameter λ. Therefore the new functional to be minimized is Q where,

$$Q = \Pi + \lambda G \quad \text{2-18}$$

Q is minimized by seeking its stationary value,

$$\delta Q = 0 \tag{2-19}$$

$$\frac{\delta Q}{\delta d} = 0 \qquad \frac{\delta Q}{\delta h} = 0 \qquad \frac{\delta Q}{\delta \lambda} = 0 \tag{2-20}$$

The above set of non-linear equations are solved iteratively using the Levenberg-Marquardt algorithm to provide the location of the second point (d, h) which seeks to minimize the potential energy and also satisfies the length constraint. Substitution of d and h into Eq. 2-13 provides the wire geometry. However, the energy minimization could also be performed using the 'fmincon' function, found in the optimization toolbox, in Matlab. Both the approaches require the input of a guess value. These guess values are very critical to the model, since the curve could have several local minima and it is the objective of the program to choose the point that determines the global minima of the curve.

Wire Stresses at the Heel

The radii of curvatures of the curves 1 and 2 are calculated at x=0 and x=D using Eq. 2-13 as,

$$\rho_{low_0} = \frac{\left(1 + y'^2\right)^{1.5}}{y''} \text{ at x=0} \tag{2-21}$$

$$\rho_{high_0} = \frac{\left(1 + y'^2\right)^{1.5}}{y''} \text{ at x=D} \tag{2-22}$$

When the wire elongates due to heating, the wire would occupy a new configuration. Also, the frame can expand/contract in the linear direction and

simultaneously bow due to CTE mismatch between the composite layers of the substrate. The frame displacements can help the wire reduce or build strains depending on the frame properties and the load cycle. Hence, it is very important to capture the frame displacements very accurately. The significance of the frame displacement and how it can be used to reduce the bending stresses in the heel of the wire is explained in the following chapter. A frame displacement model used for a generic power module has also been explained in Appendix A.

The heating of the frame results in movement of points 1 and 3. Assuming the point 1 to remain fixed the relative movement of point 3 with respect to point 1 is determined. It is an inherent property of curves that the arc length, curvature and torsion of a curve do not change due to rigid motion [Manfredo P. Do Carmo, 1976], and hence the above assumption is valid.

Using the information of the frame displacement and the expansion of the wire due to heating, the new co-ordinates (d, h) of the displaced wire are calculated. Eq. 2-21 and Eq. 2-22 are recalculated based on the displaced point 2 (d, h) to provide the new set of radii of curvature ρ_{low_1} and ρ_{high_1} after heating the wire. The strains in the heel of the wire is determined using Eq. 2-5, Eq. 2-21 and Eq. 2-22 as,

$$\varepsilon_{low} = \frac{r(\rho_{low_1} - \rho_{low_0})}{\rho_{low_1}\rho_{low_0}} \qquad \varepsilon_{high} = \frac{r(\rho_{high_1} - \rho_{high_0})}{\rho_{high_1}\rho_{high_0}} \qquad 2\text{-}23$$

For high cycle fatigue (low stress) where material linearity is assumed, the stresses are calculated by the following expressions,

$$\sigma_{low} = E\,\varepsilon_{low} \qquad \sigma_{high} = E\,\varepsilon_{high} \qquad 2\text{-}24$$

2.3 Residual Stresses during Loop Formation

On removing the constraints, the wire should retain its original profile if it had deformed elastically. However, clipping a set of bonded wires showed that the wires had a permanent deformation and they retained their current shape. For an elastic, perfectly plastic material, some fibers of the wire away from the neutral axis would have deformed plastically while the fibers near the neutral axis would have deformed elastically. On unloading, the elastic sections of the wire would try to retain their original shape whereas the plastically deformed section would prefer staying in the permanent set configuration. This would introduce residual stresses in the wire.

The residual stresses when superimposed on the applied fatigue loads alter the mean stresses of fatigue cycling. It is necessary to quantify the magnitude of these residual stresses, as they could be critical to the damage prediction model. This section describes an approach to determine the residual stresses in a curved beam that is deformed inelastically and then unloaded.

2.3.1 Inelastic Bending of Curved Beams

In the theory of pure bending of curved beams, maximum bending stresses occur in the outermost fibers. For the purpose of illustration of elastic and inelastic stresses in a beam, a rectangular section of the beam is used.

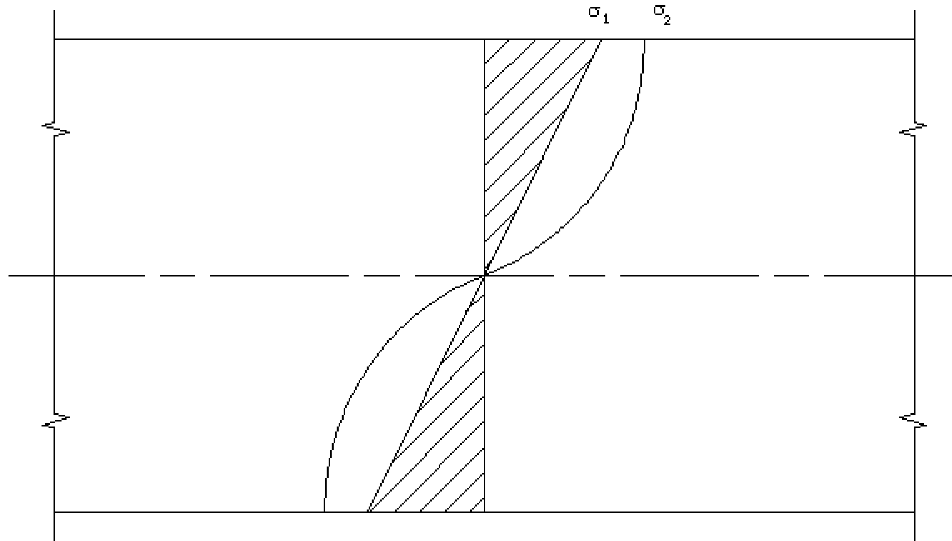

Figure 2-3 Rectangular beam in bending

σ_1 and σ_2 in Figure 2-3 represent the elastic and inelastic stresses on applying a bending moment to the beam. However, for a curved beam, the elastic stress distribution σ_1 shown in the figure would be a curve due to the offset of the neutral axis from the centroidal axis. The worst case of loading the beam, with elastic-perfectly plastic material properties, would result in having uniform compressive and tensile stresses (σ_{ys}) on either sides of the neutral axis. In order to prove the existence of the inelastic stress distribution and permanent deformation during the loop formation, a finite element analysis was performed.

It is very difficult to determine the stresses by simulating the formation of the loop using non-linear finite element method. However, the reverse procedure of unloading a deformed wire with zero offset is feasible. The wire in its minimum energy state, with a span of 20 mm, was assumed to be the unstressed configuration and it was given a horizontal displacement of 0.5 and 1.1 mm. The resultant bending stresses across the wire cross-section was then observed. Figure 2-4 shows the finite element model with

the displaced configuration. Figure 2-5 shows that for 0.5 mm displacement the wire has little plastic deformation while for a 1.1 mm displacement there is more uniform tensile and compressive stresses of magnitude σ_{ys}. Considering the amount of deformation involved during the wirebonding process, uniform tensile and compressive stresses of magnitude σ_{ys} have been assumed throughout the sections of the wire for the purpose of determination of the residual stresses.

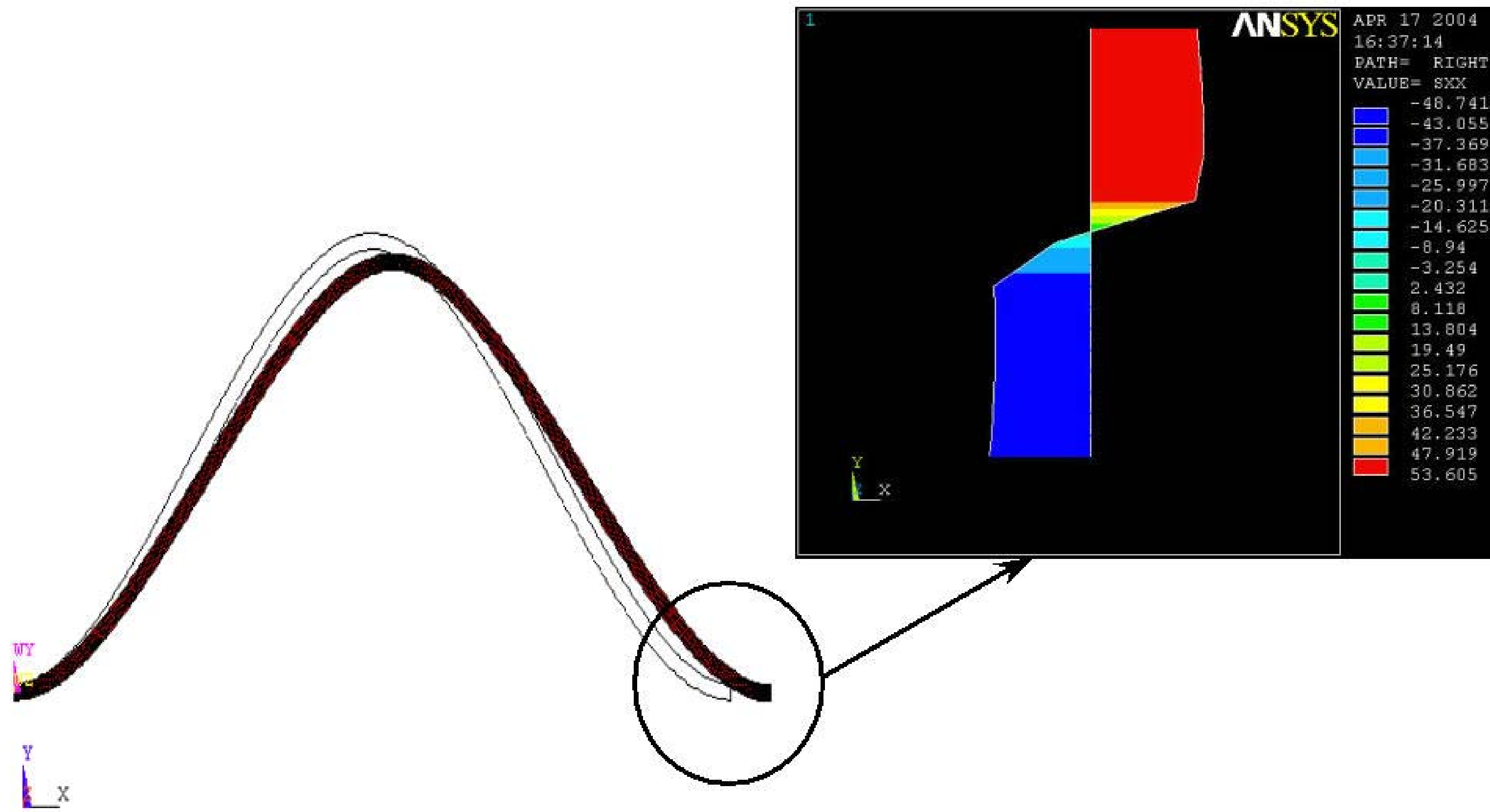

Figure 2-4 Finite element simulation of deformation

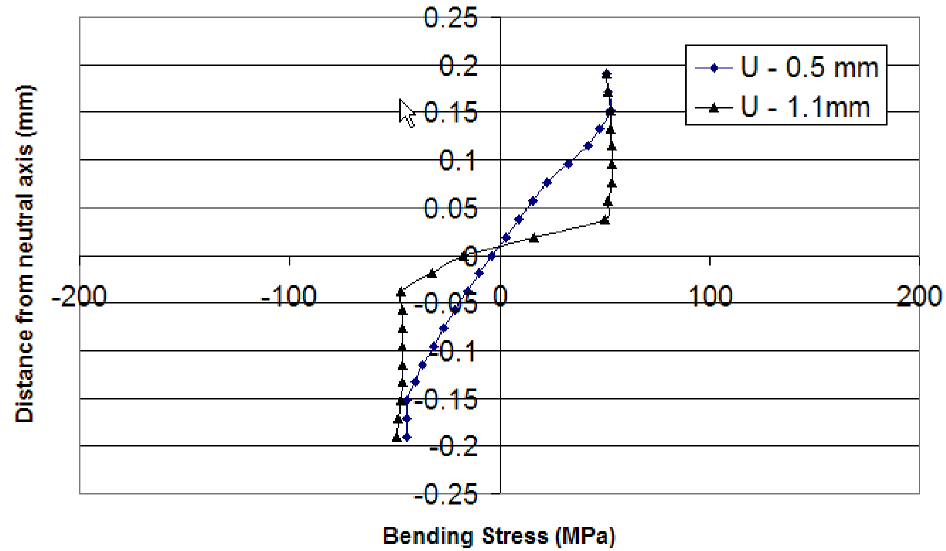

Figure 2-5 Stress distribution across fibers

2.3.2 Residual Stresses in a Curved Beam

As mentioned earlier, the whole section of the beam above the neutral axis has deformed uniformly to a uniform tensile stress of σ_{ys} while the sections below the neutral axis have been subjected to a uniform compressive stress of $-\sigma_{ys}$ during the loop formation. Since the neutral axis is offset from the centroidal axis (defined by e), the area of cross section of the wire on top and bottom are different.

The varying cross-sectional area would eventually result in varying resultant tensile and compressive forces on top and bottom sections of the wire. The cross sectional areas in the top (A_T) and bottom (A_B) of the wire are given by,

$$A_T = r^2\left[\frac{\pi}{2} - \theta_1 - \frac{\sin 2\theta_1}{2}\right] \quad , \quad A_B = r^2\left[\frac{\pi}{2} + \theta_1 + \frac{\sin 2\theta_1}{2}\right] \qquad \text{2-25}$$

where, θ_1 is defined by

$$\theta_1 = \sin^{-1}\left(\frac{-e}{r}\right) \qquad \text{2-26}$$

where r is the radius of cross section of the wire and e is the offset of the neutral axis from the centroidal axis. Eq. 2-25 has been derived based on an integration of a small strip formed by two adjacent chords from a circle. The detailed derivations have been omitted for simplicity. The resultant force acting on the top (F_T) and bottom fibers (F_B) are given by,

$$F_T=\sigma_{ys}A_T \qquad F_B= -\sigma_{ys}A_B \qquad \text{2-27}$$

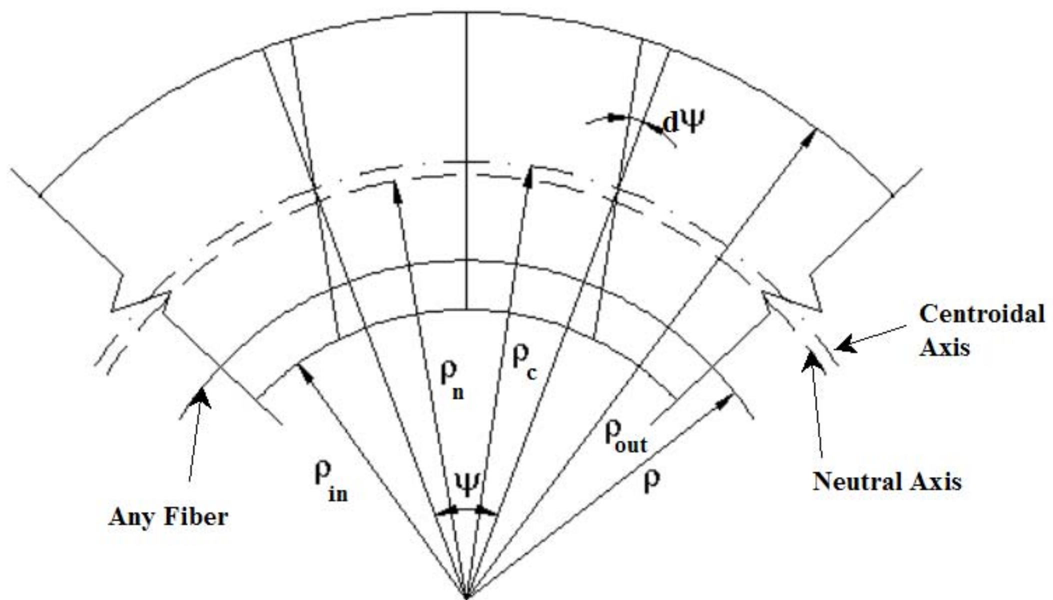

Figure 2-6 Curved bar in pure bending

Hence, the total plastic or ultimate resisting moment (M_{ult}), of the beam is given by the product of the resultant forces and the length of bending arm.

$$M_{ult} = F_T\left[\frac{e+r}{2}\right] + F_B\left[\frac{r-e}{2}\right] \tag{2-28}$$

If the beam were allowed to rebound elastically from the ultimate resisting moment, M_{ult}, the stress distribution would be given by,

$$\sigma = \frac{M_{ult}.c}{(\rho_n - c)eA} \tag{2-29}$$

where c is the distance of any fiber from the neutral axis. Superimposing the initial stresses (σ_{ys}) on the elastically rebounded stresses, given in Eq. 2-29, the residual stresses are obtained.

2.3.3 Residual Stresses for a Sample Wire Profile

The minimum energy profile was determined for a wire bonded with a span of 20 mm, length of 30 mm and a height offset of 10 mm (Figure 2-7). The objective of the study was to determine the residual stresses in the various sections of the wire profile due to the loop formation.

Figure 2-8 shows the curvature at the various sections of the wire. It is interesting to note that the curvatures are highest at the ends of the wires where the wires are bonded and at the location adjacent to the point defining the loop height of the wire.

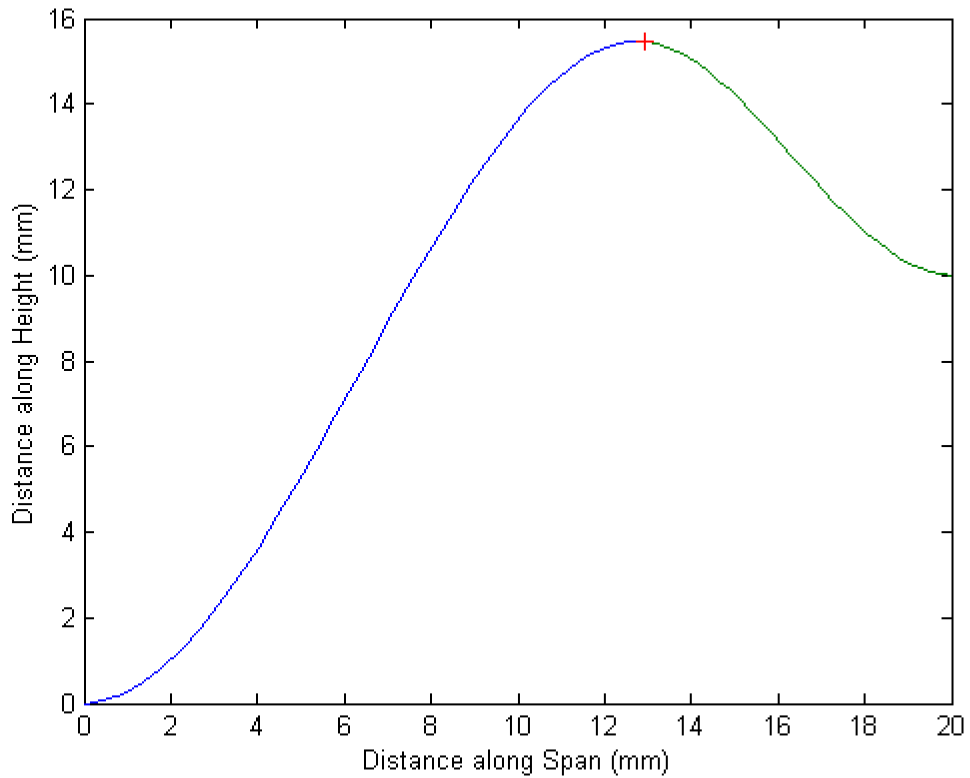

Figure 2-7 Wire profile

The shift in the signs of the curvature suggests that the stresses switch from tensile to compressive near the point defining the loop height and then back to tensile stresses near the opposite edge. The offset of the neutral axis from the centroidal axis has also been determined and is shown in Figure 2-9. The figure shows the shift of the neutral axis is very small when compared to the radius of the wire. This is largely due to the high curvature of the wire in comparison to the radius of cross-section. Hence, it would be prudent to assume coincidental neutral and centroidal axis.

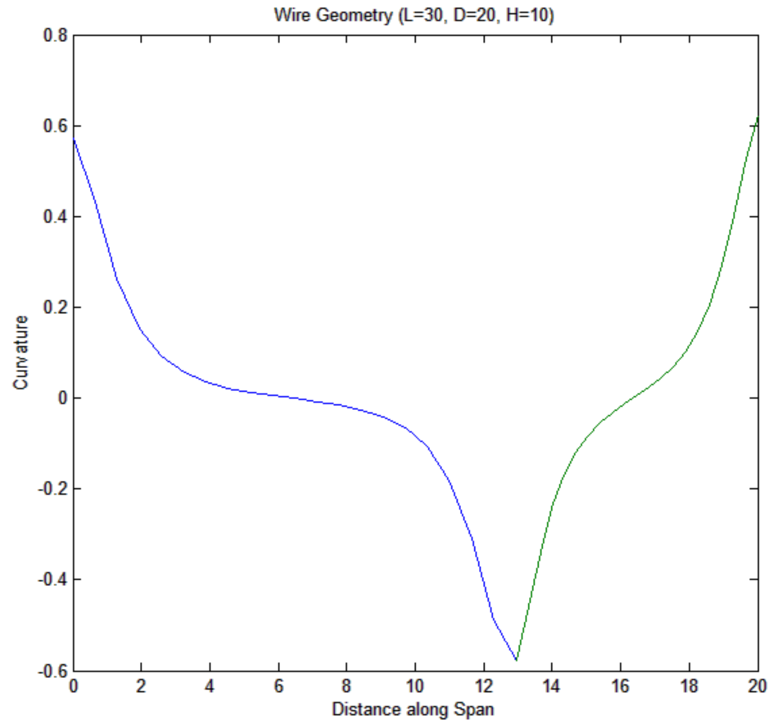

Figure 2-8 Curvature plot

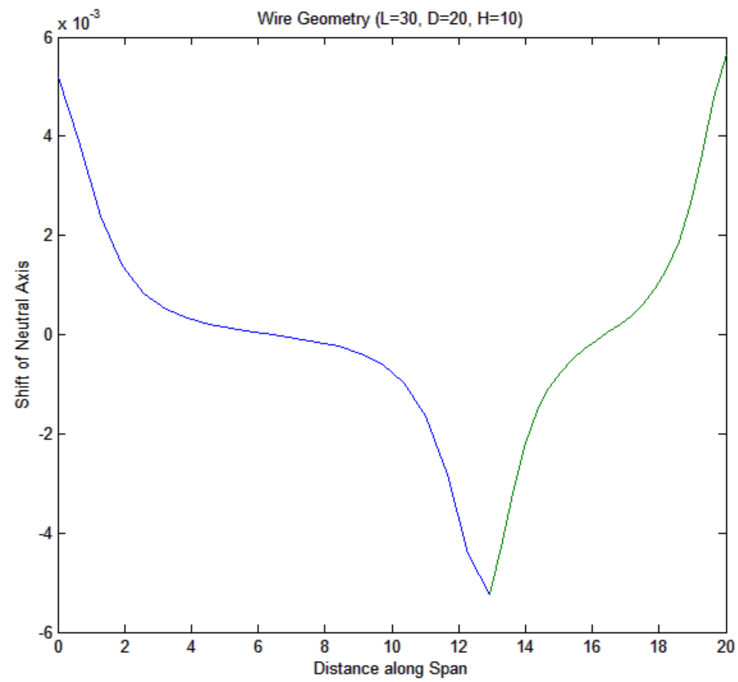

Figure 2-9 Shift of neutral axis

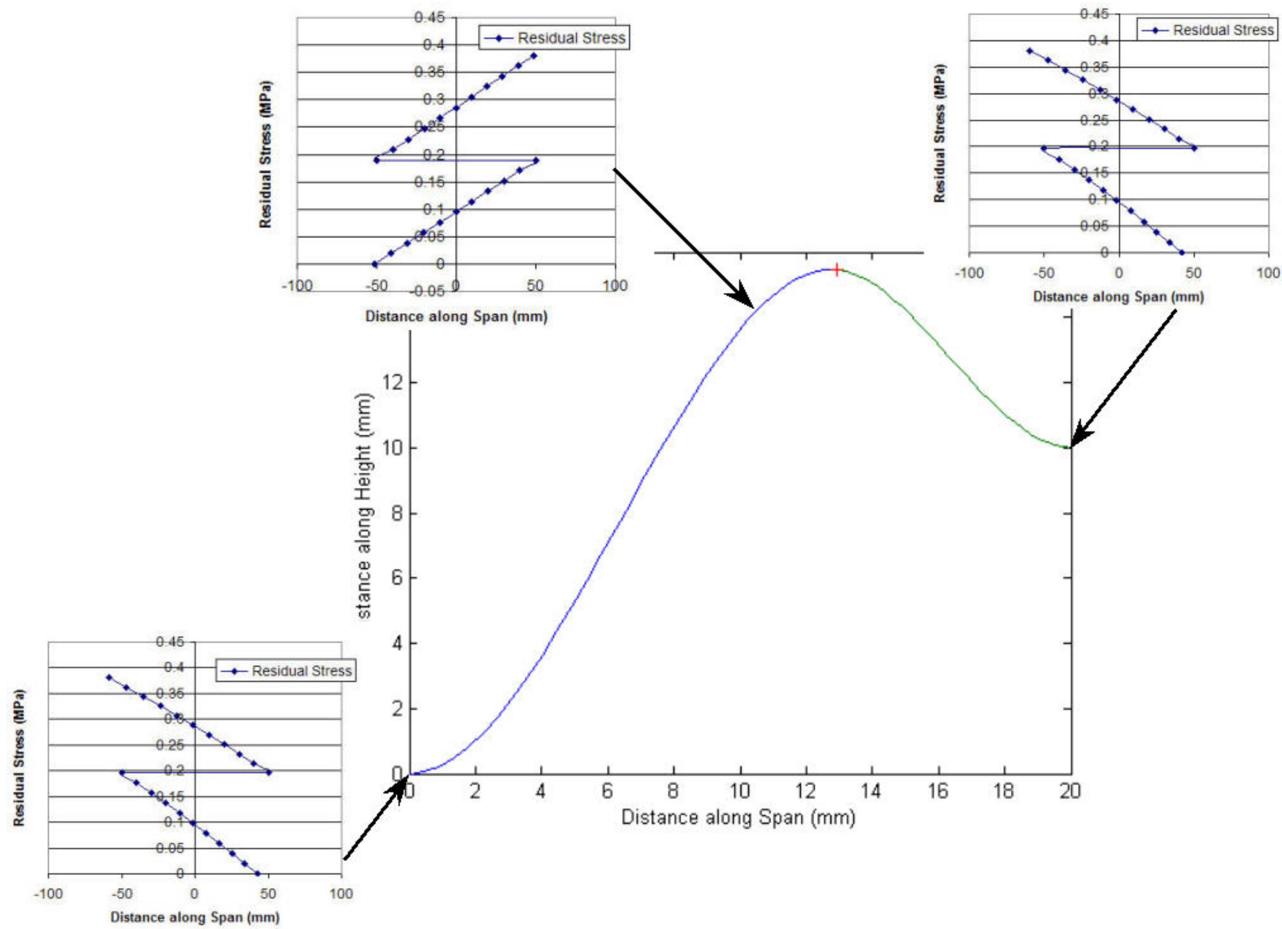

Figure 2-10 Residual stress plot in the wire

Figure 2-10 shows the residual stresses in the various sections of the wire. It is interesting to note that at the heel of the wire the residual stresses are compressive on the top and tensile on the bottom. Compressive initial stresses are advantageous for fatigue cycling while the tensile stresses in the heel are a cause for concern.

2.4 Damage Model

Fatigue damage induced by cyclic stress/strain reversals is exhibited as the initiation and growth of cracks to fracture. Cracks may initiate from defects or microcracks inherent in the wire or bond pad.

2.4.1 Effect of Residual Stresses on the Fatigue Life

As mentioned in Section 2.3, the wires are subjected to high residual stresses due to the loop formation. The aforementioned empirical description on fatigue life pertains to the fully reversed fatigue load with mean stresses of zero. The residual stresses have an important role in the fatigue life prediction of materials. Residual stresses may either improve or adversely affect the endurance limit. These stresses when superimposed with the applied fatigue load alter the mean level of fatigue cycle and the fatigue life for crack nucleation. The affect of residual stress on a material is very similar to the affect of static mechanical stresses superimposed on a cyclic stress. Residual stresses are favorable, if compressive and detrimental, if tensile. However, it is very important to note that the effect of residual stresses introduced due to manufacturing processes become less significant at larger stresses i.e. at low cycle fatigue. The large amplitude of pulsating

stress easily relaxes the residual stresses [Suresh, 1992, Rowland, 1968 and Fox, 1981]. However, for a high cycle fatigue problem, the effects of mean stresses have to be included in the model.

2.4.2 Stress Based Life Approach

For high cycle fatigue ($N_f > 10^4$, N_f – Number of cycles to failure) a stress-based model (Basquin's Power Law), relating the stress amplitude to the number of cycles to failure, is used.

$$\sigma_a = \sigma'_f N_f^b \qquad 2\text{-}30$$

where σ'_f is the fatigue strength coefficient (which, to a good approximation, equals the true fracture strength in a monotonic tension test for most metals) and b is known as the fatigue strength exponent or Basquin's exponent. For most metals, the fatigue strength exponent lies in the range of –0.05 to –0.12. Figure 2-11 shows the S-N curve for a 15-mil wire obtained by doing a cyclic tensile test on the wire specimens using the MTS Tytron micro-fatigue tester. The yield strength of the Al wire was found to be 55 MPa. The stresses used in the plot of the SN curve, shown in Figure 2-11, varied from 50 to 55 MPa. For most steel and copper alloys the endurance limit (or also called as the fatigue limit), σ_e, lies between 35% to 50% of the ultimate tensile strength, σ_{UTS}. Determination of the SN curve with 90% the yield stress may create more plastic damage each cycle resulting in pronounced necking. However, it has been reported that the endurance limit for annealed aluminum alloys is equivalent to the yield stress of the metal [Suresh, 1992, Aluminum Association, 1968]. Hence, the choice of 90% times the yield stress as the

stress amplitude, will hold good for annealed aluminum wires. Similarly, tests were repeated for a 8-mil wire to determine the fatigue coefficients.

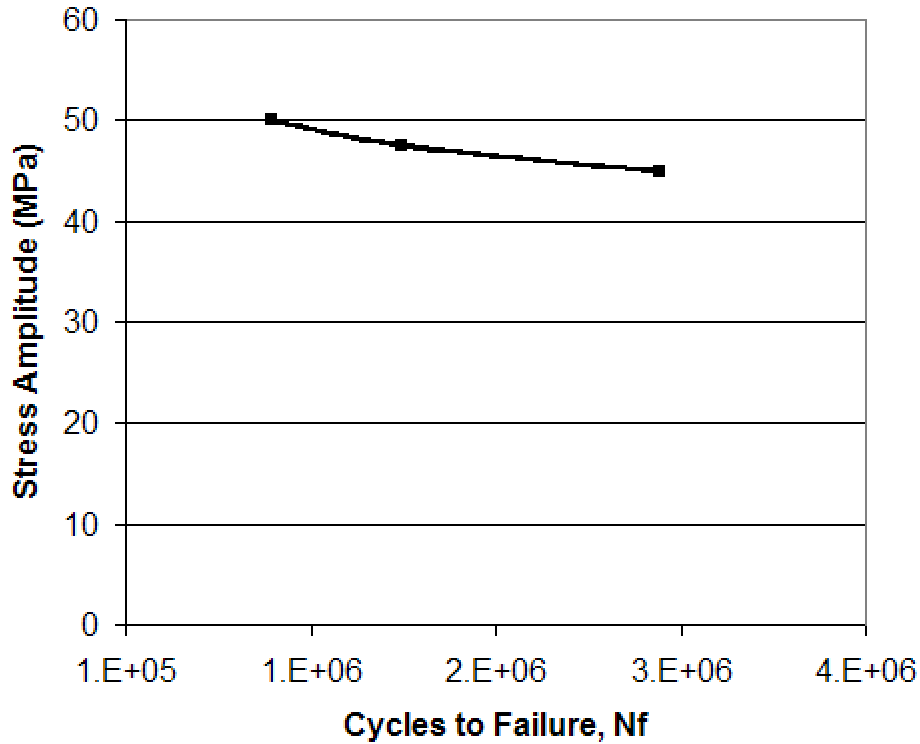

Figure 2-11 S-N curve for a 15 mil wire

The fatigue constants for an 8-mil wire are σ'_f = 194 and b = -0.097, while for the 15-mil wire it is σ'_f = 167 and b = -0.087. However, with an inclusion of tensile mean stresses, σ_0, the fatigue strength coefficient reduces. The modified relationship between the stress amplitude and cycles to failure with the inclusion of tensile mean stresses would be,

$$\sigma_a = (\sigma'_f - \sigma_0) N_f^b \qquad \text{2-31}$$

2.4.3 Strain Based Approach to Total Life

The actual testing of the power modules provide cycles to failure <3000 cycles, which makes the assumption of high cycle fatigue invalid. Hence, a strain range based approach should be used for such problems that face huge stress amplitudes.

Coffin [Coffin, 1954] and Manson [Manson, 1954] working independently on thermal fatigue problems proposed a model to characterize the fatigue life based on the plastic strain amplitude. The plastic strain range is related to the cycles to failure by the following relation,

$$\frac{\Delta\varepsilon_p}{2} = \varepsilon'_f N_f^c \qquad \text{2-32}$$

where ε'_f is the fatigue ductility coefficient (which is experimentally found to be approximately equal to the true fracture ductility in monotonic tension) and c is the fatigue ductility exponent (which is in the range of –0.5 to –0.7 for most metals).

The fatigue constants for low cycle fatigue for the aluminum wire are determined from literature as $\varepsilon'_f = 1.8$ and $c = -0.69$ [Suresh, 1992 and Deyhim et al., 1996].

The strain life based approach to fatigue design has the elastic and plastic components. The total strain amplitude in a constant strain amplitude test, $\Delta\varepsilon/2$, can be written in terms of the elastic and plastic strain amplitudes, $\Delta\varepsilon_e/2$ and $\Delta\varepsilon_p/2$ respectively, as,

$$\frac{\Delta\varepsilon}{2} = \frac{\Delta\varepsilon_e}{2} + \frac{\Delta\varepsilon_p}{2} \qquad \text{2-33}$$

Combining Eq. 2-31, 2-32 and 2-33, the total strain amplitude can be expressed in terms of the cycles to failure as,

$$\frac{\Delta\varepsilon}{2} = \frac{(\sigma_f{}' - \sigma_0)}{E}(N_f)^b + \varepsilon'_f N_f^c \qquad \text{2-34}$$

Eq. 2-34 is essentially a superposition of the elastic and plastic strain amplitudes. For an aluminum wire whose modulus was determined to be 41 GPa with yield strength of 55 MPa, the strain amplitudes vs. cycles to failure were plotted. Figure 3-22 shows the cycles to failure for various strain amplitudes derived from a pure stress-based, strain-based and a method based on the superposition of the elastic and plastic strain amplitudes. The figure also has the effect of mean stresses (55 MPa), represented through dotted lines. The mean stresses are critical to the Basquin's relation, which is used to estimate the high cycle fatigue to failure. However, for low cycle fatigue problems ($N_f < 10^4$), the effect of residual stresses is insignificant. This study serves as a good validation to exclude the effect of mean stresses for the low cycle fatigue problems.

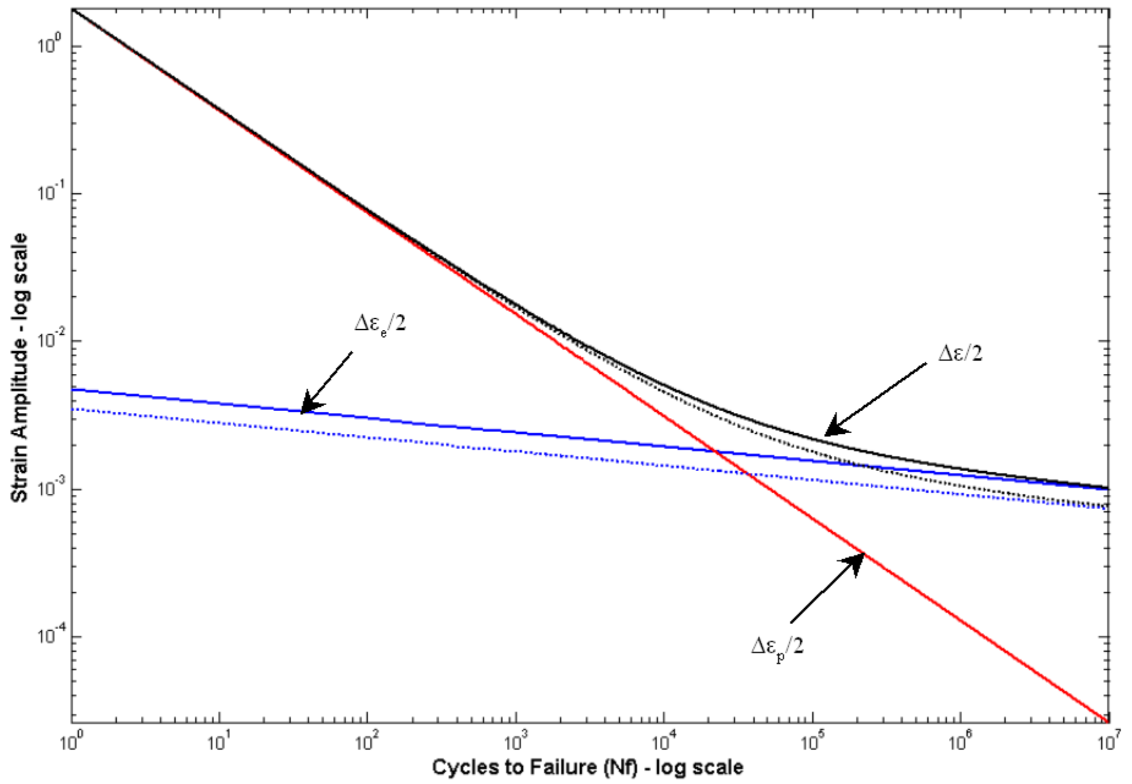

Figure 2-12 Strain amplitude vs. cycles to failure

Figure 2-13 shows a flowchart with the summary of steps involved in the first order PoF based wire flexure model.

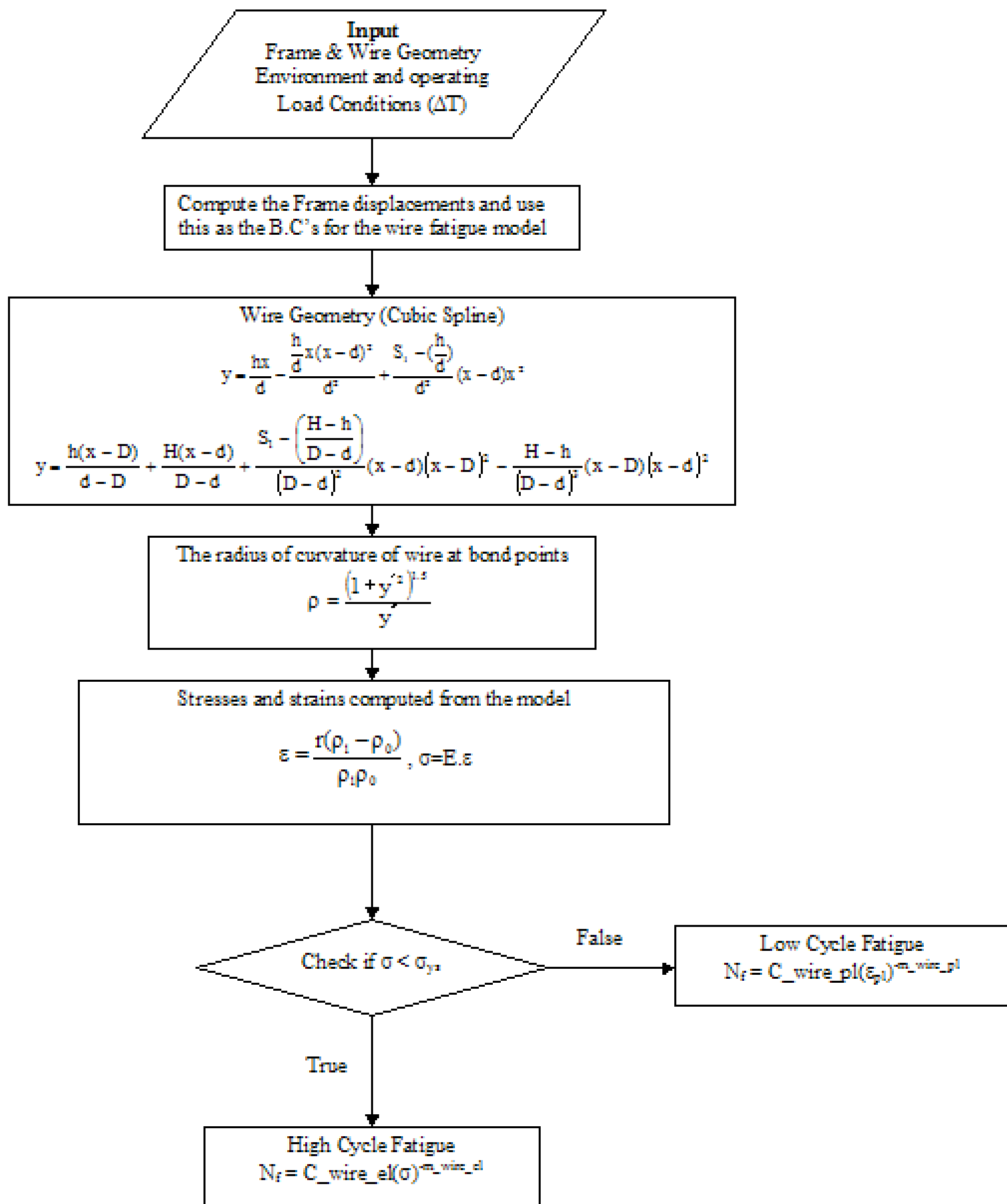

Figure 2-13 Flowchart of model

Chapter 3: Assumptions and Validation Studies

3.1 Introduction

This chapter has been mainly dedicated to explore more into the analytical model, its validation, its shortcomings and possible improvements. Sensitivity analysis has been performed by modifying some of the key parameters used in the design of wirebonded interconnections. The key parameters described this chapter include, length, span, height offset of wire and frame properties that control the frame displacements. The overall objective is to design the best possible wirebonded interconnection based on the imposed constraints.

3.2 FE Validation of the Energy Based Approach

This study was performed with the objective of validating the energy-based approach used to determine the wire profiles and to justify the approach of using two piecewise polynomial curves to represent the wire profile.

A test wire of span 6.3 mm with a height offset of 3 mm was modeled. The energy-based model was used to determine the stress-free wire profile. On heating the wire by 100°C, the wire profile changes and the energy-based model makes a prediction of what the new profile would look like. This has been crosschecked against finite element results from ABAQUS obtained for loading of the stress free wire profile. The wire has been represented using 58 beam elements. It should be noted that the beam element used in ABAQUS, were C^1 continuous. The difference between the energy based

model and the FE model is the continuity requirements and the number of elements used to represent the wire profile. The energy-based model uses only two curves that are C^2 continuous. Figure 3-1 shows the deformed wire profiles obtained through both the approaches (for magnification purpose the deformations have been scaled 10 times). It is obvious from the figure that the energy-based model captures the true behavior of the wire after thermal cycling. Hence, it can be concluded that the trend has been captured pretty well by the cubic spline even with just two curves (one reference point). This test also serves as a validation study for the proper implementation of the energy minimization routine.

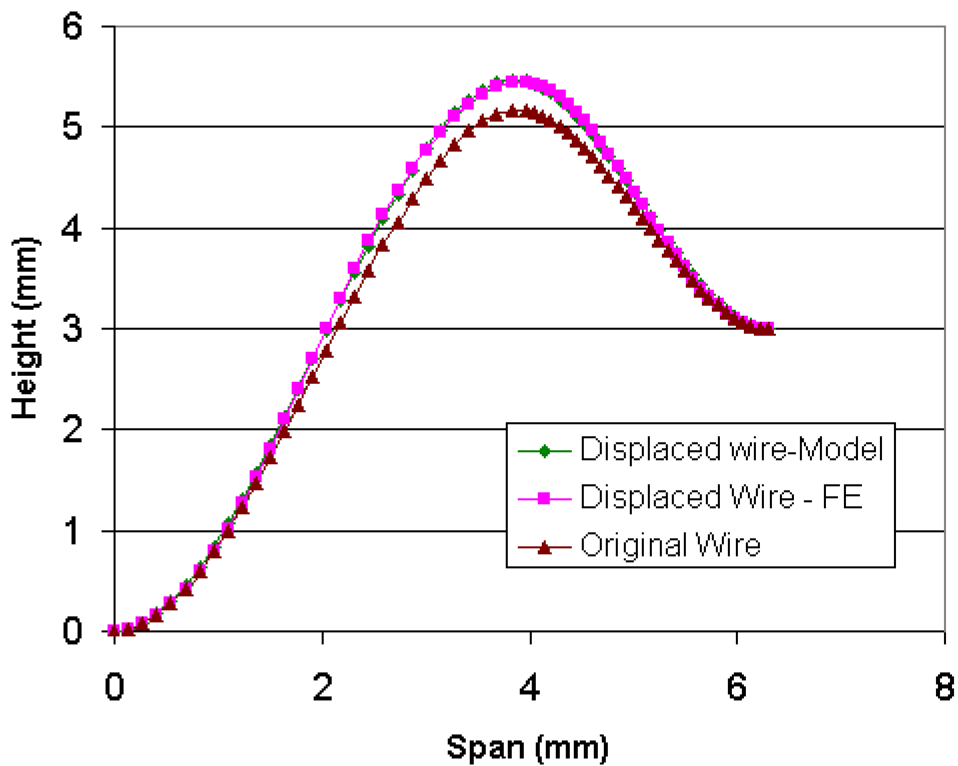

Figure 3-1 Deformed wire profile from energy-based model and FE

3.3 Thermal Cycling Tests

Thermal cycling experiments were conducted by means of a liquid-to-liquid thermal shock chamber. Five modules similar to the ones shown in Figure 2-1 were placed in a Thermal Shock Chamber to be cycled from –40° C to 125° C. The wire bonds were assigned values 1-12 counting from left to right shown below in Figure 3-2.

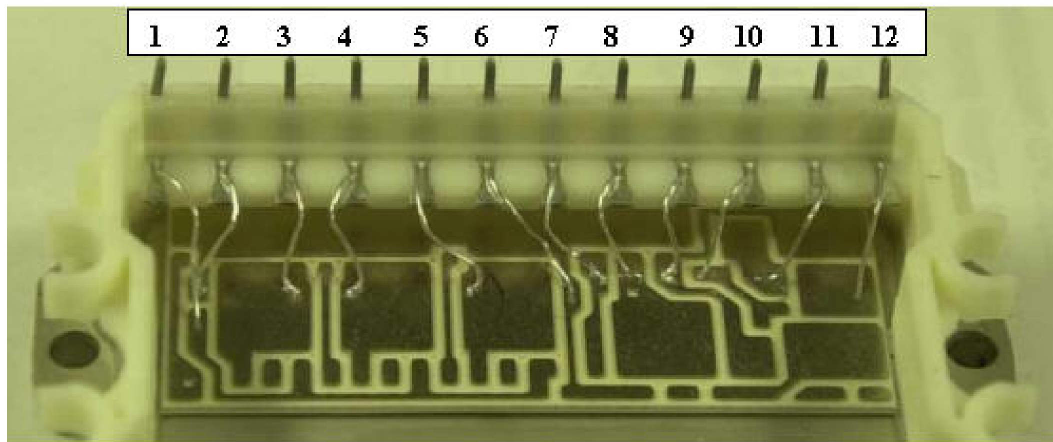

Figure 3-2 Module with the bond # shown

One thermal cycle consisted of placing the modules in the cold bath for 3 minutes to bring the module temperature to –40° C, and then transiting to the hot bath for 3 minutes to bring the modules temperature up to 125° C. The transition time between baths was approximately 5 seconds through ambient air conditions of 25° C. The temperature profile is shown in Figure 3-3.

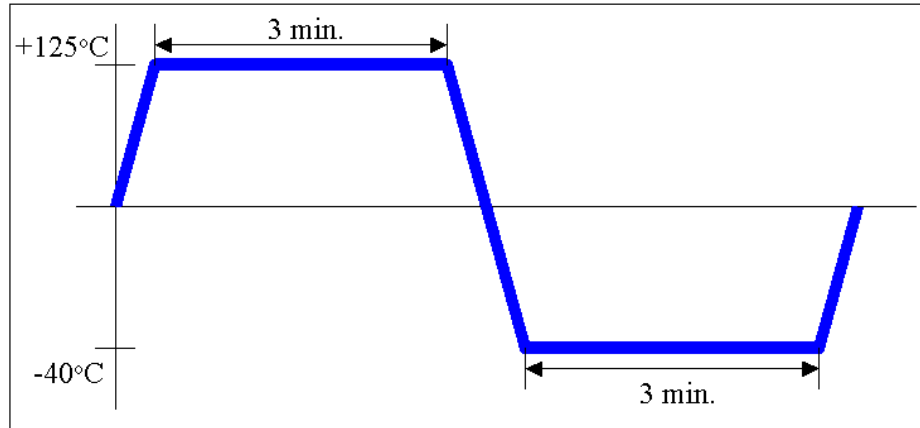

Figure 3-3 Thermal cycling load profile

After each test, all wire bonds on each module were tested for continuity using a multimeter as well as visual inspection. Upon failure of any wire-bond, the failure site was photographed. The failure location for each wirebond was photographed to determine the location and mode of failure (Figure 3-4). Each wirebond failed at the heel of the wedge bond, where the wire was attached to its respective bond pad. The wires did not experience bond lift-off, and the bond to the DBC kept its integrity for all wirebonds.

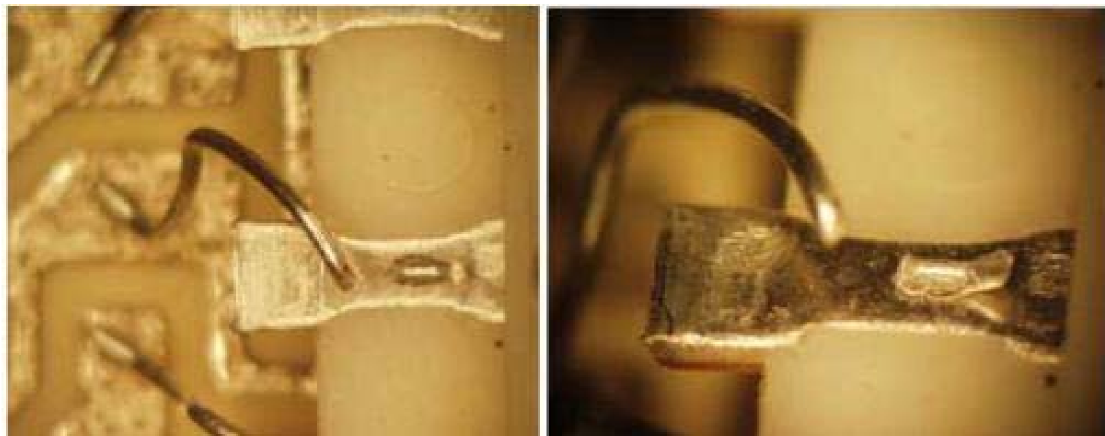

Figure 3-4 Heel crack failure in wire #9 after 1125 cycle

3.3.1 Comparison with the Analytical Model

The number of cycles to failure obtained from the experiments was verified against the output from the model. For the high ΔT that the module experienced during the temperature cycling tests, the strains were very high and it has been assumed that the total strains were approximately equal to the plastic strains. Figure 3-5 shows a graph with the experimental and output values from the model. It is observed that the energy-based model gives a conservative result. This is largely due to the underlying idealistic assumptions used in the model. The actual wires in the modules have certain twists; wire thinning near the heel, which have not been accounted for, in the model. Any small variations in the strains/stresses would be magnified when the cycles to failure are computed since the Coffin-Manson or the Basquin's relations are all power law based. Nevertheless, the model captures the trend observed in the field, though the cycles to failure are on the conservative side. The effect of wire thinning and wire twisting has been more elaborately explained in Chapters 4 and 5 respectively.

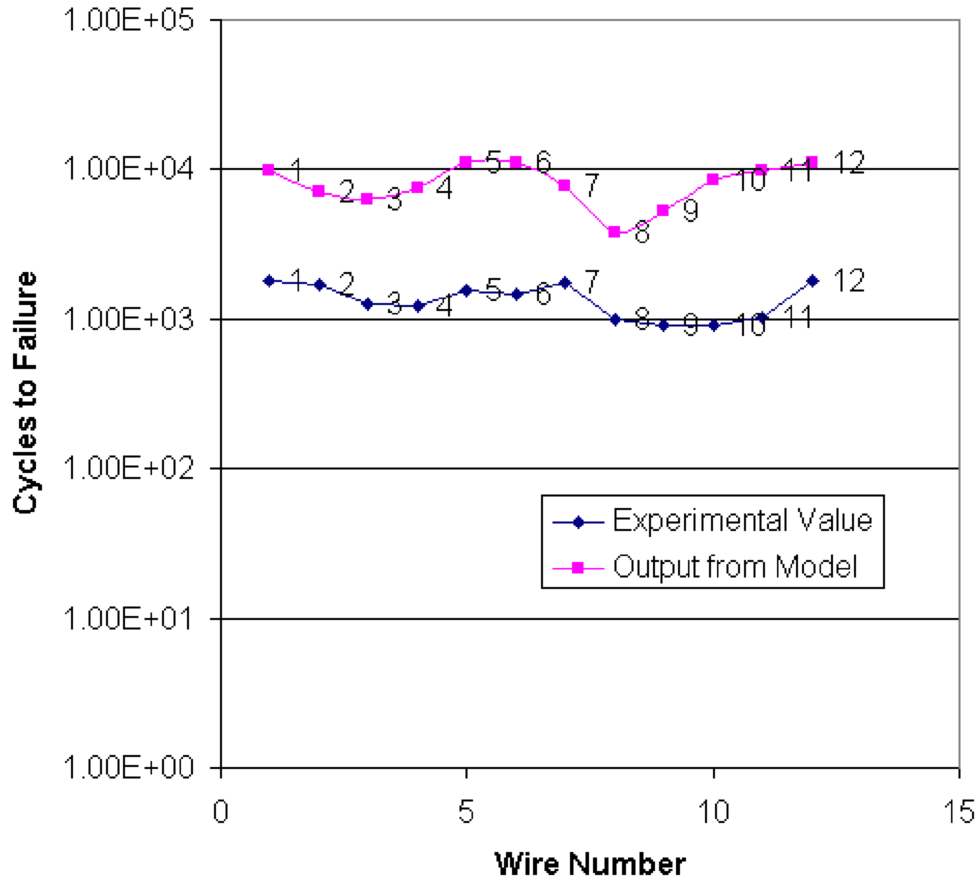

Figure 3-5 Comparison of output from model and experiment

3.4 Sensitivity Analysis

Sensitivity analysis has been done to study the effect of Length, Height and Span of the wire on the fatigue life. It is very important to know that these conclusions are based purely on the mechanical reliability of the wires when exposed to thermal cycling. However, from electrical perspective, one would prefer shorter wire lengths and spacing to reduce the switching time and also to reduce the effects of inductance.

3.4.1 Effect of Wire Length on the Wire Life

Figure 3-6 shows the wire geometries for various lengths of the wire with constant height of the second bond pad (H = 3.5 mm). The wire lengths shown in the figure vary from 8 mm to 10.75 mm with a step size of 0.25 mm.

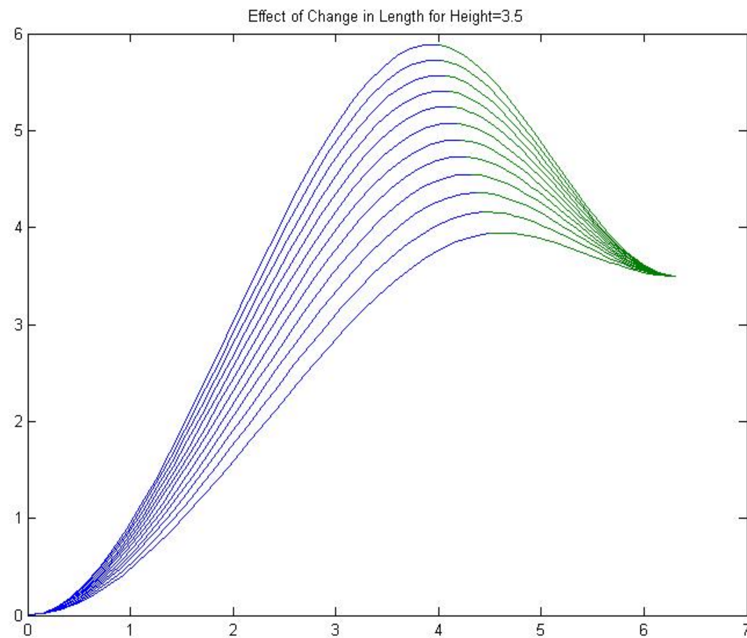

Figure 3-6 Effect of wire length on wire life (H=3.5 mm)

Figure 3-7 and Figure 3-8 show the cycles to failure due to wire flexure for various wire lengths at the lower and upper bond pad. The graphs are plotted for various bond heights. As explained earlier, the stress magnitudes decrease until it reaches a critical value beyond which they start increasing (the increase is very gradual above the critical wire length). It is noteworthy to mention that the stresses near the lower bond pad are not influenced much by the change in the height. However, the effect of variation in

length of the wire is experienced more at the upper bond pad and the stresses are always higher in magnitude. Therefore, a non-zero height, H, would ensure failure to occur first at the upper bond pad.

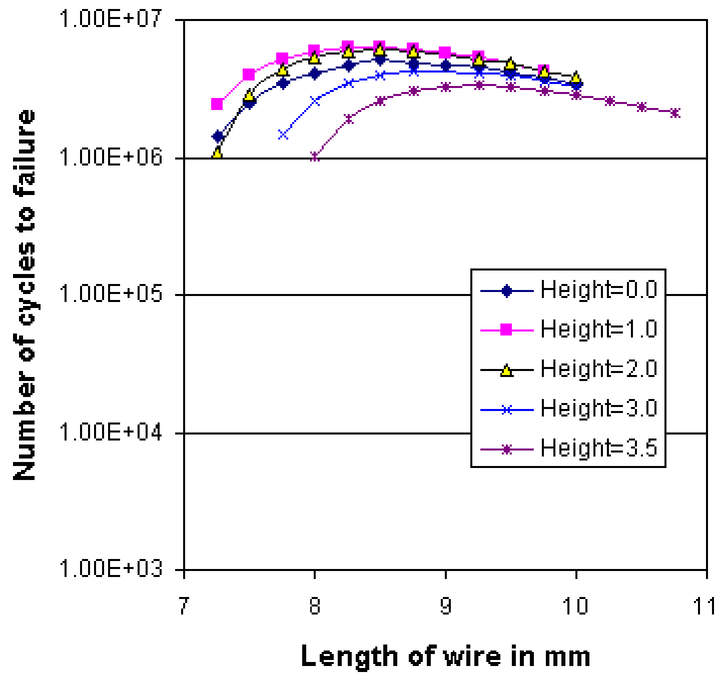

Figure 3-7 Cycles to failure for various wire lengths (lower bond pad)

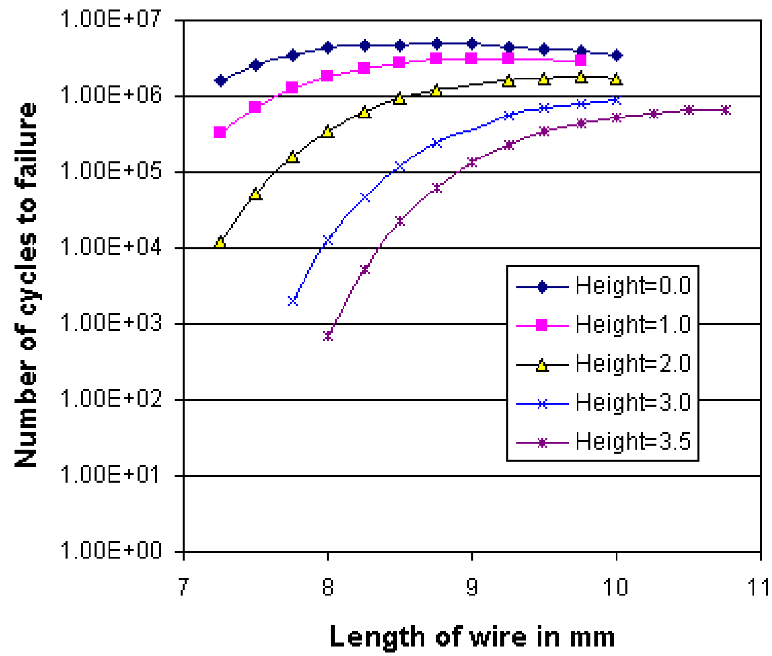

Figure 3-8 Cycles to failure for various wire Lengths (upper bond pad)

3.4.2 Effect of Bond Pad Height

Figure 3-9 shows the wire geometries for various heights with length and span being constant (L=11 mm; D=6.3 mm). The height is varied from 0.0 to 3.9 mm with a step size of 0.3 mm.

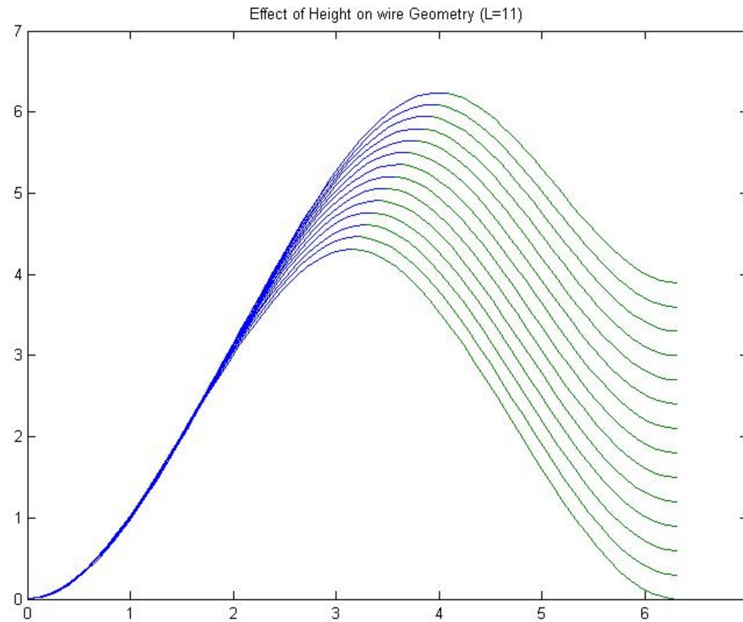

Figure 3-9 Wire profiles for varying bond pad height offset

It is observed from Figure 3-10 that an increase in the bond pad height offset (i.e. increase in H) reduces the cycles to failure. The graph has been plotted for wires with a span of 6.3 mm and with lengths varying from 10 mm to 11.5 mm with a step size of 0.5 mm. Also, from the two concluded analysis it is evident that there is an optimum wire bond length, which can produce the maximum cycles to failure.

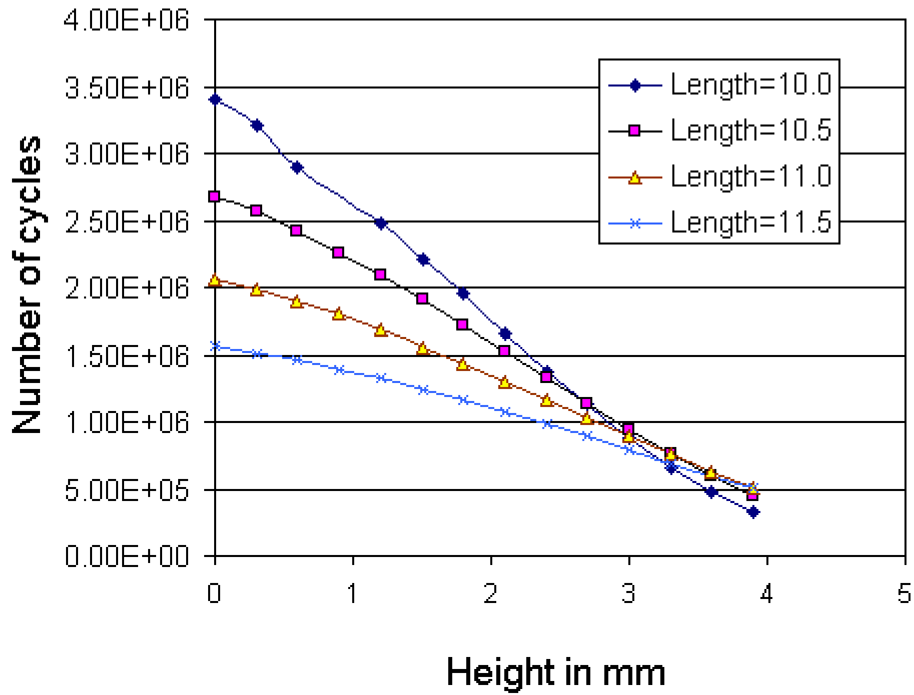

Figure 3-10 Cycles to failure at the upper bond pad

3.4.3 Effect of Wire Span

Figure 3-11 shows the effect of span on the wire life due to heel crack failure occurring near the upper bond pads. This study has been primarily conducted to prove that if the lengths and height offset of a wire are provided as constraints the model still gives the flexibility of obtaining the optimum wire span, which can increase the cycles to failure.

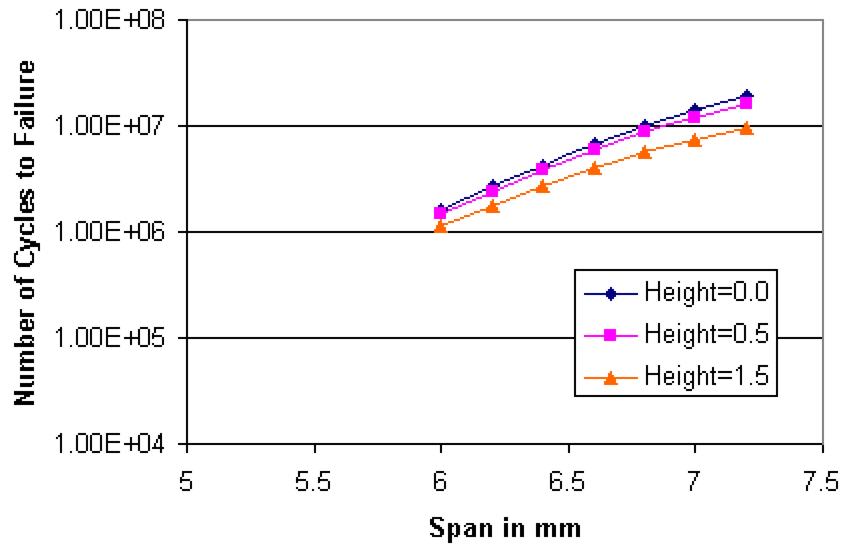

Figure 3-11 Effect of wire span on wire life (upper bond pad)

The figure also shows that as the span of the wire increases the cycles to failure increases i.e. the stresses or the strains reduce with increase in span. The mathematical reasoning for this trend is explained through a simplified version of the cubic spline explained in Appendix C.

3.4.4 Effect of Wire Thickness

The model developed by Hu-Pecht-Dasgupta shows a linear relationship between the wire thickness and the bending stresses [Hu et al., 1991]. The current energy-based model determines the stresses from the wire loop profiles before and after thermal cycling. Hence, the linearity in the stresses for various wire thickness has to be proved in this case also. Hence, a study was conducted for various wire diameters ranging from 0.05 mm to 0.3 mm, in steps of 0.05 mm, and the stresses were plotted corresponding to

the various wire diameters. The curve is seen to follow a linear trend (Figure 3-12) thus proving as credibility to the model. Hence, this study also concludes that a smaller wire thickness is always preferred for better reliability from wire flexure standpoint.

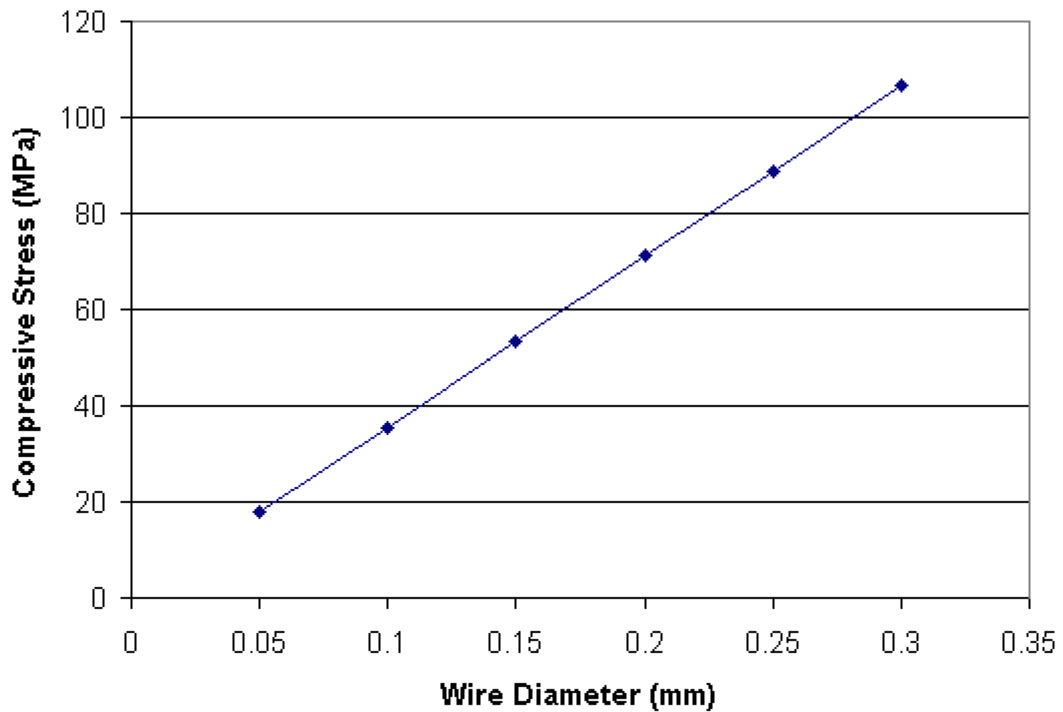

Figure 3-12 Effect of wire thickness

3.4.5 Effect of Thermal Load

The model uses the wire curvature before and after thermal cycling to determine the bending stresses. For linear elastic behavior, one would expect thermal load to be linearly proportional to the bending stresses.

Hence, a study was conducted with a stepwise increase in the thermal load, varying from 10°C to 100°C. Figure 3-13 shows that the bending stresses vary linearly with a stepwise increase in the thermal cycling load.

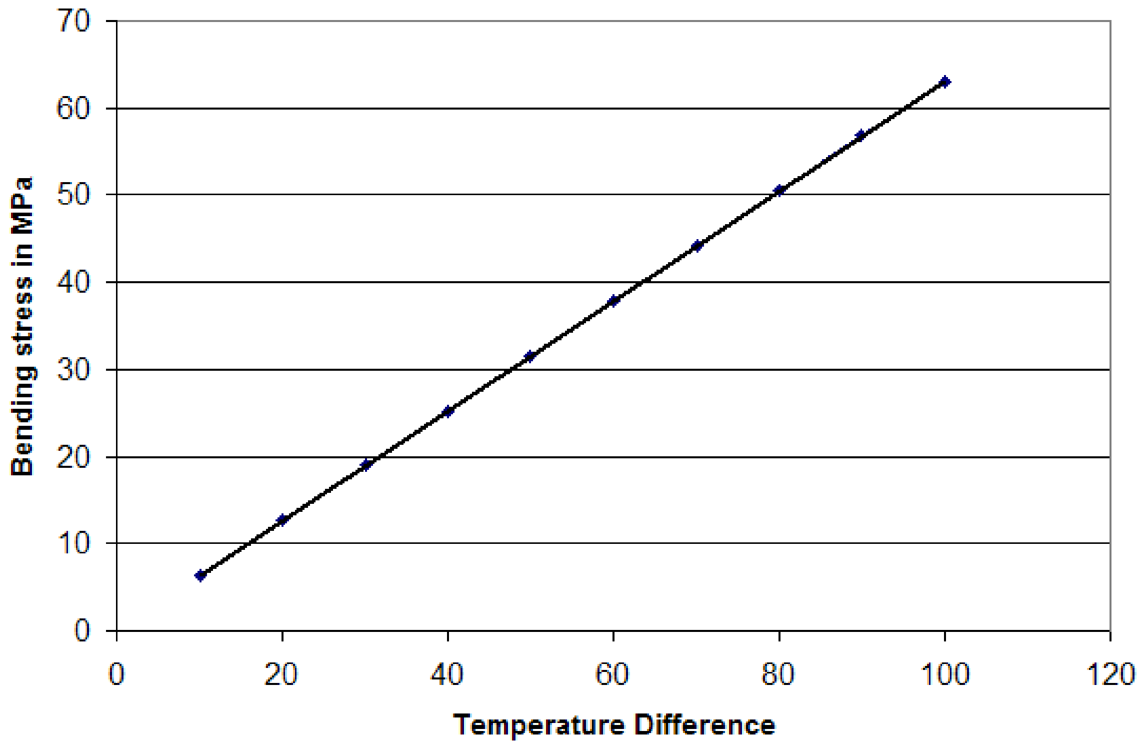

Figure 3-13 Effect of stepwise increase in temperature

3.5 Significance of Frame Displacement

This section explains the significance of the frame displacement model and how it controls the reliability of the wire failure due to flexure. This study is essential for setting suitable guidelines. This section also explains the significance and limitations of the models described in the earlier chapter.

On heating the power module, the frame displaces and places additional strains on the wire. The significance of the frame displacement is studied by modeling the frame,

shown in Figure 2-1, separately using FEM. The discretized model of a typical power module explained earlier is shown in Figure 3-14. Considering symmetry only a quarter portion of the module is modeled. The wires shown in the figure have been used just for demonstration purpose but they are not actually used in the analysis.

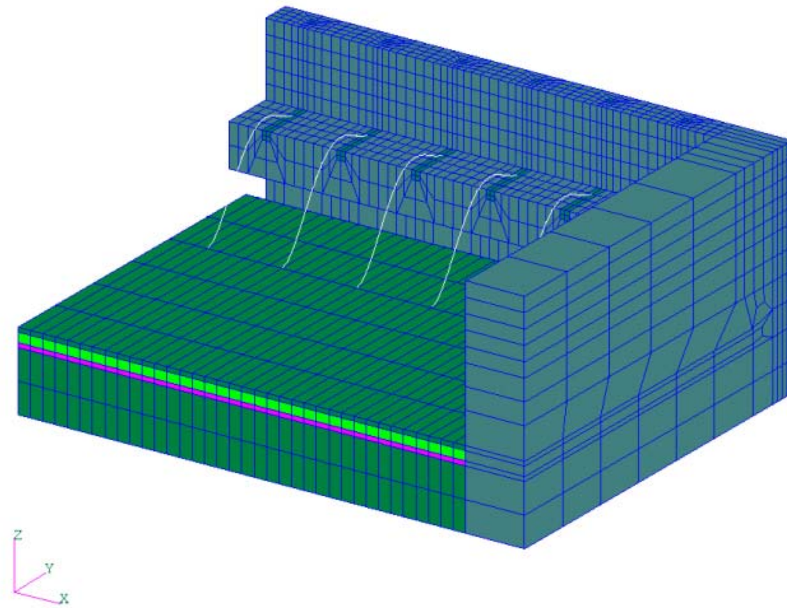

Figure 3-14 Finite element mesh

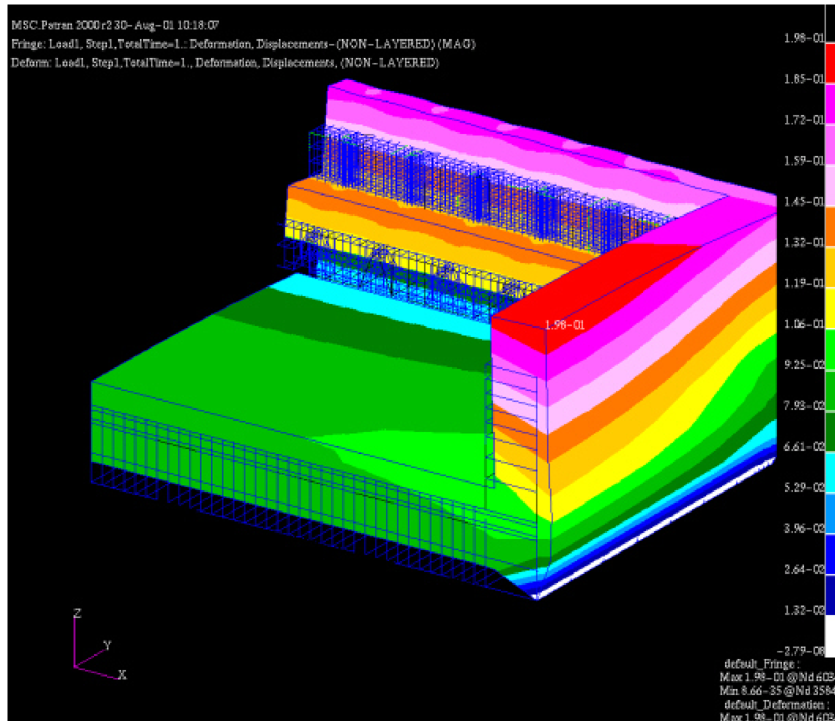

Figure 3-15 Displacement contour

A thermo-mechanical load, with a ΔT of 100°C, is applied and the frame displacements are calculated. Figure 3-15 shows the displaced contour.

The u-displacements are small while the v and w displacements are significant as seen from the graph on Figure 3-16. These displacements could prove significant in reducing/increasing the strains in the wire. It becomes evident from the study that the displacements of the frame have to be represented properly for accurate prediction of the stresses in the wire. One simple assumption is to assume that the frame displaces by $\alpha_f \Delta T$ and the substrate expands by $\alpha_s \Delta T$ (α_f and α_s are the coefficient of thermal expansions of the frame and substrate respectively). However, this gives a conservative result. Also, a notable feature in this study is that the displacements are similar in magnitude across the various leads and also the u-displacements are insignificant. Hence, it would be sufficient

to consider a two dimensional plane strain analysis than a rigorous three-dimensional analysis.

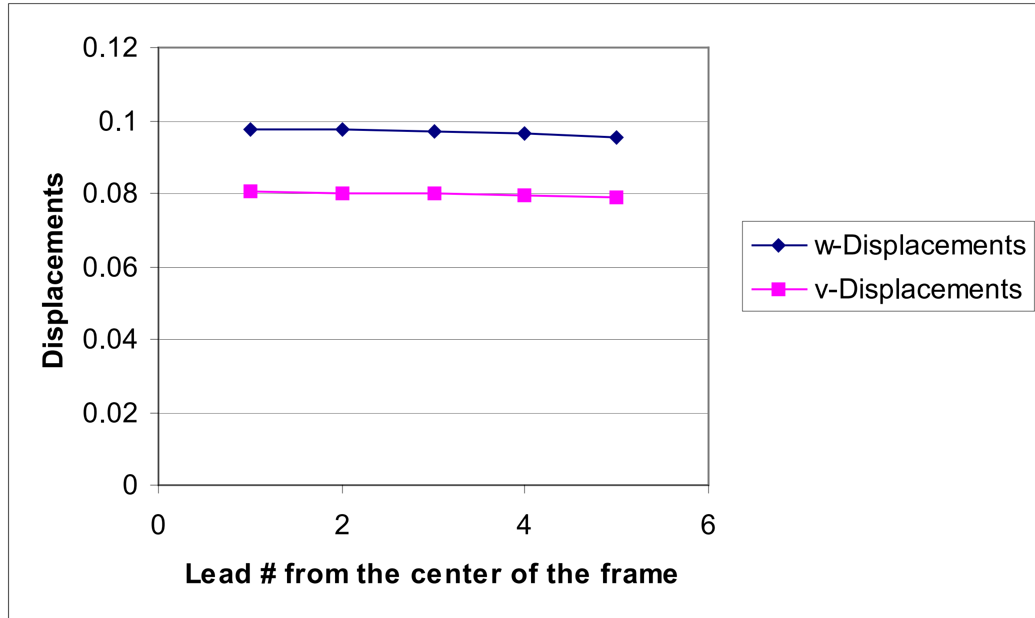

Figure 3-16 Frame displacements at the various lead numbers

3.5.1 Effect of Frame Displacements on the Flexural Stresses

The above finite element study concludes that the displacements in the frame are significant and have to be incorporated into the wire flexure model. However, it is not very clear from the study if the frame displacements are detrimental or beneficial for reducing the flexural stresses. A good knowledge on the influence of the frame helps in designing reliable power module.

When the wire in the power module is heated, the wire expands and this change in curvature of the wire at the heel causes the flexural stresses. If the change in curvature due to thermal cycling can be nullified by letting the frame displace to predetermined levels, then the flexural stresses can be reduced. This can be achieved either by choosing

a suitable CTE of the frame or by increasing/decreasing the height offset. Changing the height offset would mean a different set of key parameters, which includes optimum wire length and span of wire that produces the maximum cycles to failure. Hence, our current study focuses on varying the CTE of the frame and its effect on the flexural stresses in the heel of the wire.

3.5.2 Effect of CTE on the Heel Stresses in the Wire

Figure 3-17 shows a two-dimensional plane strain model of a power module. The CTE mismatch between the wire and the bond pad will induce high shear stresses coupled with wire flexural stresses. Hence, the bond pad material has been so chosen that the CTE matches with the wire material and this would eliminate the wire lift-off problem due to shear. The stress contours in Figure 3-18 shows the absence of the stresses arising due to CTE mismatch.

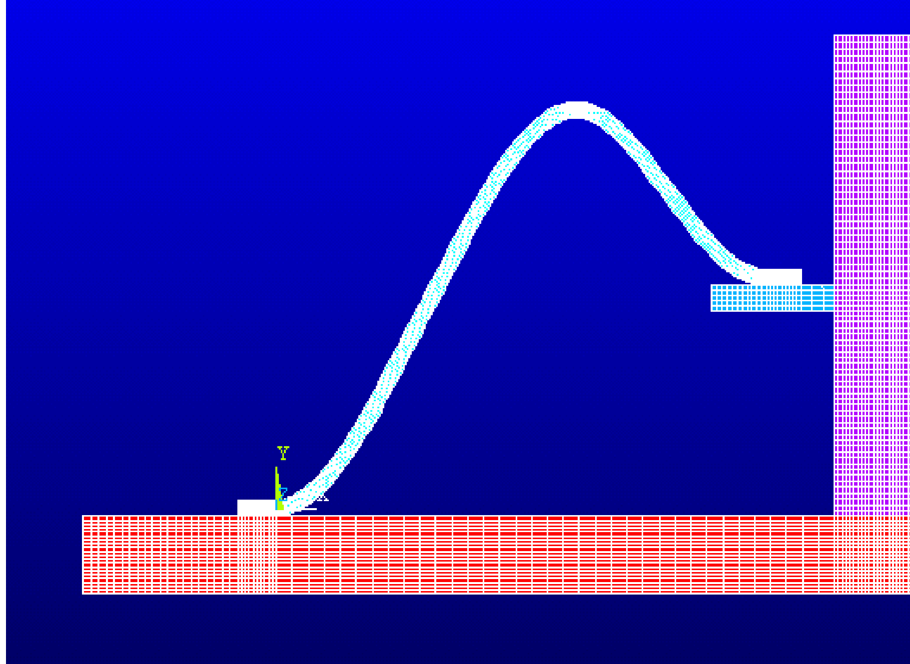

Figure 3-17 Frame displacement model

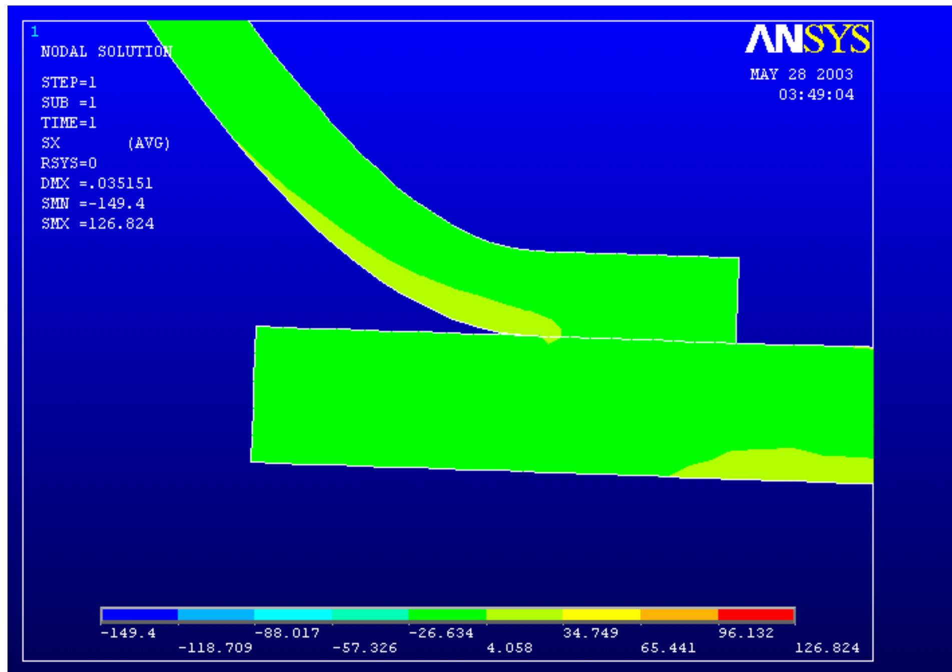

Figure 3-18 Heel stresses

The power module is cycled for a ΔT of 200°C. Figure 3-19(a) through (e) show the bending stresses at the heel of the wire. All the figures clearly show that the heel is the critical region. The results for a layer of nodes, across the wire thickness, in the heel of the wire have been chosen for comparison and the bending stress plots are shown in Figure 3-20. It is observed that for no expansion of the frame, high compressive stresses are seen at the top of the wire at the heel. An increase in the CTE of the frame helps the wire to reduce the bending stresses as shown in Figure 3-19(b) and (c). However, as the CTE of the frame increases further, the bending stresses increase in magnitude and become tensile at the top of the wire. It is to be noted that the current study also depends largely on the load cycle used.

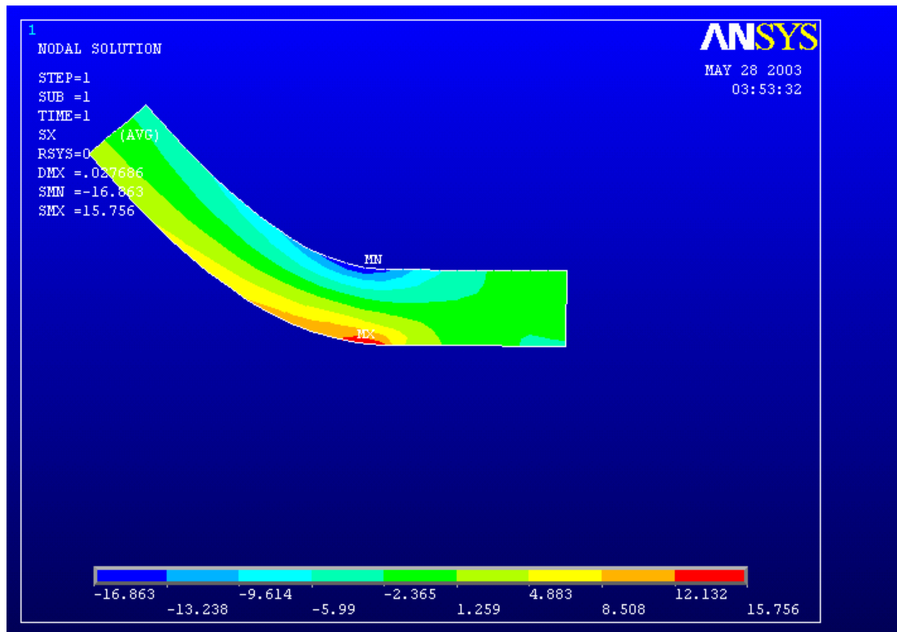

(a) CTE = 0.0

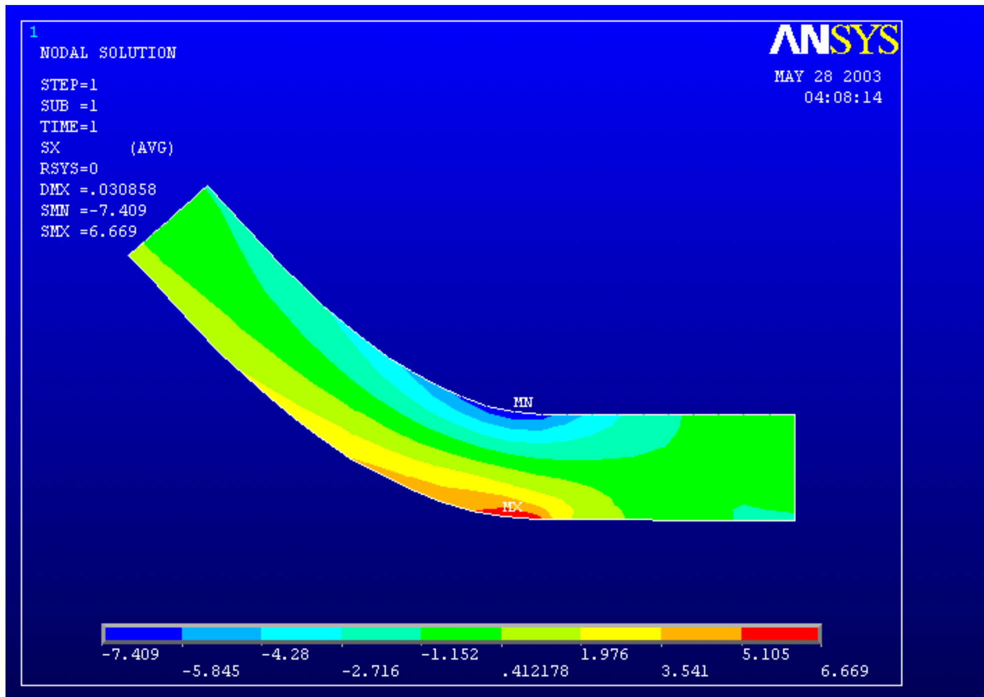

(b) CTE = 20e-6

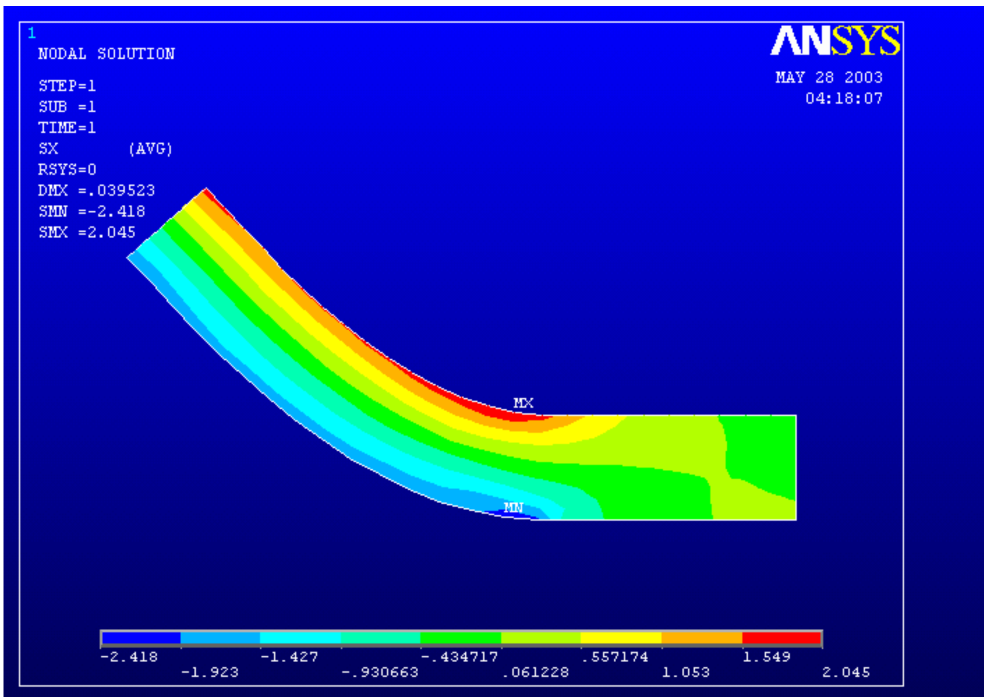

(c) CTE = 40e-6

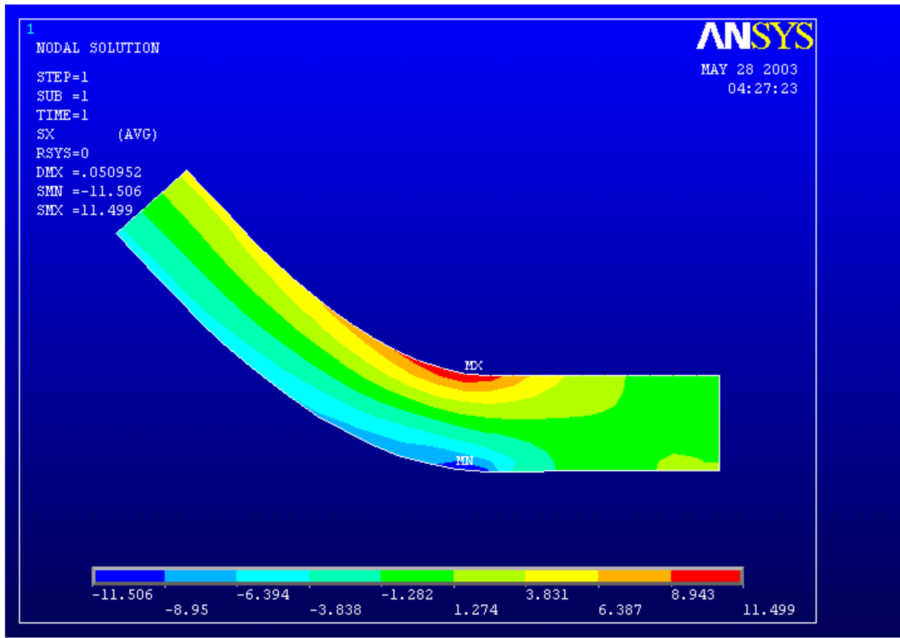

(d) CTE = 60 e-6

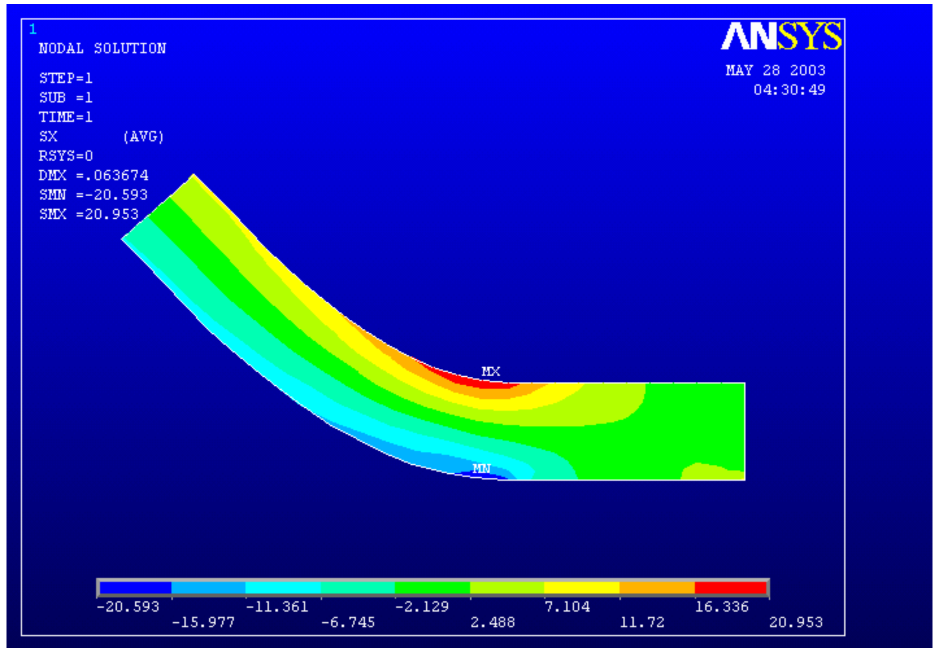

(e) CTE = 80e-6

Figure 3-19 Wire heel stresses at the upper bond pad for various frame CTE's.

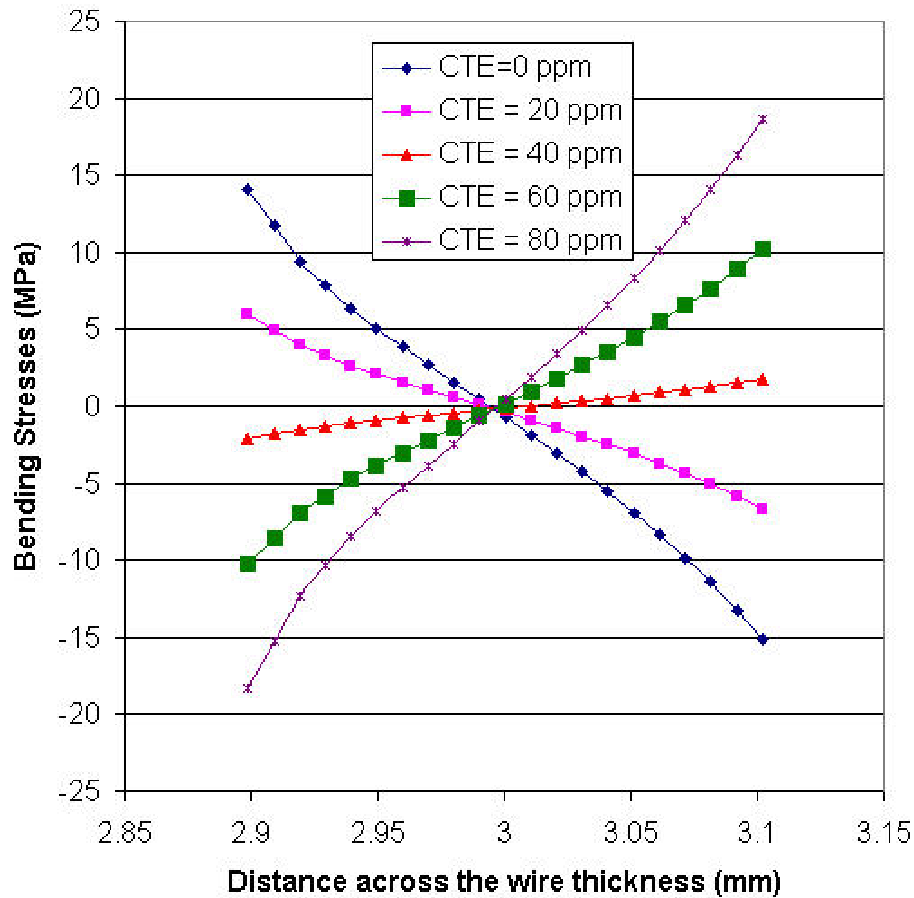

Figure 3-20 Bending stresses at the wire heel for various frame CTE's

Based on a set of constraints imposed (wire geometry, load cycle etc.), a suitable choice of frame material will reduce the stresses at the heel of the wire. Performing a finite element analysis for each design is very time consuming and hence a very simple analytical model has been proposed (Appendix A) to solve for the frame displacements. This model considers the linear expansion and the bending of the frame.

3.6 Model Assumptions

The model assumes that the manufacturing process is perfect and no additional stresses are placed due to the manufacturing process. The manufacturing errors include the cracking caused at the heel of the wire due to the tool motion and bonding machine vibration. Residual stresses induced during the bond formation will not be critical for low cycle fatigue problems (less than 10^4 cycles) for the aluminum wire chosen in the study. However, if other materials are chosen, the SN curve should be re-plotted to study the effects of residual stresses on fatigue cycling.

The model determines the most stable configuration that a wire would prefer to occupy before and after the load cycle. Based on the change in curvature during these two states before and after thermal cycling the strains are obtained. However, not all the wires are bonded with the minimum energy wire profile and these are sometimes governed by the applications and limitations of the geometry of the power modules. However, pronounced thermal cycling will result in the wire trying to attain a stable configuration after sufficient number of thermal cycles.

The model is very accurate for an idealistically bonded wire and when it is loaded elastically. However, for plastic deformation of the wire, the loading has to be applied gradually and the strains have to be decoupled into elastic and plastic strains. All the wires in the power modules considered in the study failed in less than 3000 cycles. Hence, the bending strains, which hold good even for plastic deformation, have been assumed to be equal to the total strains. The life cycle prediction has been based on these assumption of strains.

During the loop formation in wedge bonding, the movement of the axis of the bonding wedge feed hole is usually aligned with the center line of the first bond, so that the wire can be fed freely through the hole in the wedge. The width offset between the bond places additional strains in the wire. In addition, the model assumes there is no wire thinning near the bonding locations. The strains have been calculated based on the theory of pure bending of curved beams. The Euler-Bernoulli equations derived in Chapter 2 are valid only for the local model and cease to exist near the reduced cross section of the wire (caused by wire thinning). There is an additional moment/shear force acting in the reduced cross section of the wire. This influence can be introduced by means of a stress concentration parameter, K_s. K_s accounts for the effects of wire thinning and twisting. The determination of K_s for the wires used in the study is explained in Chapter 4.

The minimum energy wire profiles determined by the model could be used by commercial finite element codes to solve for the bending stresses. Also, these finite element codes add the additional flexibility of including the effects of wire thinning near the heel by suitable modification of the geometry. The solution time for an elastic loading of a thermomechanical load for a discretized two dimensional model is very small, depending on the number of nodes and degrees of freedom. However, sufficient time is involved in modeling and meshing these complicated geometries. To avoid the huge modeling time, an automated program has been written to generate the ANSYS log files. This approach has been implemented to generate 3D wire profiles in Chapters 4 and 5. The analytical model is preferred over the analytical model for checking reliability of existing designs, since it can more accurately model the wire thinning effects. However,

the pure first order physics of failure based model is preferable to derive suitable guidelines and also to determine the optimum geometric parameters.

3.6.1 Further Limitations, if using the Hermite Interpolation Scheme

As explained earlier, the hermite interpolation model explained in the previous chapter, has a C^1 continuity and hence lesser accuracy. For better accuracy with a hermite interpolation scheme, more reference points are needed, which increases the computational time. Also, the hermite interpolation model is based on the user providing the details about the point that defines the loop height (point 2 shown in Figure 2-2). Most of the time, it is very difficult to obtain these details from the actual power module. In addition, thermal cycling can always result in the wire profile taking a new configuration after a few load cycles. Hence, a study was conducted to observe the sensitivity of the model to small variations in the location of the reference point 2. This dependence on the outputs is seen in Figure 3-21. From a design point of view, the model seems appropriate when the point is defined within +/-0.5 mm. However, this is problem dependent i.e. depends on the wire length, span, height and load applied.

Figure 3-22 shows the life as a function of wire span. The effect of variation in the reference point (point 2 shown in Figure 2-2) to the life has also been plotted in Figure 3-22. Considering these drawbacks, the hermite interpolation scheme in spite of its simplicity was not preferred, unless the user had accurate loop height information.

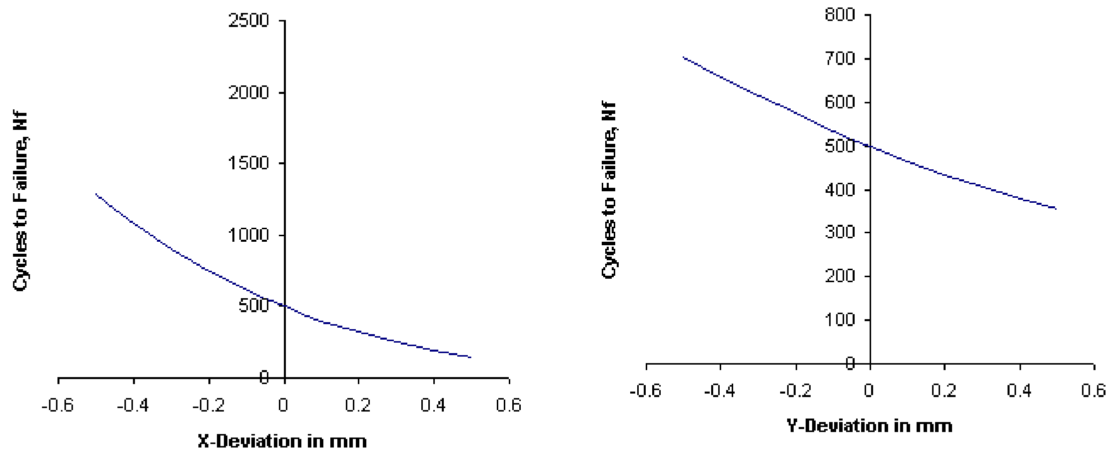

Figure 3-21 Variation in model output due to variation of top point definition

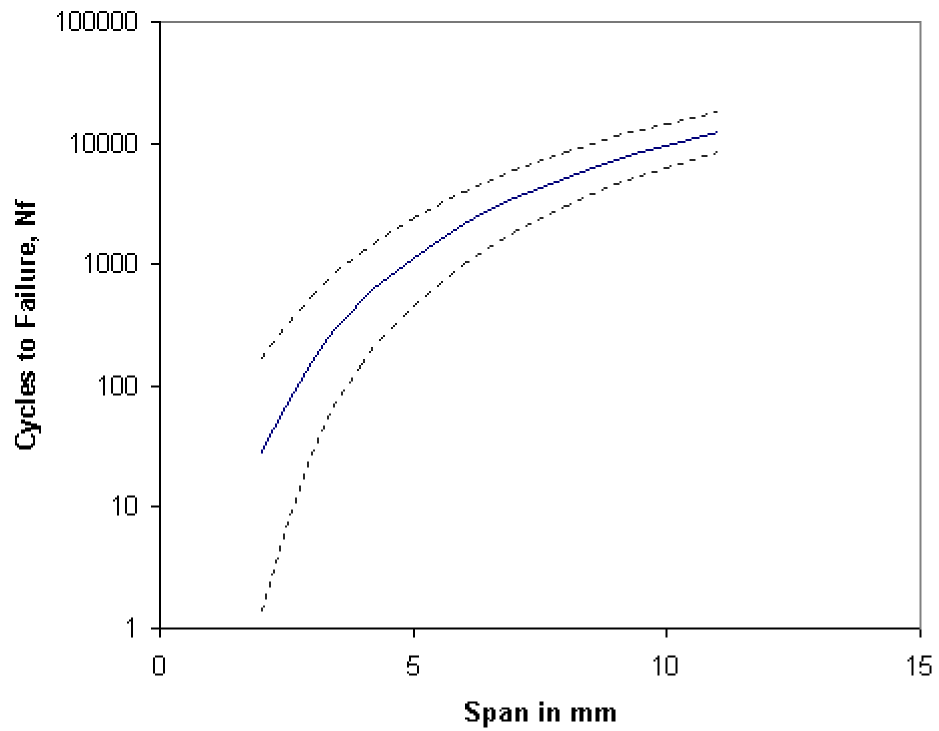

Figure 3-22 Life of wire dependent on wire span length

3.6.2 Disadvantages of the CUBIC Interpolation Scheme

The cubic interpolation scheme was found to be much more accurate in comparison to the Hermite interpolation scheme. The model is certainly useful in providing guidelines about the important parameters that influence the reliability of the wirebonded connections. The main disadvantage with the energy-based cubic spline is the computation time involved in trying to minimize the strain energy. The solution process involves numerical differentiation, integration and a numerical solver (Levenberg-Marquardt Algorithm) for solving a set of non-linear equations. This process has to be repeated for the configuration of the wire before and after heating. Appendix C provides a much simpler and quicker version of the model.

Chapter 4: Ultrasonic Bonding and its Effect on Wire Flexural Failure

4.1 Introduction

About 95% of the interconnections in the semiconductor industry are ultrasonically welded in some manner [Harman, 1997]. In the high power devices, thick aluminum wires, which are required to carry a high current, are bonded ultrasonically to various aluminum alloys on the semiconductor chips.

The transducer and the appropriate bonding tool length are chosen to form a resonant structure. An example of a typical transducer is shown in Figure 4-1. One end of the bonding tool carries the transducer. Adjacent to the transducer element is the clamp, which is the location of one of the nodes of the ultrasonic wave signal. The tapering structure that is attached to the clamp is called the horn of the transducer. The horn provides the physical displacements at the welding/bonding tip, located on the tip of the horn, required to produce a satisfactory weld. The tip displacement is usually between 50-600 μin at the excitation frequency of 60 kHz [Crispi et al., 1972]. Several studies have gone into the details of in-situ monitoring of the tip displacements in the ultrasonic bonding equipment [Crispi et al., 1972, Wilson et al., 1972]. The current study assumes that the welding tip has been optimally located and the transducer horn has been optimally designed to produce the strongest bond.

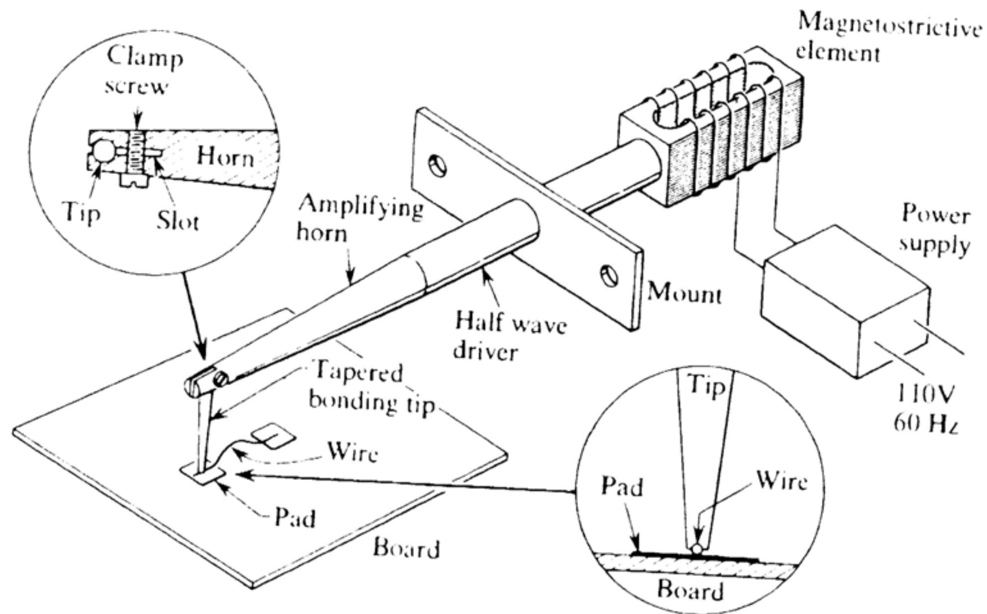

Source: Dushkes, S. Z., "A design Study of Ultrasonic Bonding Tips", IBM J. Res. Development, May 1971.

Figure 4-1 Ultrasonic transducer

4.2 Ultrasonic Bonding Mechanism

Several studies were conducted in the late 60's and early 70's to understand the mechanism that produces ultrasonic bonding in metals. The ultrasonic bonding of two metallic surfaces was earlier thought to be a sum of the following processes,

- The localized melting or heating due to friction, elastic hystereses and plastic deformation
- Mechanical interlocking
- Interfacial nascent bonding
- Chemical bonding involving diffusion

The role of heat in ultrasonic bond formation raised several controversies. It was earlier thought that high temperature was necessary for the ultrasonic welds; however, it was proved that the heat associated with rubbing was due to non-optimum bonding parameters [Joshi, 1971 and Harman et al., 1972]. A low clamping force would eventually result in interfacial sliding thus causing a rise in temperature. Joshi had observed that the temperature readings during the bonding process were less than 70°C, based on readings from a thermocouple. The absence of heat-affected zones and intermetallic compounds in the study also suggested that there was no significant heating. Also, Harman and Leedy [Harman et al., 1972] had successfully made strong bonds in a atmosphere of liquid nitrogen.

In order to study the relative motion between the tool, wire and substrate, Joshi [Joshi, 1971] used a specifically designed laser interferometer. He found that the amplitude of motion of the tool tip, wire and substrate quickly attain a value and remain constant during the entire bonding process. Hence, his study concluded that there was no relative motion between the wire and the substrate.

Ultrasonic stress waves force dislocations to oscillate with amplitudes comparable to distances between their equilibrium positions when no ultrasonic field is applied. [Langenecker, 1966]. Pronounced plasticity is seen to occur in metals. Large scale forming process and strengthening of materials occur as a result of ultrasonic treatment. The following non-linear effects can be observed in a metal exposed to ultrasonic irradiation,

- Acoustic softening
- Acoustic hardening

The acoustic irradiation reduces the apparent static stress necessary for plastic deformation. Hardening occurs after ultrasonic irradiation. Langenecker had shown the similarity between stress elongation curves in aluminum resulting from ultrasonic irradiation at constant temperature to equivalent elongations arising due to the application of heat (Figure 4-2). In his study, high purity aluminum crystals were exposed to ultrasonic irradiation at 20 kHz at various power levels at 18°C.

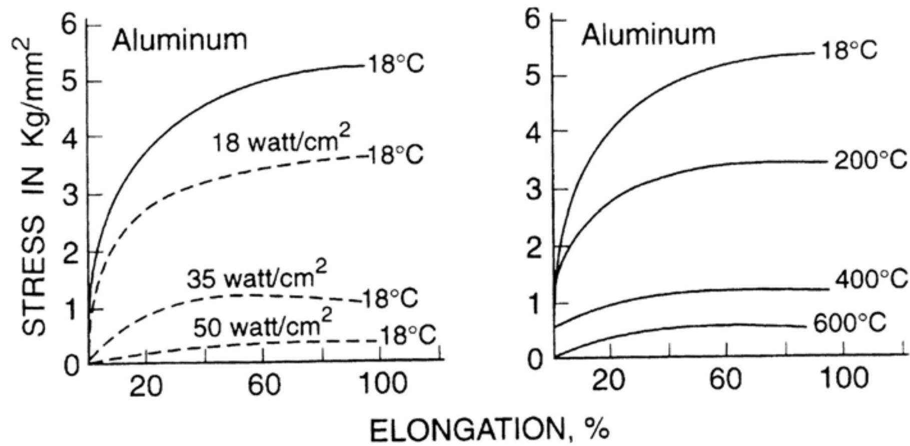

Source: Langenecker, "Effects of Ultrasound on Deformation Characteristics of Metals", IEEE Transactions on Sonics and Ultrasonics

Figure 4-2 Stress vs. elongation for aluminum crystals

This softening mechanism was observed in several other metals like, Cd, Fe, Ti and W. It was concluded that the acoustic softening takes place when the metal is subjected to ultrasonic irradiation.

The stress vs. elongation was essentially equivalent to deformation under a compressive load. It was concluded from the study that either heat or ultrasound would produce equivalent deformation. However, apart from the similarity in displacements,

there are several differences between the processes. The ultrasonic energy density required to produce deformation in aluminum with no applied stress is 10^7 eV/cm^3 times lesser in magnitude in comparison to a sample subjected to thermal energy producing equivalent deformation.

Acoustic energy was assumed to be absorbed at those regions in the metal lattice, which are known to carry out mechanisms of plastic deformation (e.g. grain boundary and dislocations). Ultrasound is presumably propagated through the metal by phonons, a quantized mode of vibration occurring in a rigid crystal lattice. These phonons give up most of their energy to crystallographic defects. In contrast, the thermal energy distributes rather homogenously among all atoms of the crystal including those that do not participate in the plastic deformation. Hence, deformation through plastic deformation by thermal energy is less efficient in comparison with ultrasonic irradiation. It is to be noted that Langenecker's studied only the softening of metals and metal forming when exposed to ultrasonic irradiation and not the ultrasonic bonding or welding process.

Joshi [Joshi, 1971] conducted further studies to develop an understanding on how metal-to-metal ultrasonic bonds were made. He observed that localized deformation occurs on favorably oriented grains on both sides of the interface and joining occurs on certain matching areas. In Al-Al bonds, the interface disappears completely leaving behind a structural pattern that indicates a gross flow of metals. The features of the interface are characterized by lack of work hardening and diffusion. Bonding in dissimilar materials occurs by extensive mechanical interlocking and deformation. The softer material flows around the topography of the harder material. Hence, the ultrasonic

bonding process can be summarized as seizure through atomic attraction, and sometimes by mechanical interlocking once intimate contact is developed due to softening on both sides of the interface. Also, ultrasonic bonding is a process where deformation and recrystallization proceed concomitantly [Joshi, 1971]. The high energy densities during bonding results in strains being annealed continually thus leaving a strain free interface. This theory was also supported by the fact that intense acoustic oscillations caused a large increase in recrystallization kinetics of copper [Hayes et al., 1969]. Evidence of concomitant deformation and recrystallization during bonding process was also supported by studies by Krzanowski [Krzanowski, 1990]. In that study, transmission electron microscopy (TEM) was used to examine ultrasonic bonding of aluminum wire to various metal substrates. The growth process of aluminum crystals due to thermal cycling was later studied by Ohga [Ohga, 1991]. He observed that crystal growth was not found near the bonding points of the aluminum wire suggesting less damage was done during the wire bonding process. However, the reduced cross-section with the constraint would result in the heel section acting like a stress-raiser.

4.3 Bond Formation Patterns

The footprints that remain after the bond is lifted off were studied to better understand the contact mechanism. The lift-off patterns represent the best method of studying the early stages of the bond formation. The wire-to-bond pad micro-welds were formed at points near the perimeter [Harman et al., 1972, Harman 1997, Ramminger et al., 2003, Wu et al., 1995]. The weld formation always begins around the perimeter and as the welding time increases the welded area grows inwards. Krzanowski [Krzanowski,

1990] had reported the presence of surface oxides in the unwelded regions of the bonded interface of the wire, while perfectly welded points were indistinguishable from normal grain boundaries, through X-ray microanalysis in the TEM.

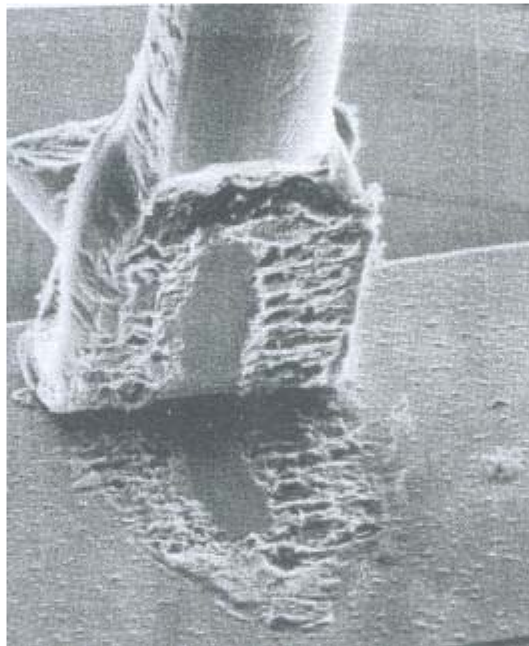

Source: Harman, Wirebonding in Microelectronics, 1997
Figure 4-3 Bond pad lift-off pattern for non-optimized process parameters

Harman [Harman, 1997] had observed the lift-off patterns for a non-optimized set of input parameters. The wires were partially lifted to observe the weld patterns. It is clearly seen through Figure 4-3 that the wires are welded very well near the perimeter while the center is left unwelded. It is very important to note that this is not the failure mechanism observed in the power modules. The illustration has been used primarily to show the unwelded regions on performing a pull test. The failure induced by thermal cycling in the power modules for optimized set of input parameters will be different from what the pull test image in Figure 4-3 shows.

One of the explanations for this perimeter bonding is the fact that the softening effect plays an important role in dispersing the surface oxide film and contaminant from the perimeter. The removal of surface oxides is very essential for a strong bond. In the initial phase of the wirebonding process, the wire is pressed onto the substrate and the surface oxide layer is broken up effectively at the points of high plastic deformation. Little deformation takes place in the center, leaving the surface oxides and eventually leaving this area unwelded. The perimeter welding in well-made microelectronic bonds seem to be related to the bonding machine, tool shape and the bonding schedule [Harman et al., 1977].

4.4 Wire Bond Process Parameters

The wire bonding process depends on many parameters, of which the critical ones are shape of the bonding head, ultrasonic power, bonding force and the bonding time. Heat is an additional factor for ball bonding.

The wire is positioned under the bond foot of the wedge via the hole (Figure 4-4), and the tool comes down on top of the wire with a pre-determined force. Ultrasonic energy is transmitted to the wire through the tool, as soon as contact is established. As explained earlier, the intensity of the ultrasonic power governs the softening of the wires. For a good bond to be created, the tool must be effective in transmitting the ultrasonic energy down through the wire. There are several profiles of the groove edges commonly used for large bonding wires [SPT catalogue, 1996], which include concave, inline groove, “V” groove and Deep “V” groove designs (Figure 4-5). The V-Groove is the more prevalent design in the large bonding wires. Hence, in this thesis the tool profiles

used for simulation would be based upon the V-Groove profiles with the 60° groove angle. The wedge tool chosen for the current study is used for a 381 μm wire diameter. The tool dimensions used in the current study are given in Table 4-1.

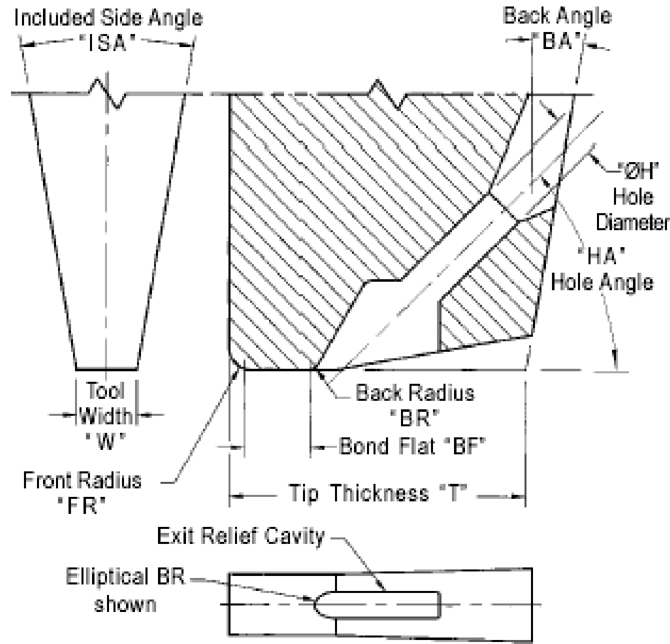

Source: Small Precision tool, Ultrasonic Bonding Wedges, Revised 08-99-6

Figure 4-4 Bond wedge profile

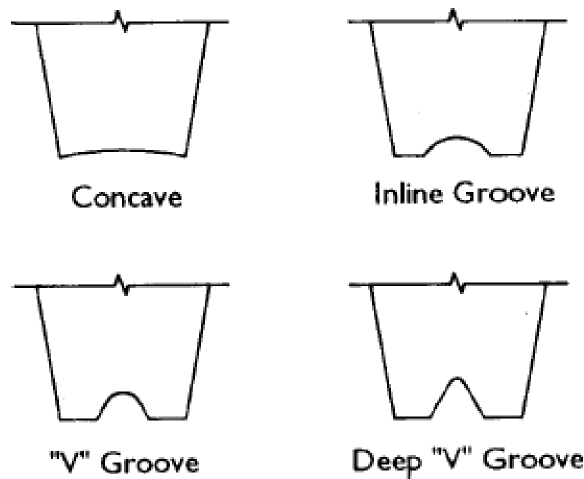

Source: Small Precision tool, Large Wire bonding tools Catalog, Revised 02-96-3

Figure 4-5 Wedge groove profile for large bonding wires

Table 4-1 Tool dimensions

Parameters	Dimensions in μm
Tool Foot Length (FL)	932
Bond Flat (BF)	508
Foot Width	1067
Groove Depth	178
Groove Radius	160
Groove Opening	391

The bond flat is the actual length of the flat base of the bonding tool that comes in contact with the top of the wire. This can give a good indication of the actual bond length during the bonding process.

4.5 Wire Properties when subjected to Ultrasonic Energy

As explained earlier, heat or ultrasound would produce equivalent deformation. It was shown by Langenecker [Langenecker, 1966] that complete yielding of Aluminum occurred at 20 KHz ultrasonics with ~50 W/cm^2 power without any additional stress. For a 381 μm diameter wire the power used for bonding is 10-13 W. Joshi [Joshi, 1971] had assumed a conservative value of 1% to the efficiency of energy transfer between the power supply and the bond interface. Considering the same efficiency in the current study for a 381 μm diameter wire, the intensities of ultrasonics would exceed 50 W/cm^2

(assuming the area of contact to be a product of wire diameter x bond flat). Since it was impractical to simulate the real ultrasonic bonding process considering all the complications explained earlier, heat that would produce an equivalent effect was used instead. For this purpose, the material properties of the wire were determined at 500°C. At this high temperature, the stress elongation behavior of the material would be equivalent to the properties of the wire when exposed to ultrasonic power of 10 W.

Figure 4-6 shows the stress-strain curves of the aluminum wire measured at room and high temperatures. It is observed that at 500°C extreme softening of the metal occurs. Figure 4-7 shows the modulus of the wire at various temperatures. It is observed that until about 200°C the modulus remains almost a constant beyond which it starts to reduce. All these properties were measured using the Rheometrics Solids Analyzer, RSA 2, which has a capability to measure the mechanical properties in the temperature range -150°C to 600°C.

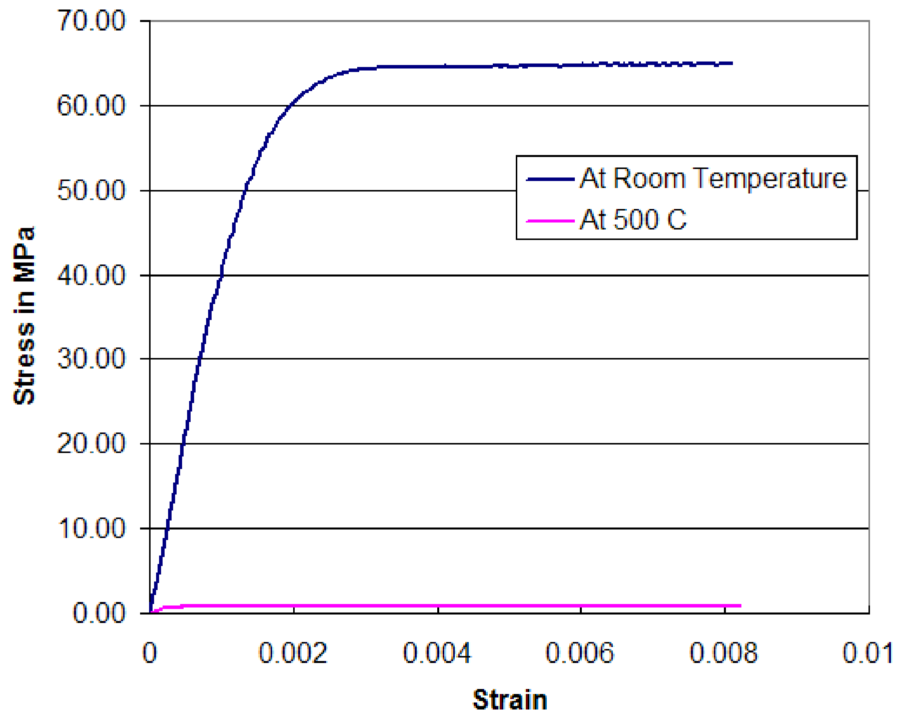

Figure 4-6 Stress-strain curves at room and high temperature

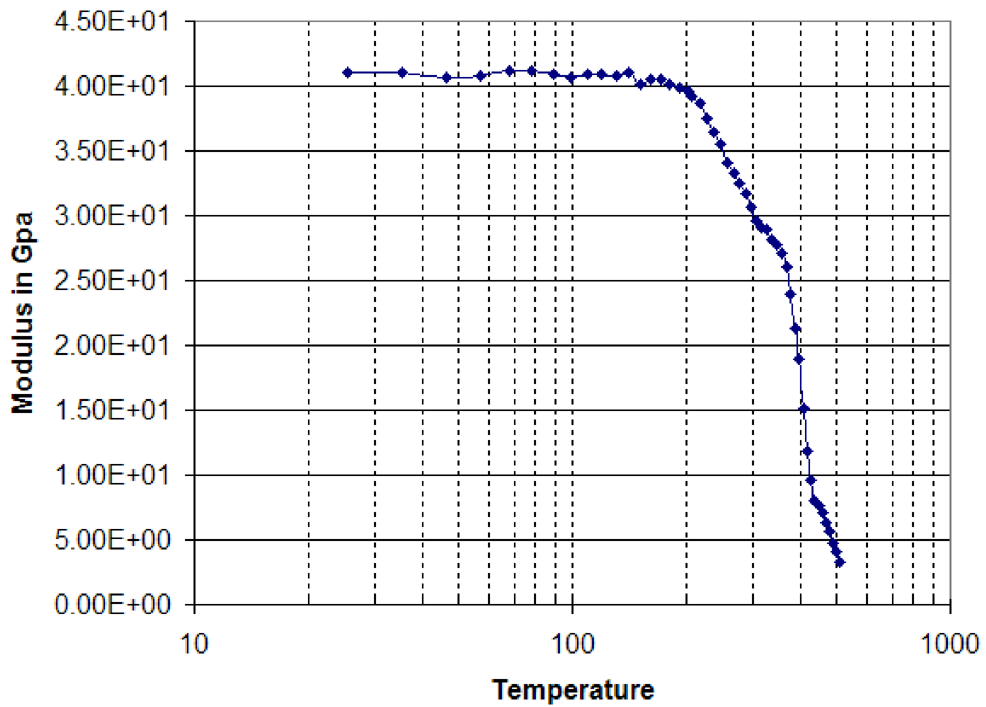

Figure 4-7 Modulus at various temperatures

4.6 Effect of Tool Shape on Wedge Bonding

The internal groove angle for a 381 μm diameter wire, considered in the study, is 60°. In order to provide an explanation for the perimeter bonding, different non-standard groove angles of 50°, 70° and 90° were also chosen for the analysis. A finite element simulation of the bonding process was done using contact elements in ANSYS. The model consists of two dimensional plane strain quadrilateral elements. The tool profile on the two dimensional cross-section corresponds to the standards provided in the SPT catalogue for large bonding wires and have been shown in Table 4-1. Figure 4-8 shows the half section of the wire (considering symmetry) with the tool profile, which has a 60° groove angle and 160 μm groove radius.

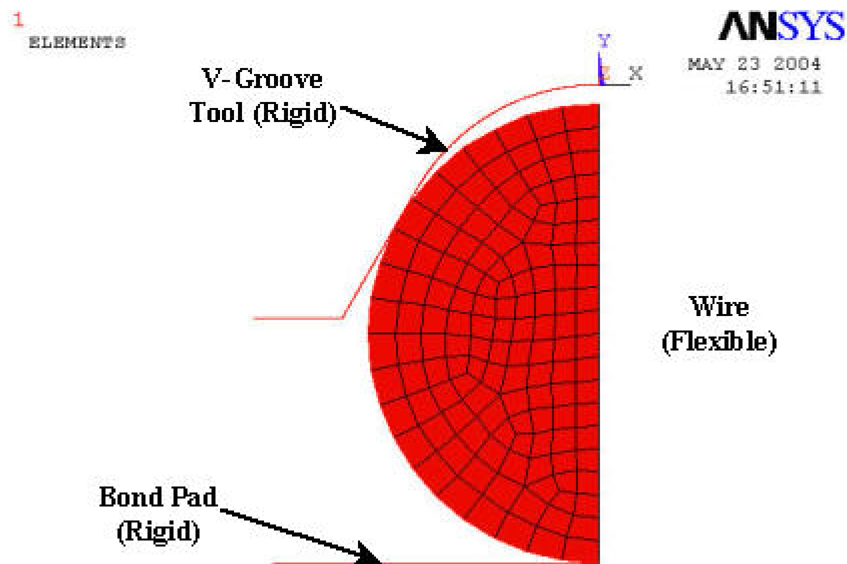

Figure 4-8 Finite element simulation of contact between wire and pad

The softened material properties of aluminum, corresponding to properties at 500°C, were used for the analysis. Contact elements were used for the analysis. Based on

the theory explained earlier, the following types of contact mechanics was used for the simulation,

- Standard contact was assumed between the tool and wire, which permits the separation of the tool from the wire when the tool is lifted.
- Bonded contact was assumed between the wire and the pad. Once contact was established between the wire and the pad, they would remain intact.

Considering the softened property of the wire when subjected to ultrasonic irradiation, the wire was always assumed the flexible surface. The pad and the tool (made of Tungsten Carbide) were rigid when compared to the softened wire (Figure 4-8). The entire cross-section of the tool was not modeled due to limitations in the number of nodes and also due to the very high computational time involved to run even a two dimensional analysis. The analysis was simplified by assuming the tool and the pad as rigid lines. This restricts the applicability of bond force on the line elements (contact elements). Instead, the bond force is applied in terms of a vertical displacement of the tool in the downward direction. A deformation of 0.05 mm was given to the tool in the downward direction for studying the effect of the groove angle on the resultant bond formation.

Figure 4-9 and Figure 4-10 show the displacement contours and the von Mises stress distribution at the end of the load cycle. The greatest plastic deformation does not occur in bottom of the wire on the line of symmetry. There is significant amount of deformation occurring at the edges of the wire. Marked plastic deformation also occurs in these regions of the contact surface. This region of maximum plastic deformation produces the best weld between the wire and the metallization. For the 60° groove angle tool, shown in Figure 4-11, maximum plastic deformation occurs in a ring at the

perimeter of the contact surface with a width of approximately 0.3 times the wire radius. However, this is largely dependent on the input power, which defines the softened wire properties, and also the bond force. The oxide film in these regions breaks down by the interfacial deformation resulting in bonding the surfaces at the periphery. This incidentally happens to be the same location where microwelds were observed by various researchers [Harman et al. 1997, Takahashi et al., 1996]. The bonding at the periphery is observed in all the tool designs of 50°, 70° and 90°, shown in Figure 4-11, Figure 4-12 and Figure 4-13 respectively. However, the industry preferred standards happen to be the 60° groove angle. This could be largely due to the higher contact area experiencing maximum plastic deformation, which is essential to remove the surface oxides, when compared to the other designs.

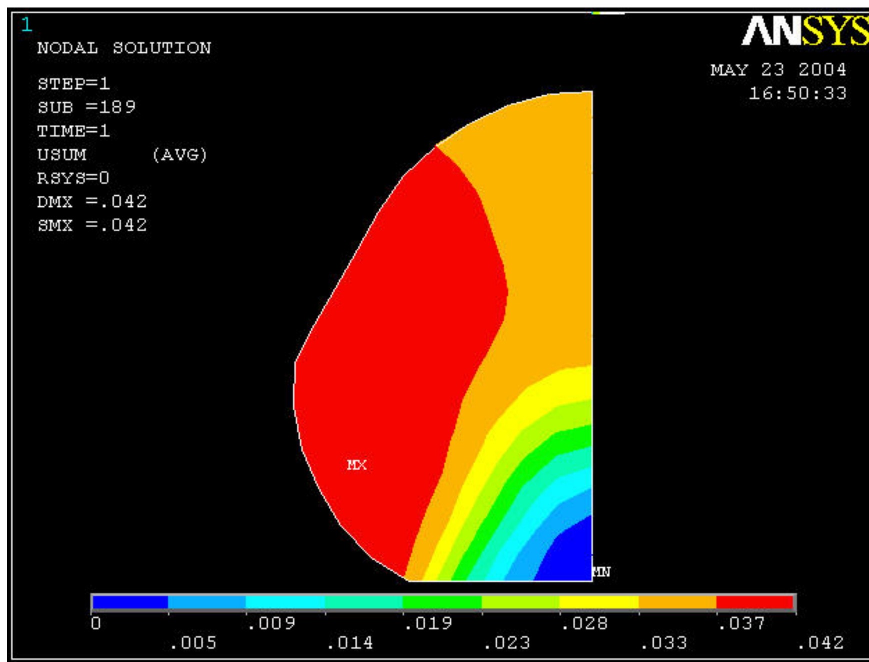

Figure 4-9 Displacement contour for the 60 V-groove tool

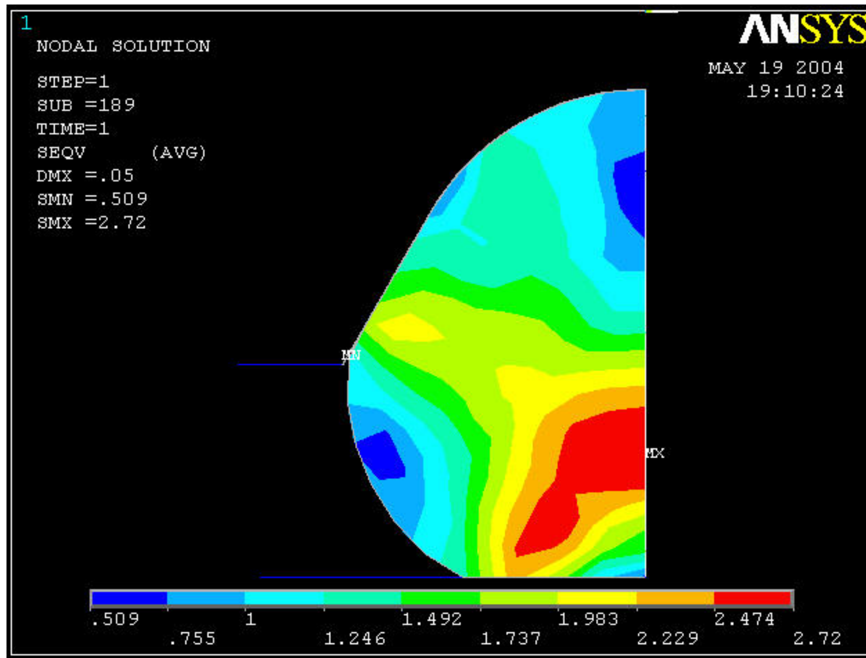

Figure 4-10 60° groove angle

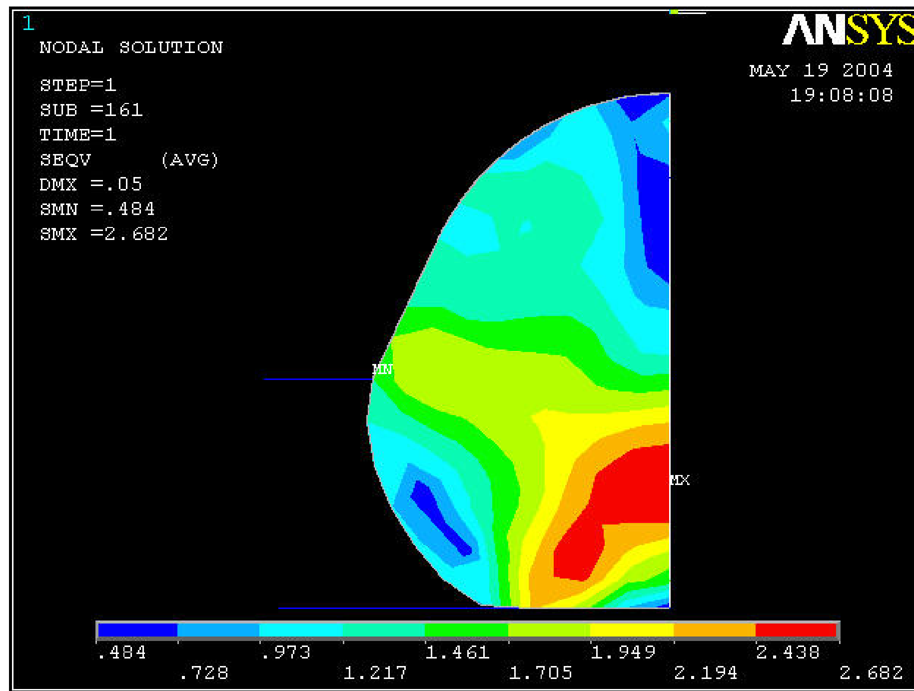

Figure 4-11 50° groove Angle

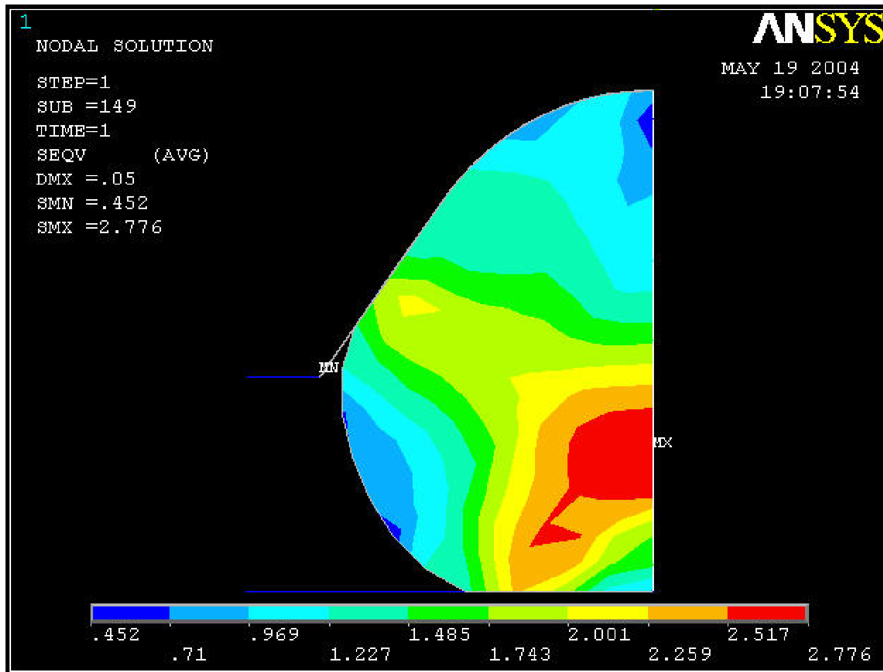

Figure 4-12 70° Groove angle

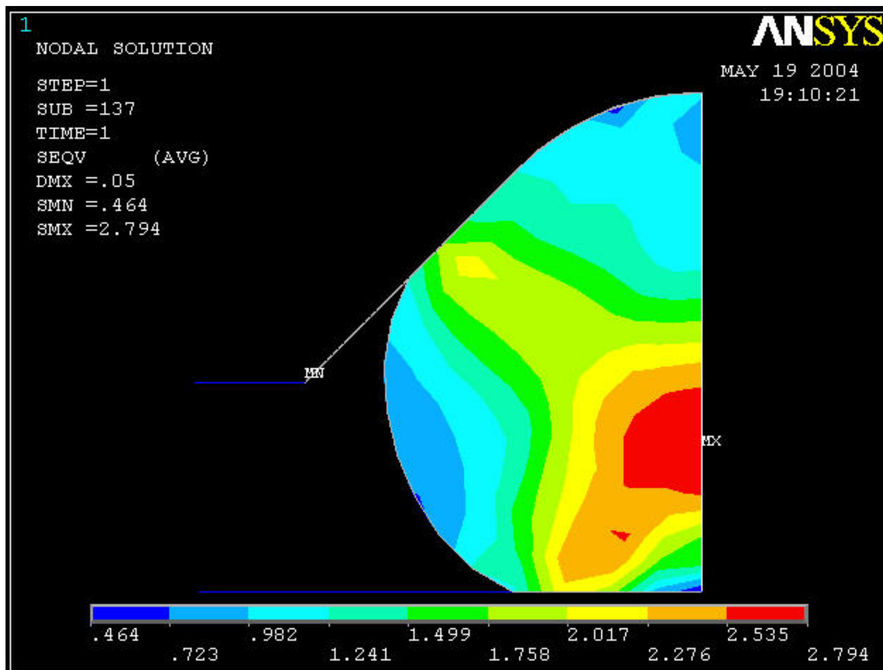

Figure 4-13 90° Groove angle

4.7 Wire Deformation and its Effect on Flexural Stresses

Current bonding processes deform the wire 1.3X to 2.0X times the original diameter [SPT Catalogue, 1999]. The amount of deformation is also governed by the tool design. The latest tool designs permit an even smaller deformation. Small deformations are preferable for the fine pitch applications. Unlike the ball bonding process, in a wedge-bonding process, the bond width can be smaller than 1.2 times the wire diameter since there is no need for a free air ball. However, the lengths of the bonds are longer as shown in Figure 4-14. Takahashi [Takahashi et al., 1996] had reported that a deformation in width of 1.6 to 2.0 times the wire diameter results in a strong bond.

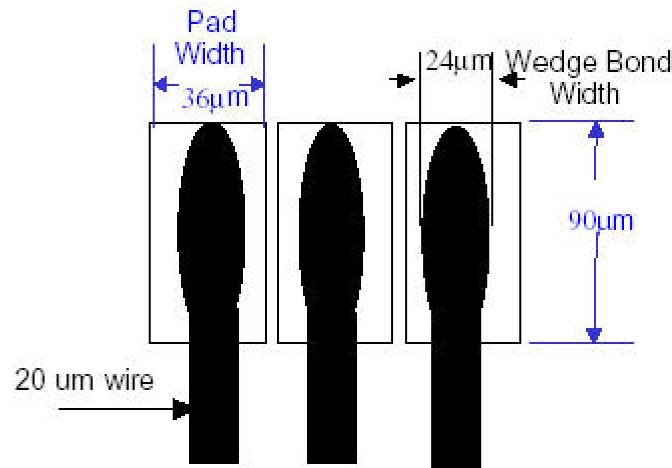

Figure 4-14 Wedge bonding for fine pitch applications

The deformation during bonding was determined for a set of wires that were used in the power module shown in Figure 2-1. The wires were encapsulated in epoxy resin and then polished to the desired location. Figure 4-15 and Figure 4-16 show the front and top cross-sectional views of the wire. The figures also reveal the thin lining of bond pad

along with the copper lead-frame. The cross-sectional images revealed that all the wires were deformed to approximately 1.2 times the wire diameter.

It is important to note that the deformation of the wire is a qualitative measure for measuring the contact area between the bond pad and the wire. Also, this contact area affects the strength of the bond. A low contact area, or reduced deformation would result in a weak bond. Such a wire is expected to fail by wire lift-off. An increase in the contact area would alleviate this issue. However, the increased deformation might cause more damage to the heel resulting a wire flexural type of failure. In this thesis, the effect of deformation on the flexural stresses would be investigated.

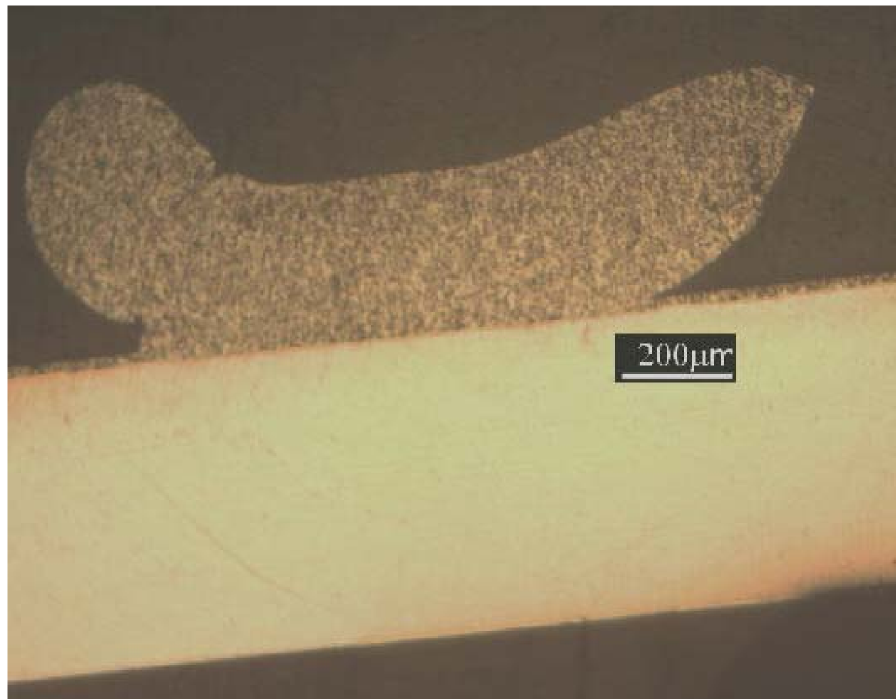

Figure 4-15 Front view of the cross-sectioned wire

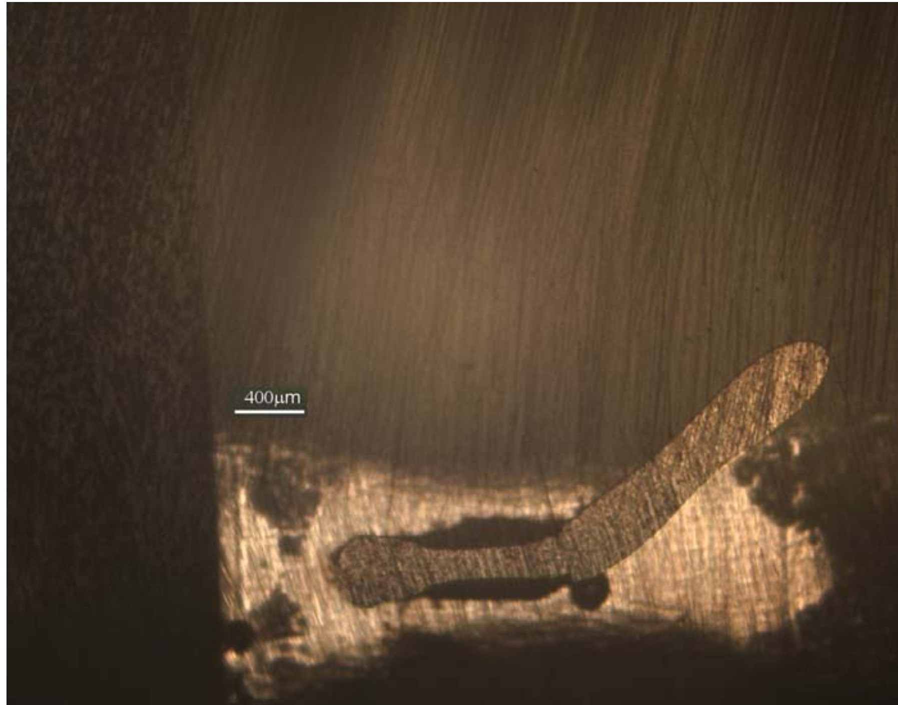

Figure 4-16 Top view of the cross-sectioned wire

It has been proved that the critical region when considering flexural stresses is always the heel of the wire. The top surface of the wire is expected to be in compression while the bottom surface is in tension. From fracture mechanics perspective, it is always the tensile stresses that are of more concern. Also, the heel in the bottom of the wire is more stressed since it lies next to a highly constrained section of the wire. To fully understand the effects of bond deformation on life a three-dimensional approach should be used to model the flexural stresses.

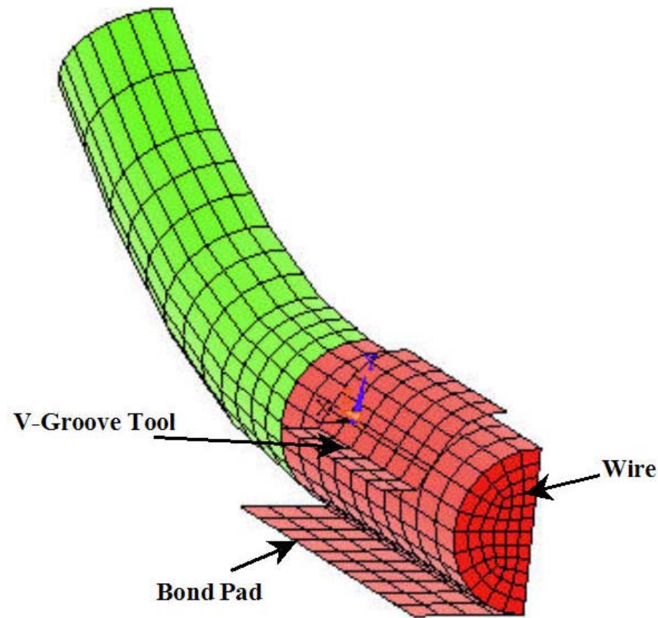

Figure 4-17 3D Finite element model of the tool-wire-pad

Figure 4-17 shows part of the model of the wire-tool-pad surfaces with the finite element mesh. The surface-to-surface contact feature in ANSYS has been used to simulate the contact between the various surfaces. As stated earlier for the two-dimensional case, the wire has been assumed the flexible surface while the pad and tool are the rigid surfaces. The analysis has been performed with 20 noded Isoparametric brick elements. To achieve the same sort of accuracy with 8-noded hexahedral elements a much-refined mesh would be necessary. The model had as many as 8965 elements with 42167 nodes, which would result in overall 126501 degrees of freedom. The number of elements have been carefully chosen after several convergence tests.

The V-Groove tool with 60° groove angle mentioned in section 4.4 was chosen for the contact analysis. In order to study the effect of the wire deformation on the flexural stresses, the bond force/tool displacement has to be changed. Analysis has been performed with the following tool displacements, 0.05 mm, 0.08mm, 0.10 mm, 0.13 mm and 0.15 mm. In each one of the cases, the maximum amount of wire deformation is observed. Hereafter the notation, B, would be used to denote the wire deformation while B/2r would denote the wire deformation per unit wire diameter (2r is the wire diameter).

The initial load step consisted of application of the tool displacement to cause the wire deformation. In the second load step, the tool is brought to its initial position thus allowing the wire to partially retain its original shape. However, considering the plastic deformation there would be significant permanent deformation on the wire. In the above-mentioned load steps, the softened wire properties are provided. The last load step consisted of application of the thermal cycling load. This would induce high flexural stresses on the heel of the wire.

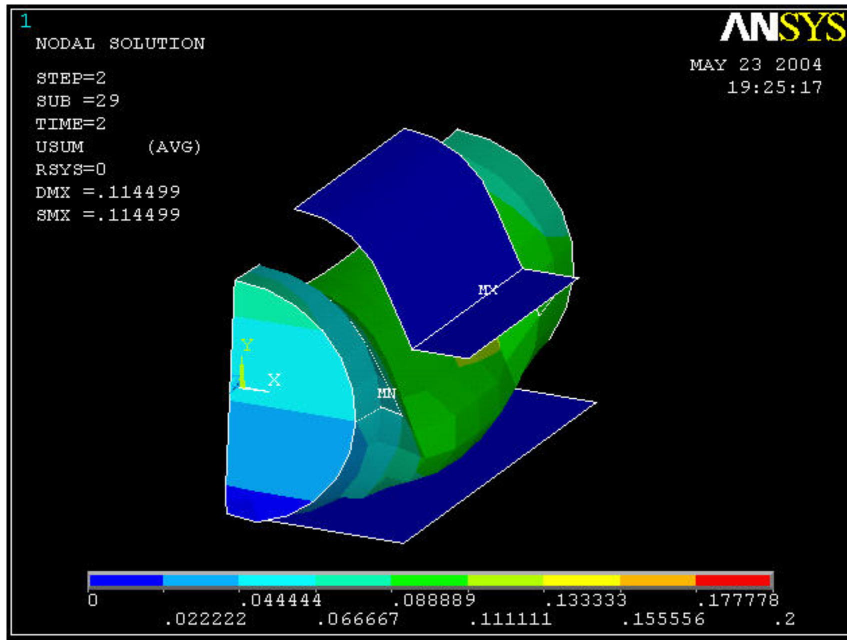

(a) Tool Displacement 0.13 mm

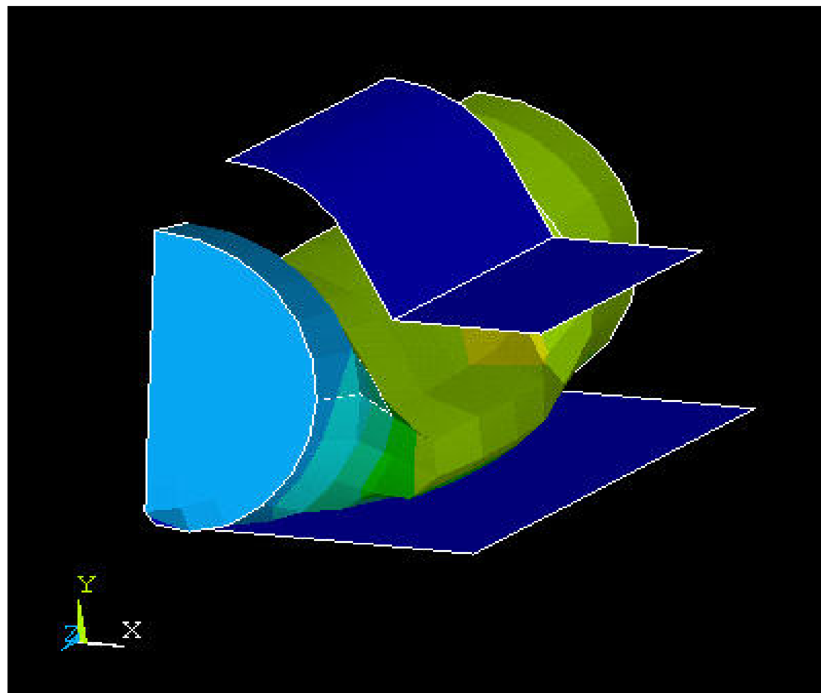

(b) Tool Displacement 0.15 mm

Figure 4-18 Deformed wire profile

Figure 4-18 (a) and (b) show the deformed wire profiles for a 0.13 mm and 0.15 mm displacement of the tool. The bending stresses have been plotted for a 0.15 mm tool displacement in Figure 4-19. Figure 4-20 shows a blowup of the wire profile near the upper bond pad. It is clearly seen from the figures that maximum bending stresses occur in the heel of the wire near the upper bond pad. As one would expect, the tensile bending stresses are higher than the compressive bending stresses due to the proximity of the lower section of the heel to the location of the constraints. This location in the heel of the wire is approximately 0.15 times the wire diameter, from the point of constraint. The bending stresses are maximum tensile at the lower section of the wire near the heel. The magnitude switches to compressive near the loop height and then switches back to tensile near the lower heel of the wire at the other end. A very similar trend is seen for the other tool displacements of 0.05, 0.08, 0.10, 0.13 and 0.15 mm. However, the results have been plotted only for the tool displacement of 0.15 mm.

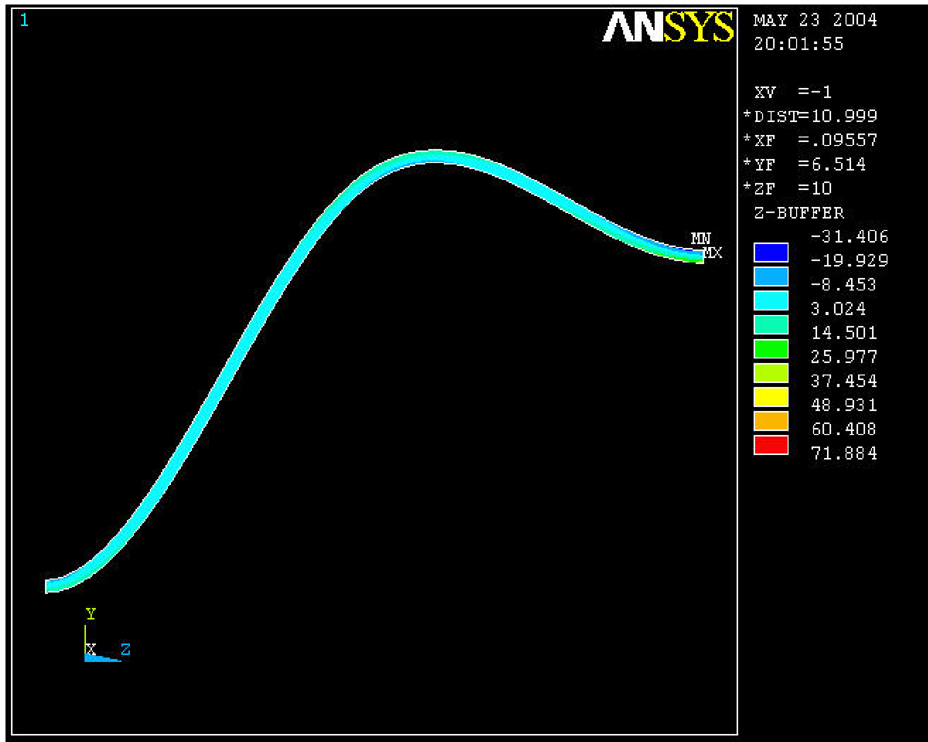

Figure 4-19 Bending stress distribution in the wire

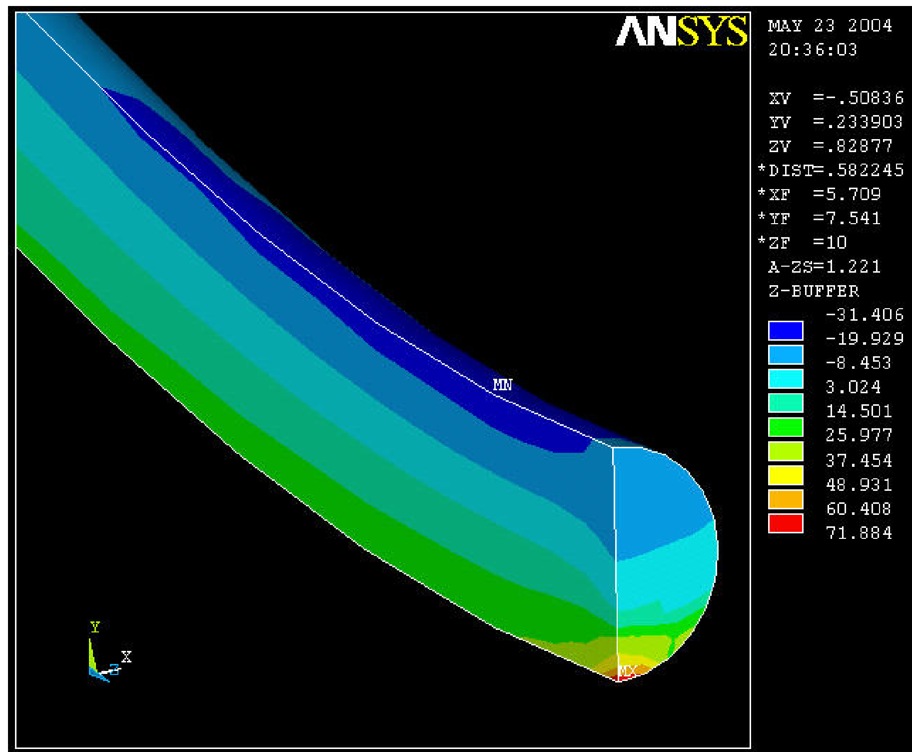

Figure 4-20 Bending stresses near the upper bond pad

Figure 4-21 shows the various amounts of wire deformation, B, for different tool displacements. It is observed that as the tool advances the wire deformation increases. The ratio of wire deformation to wire diameter, B/2r, for various tool displacements have been plotted in Figure 4-22. It is observed through the figure that B/2r increases from 1.03 to 1.31 when the vertical displacement of the tool increases from 0.05 to 0.15 mm. The normal stresses corresponding to these deformations are plotted in Figure 4-23.

From the figure, it is clearly seen that as the deformation increases it puts more flexural stresses on the wire when it is subjected to thermal cycling. Hence, it is advantageous to have as little wire deformation as possible. However, this may lead to a different sort of failure mechanism, the wire lift-off, in such wires. With wire deformations of 1.2 times the wire diameter, wire flexure was always the dominant failure mechanism.

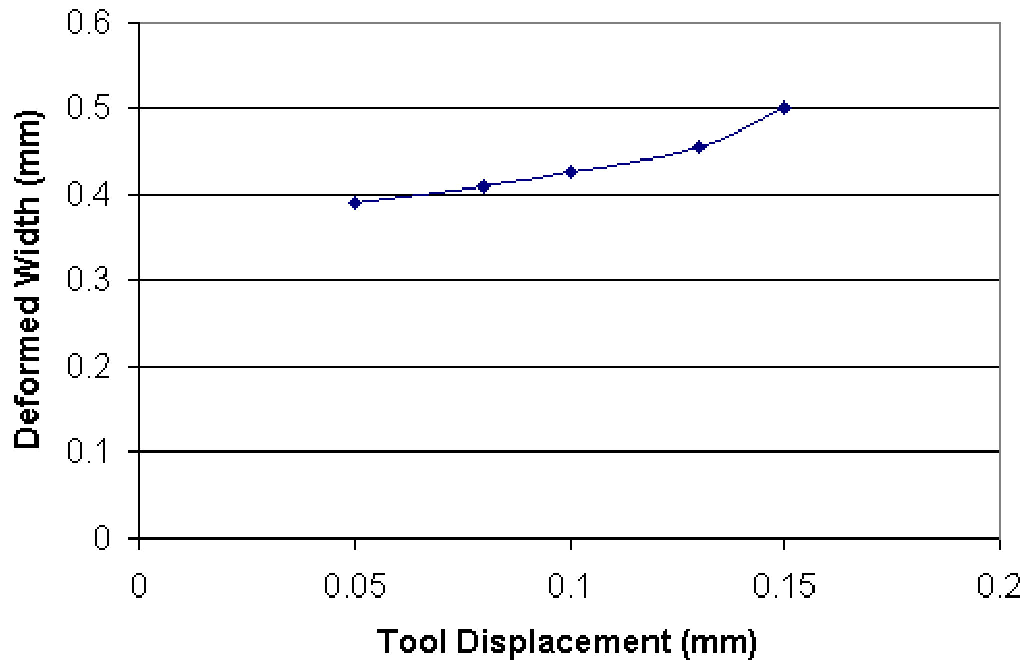

Figure 4-21 Wire deformation for various tool displacements

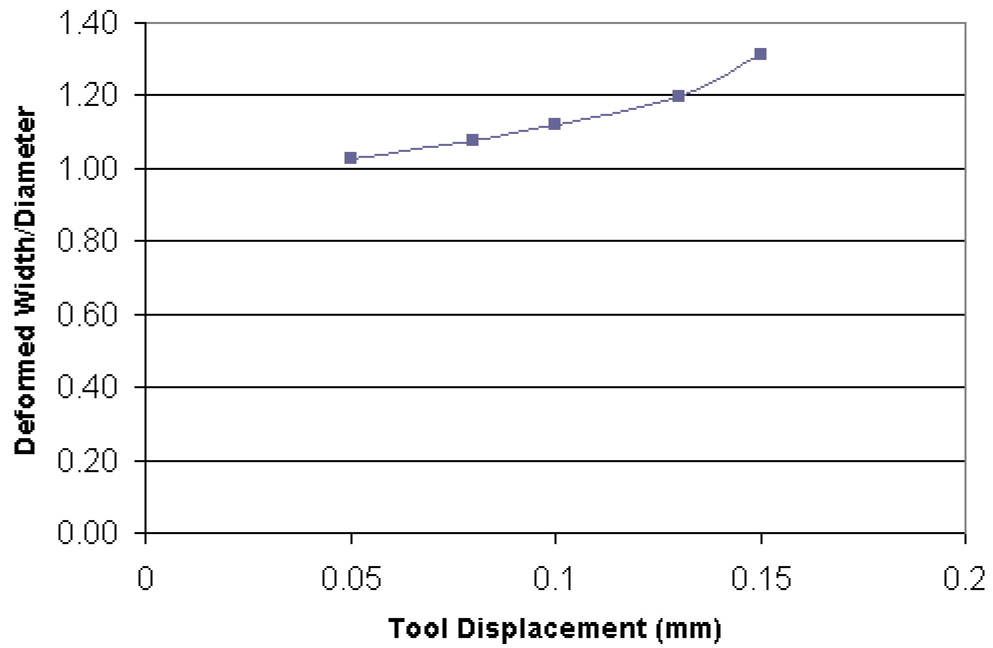

Figure 4-22 B/2r for various tool displacements

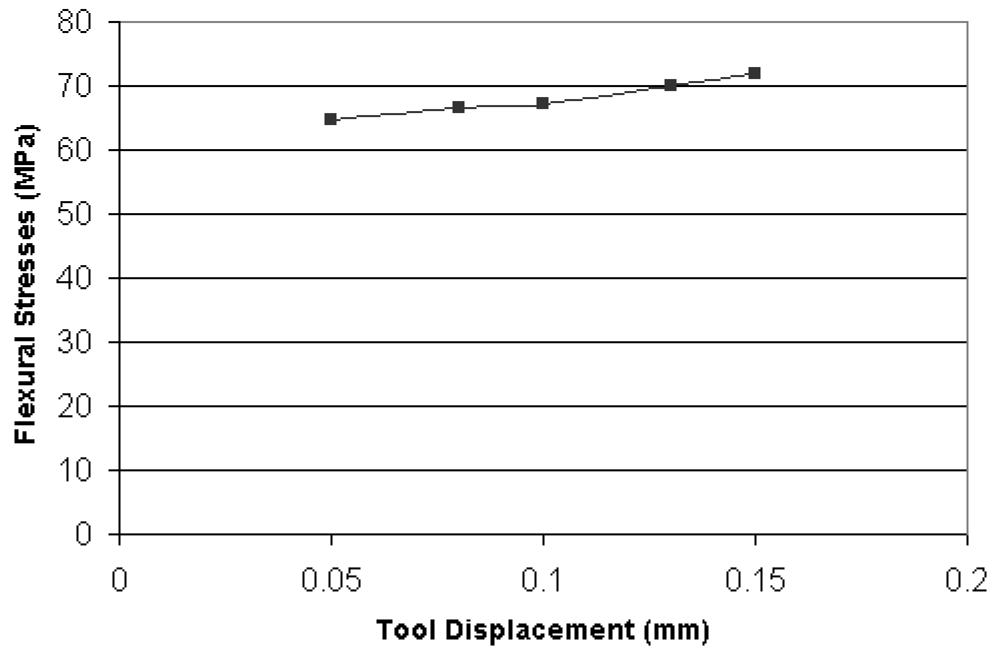

Figure 4-23 Flexural stress for various B/2r

4.8 Effect of Wire Deformation on the Wire Fatigue Model

As mentioned earlier in Section 3.6, wire thinning near the heel is not captured by the physics of failure based model. However, its effect could be introduced in terms of a stress concentration parameter, K_s, which accounts for the wire thinning due to the ultrasonic bonding process.

In Figure 4-16 it was shown that the wires used in the power module had a deformation of 1.2 times the wire diameter. This corresponds to a 0.13 mm of tool displacement in the downward direction, shown in Figure 4-22. The pure bending stresses (does not account for the wire thinning effect) on the upper section of the wire from finite element, is compressive with a magnitude of 31 MPa. However, on the lower section of the wire near the heel, the stresses are much higher (i.e. 70 MPa for the 0.13 mm

displaced tool), as shown in Figure 4-23. The reduced cross-section near the heel increases the stresses by a factor of 2.26 (i.e. $K_s = 70/31 \approx 2.26$). The first order physics of failure based model derived in Chapter 2 predicts a bending stress variation between –35.14 MPa on top fibers to 35.14 MPa on the bottom fibers. The stress concentration parameter, K_s, of magnitude 2.26 is included in the damage prediction model given in Eq. 2-32.

The modified damage model is used to revalidate the thermal cycling results explained in Section 3.3. The results have been shown in Figure 4-24. With the inclusion of the effect of wire thinning near the heel, it is observed that the modified model predicts much closer to what is observed through the experiments.

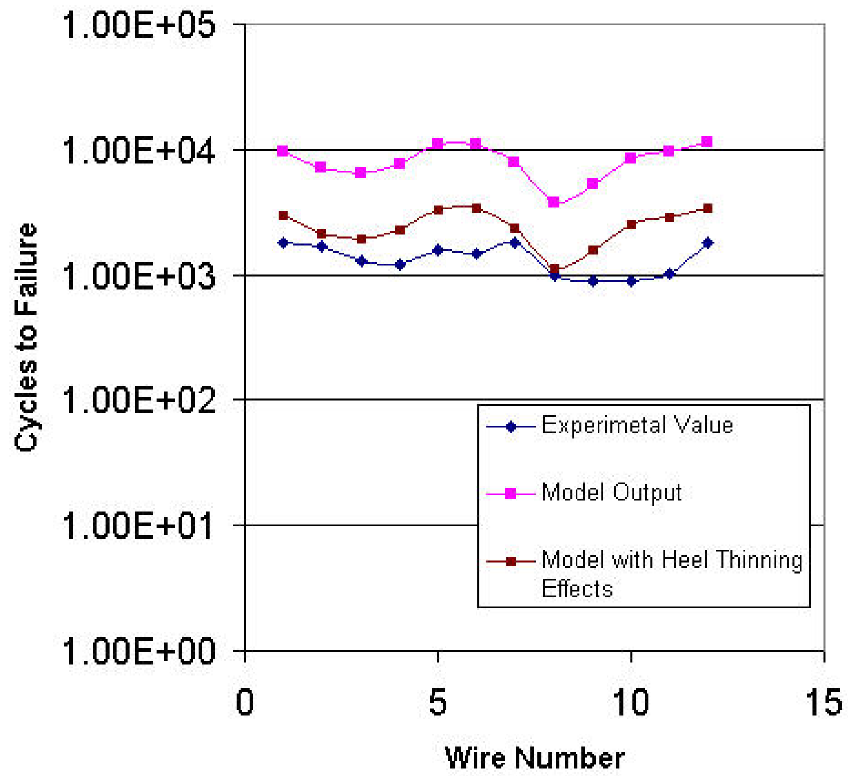

Figure 4-24 Thermal cycling results revalidated

Chapter 5: Effect of Wire Twisting

A traditional wedge bonder, unlike the ball bonder, is unidirectional i.e. the bond pads are placed in the same direction as the wire [Qin, 2001]. However, there are some applications where it is desired to have non-aligned bond pads. The circuit pattern on the direct bonded copper substrate, shown in Figure 5-1, prevents the wedge bonder from making unidirectional bonds. Such twisting can place additional stresses on the wire, thus causing it to fail prematurely. Hence, it was considered important to focus on the aspects of wire twisting and its effect on the bending stresses. The scope of the current research is specific to wires that are bonded to pads, aligned parallel to one another, but with a width offset, W. The width offset prevents the wires from being aligned parallel to the bond pad thus introducing twisting effects.

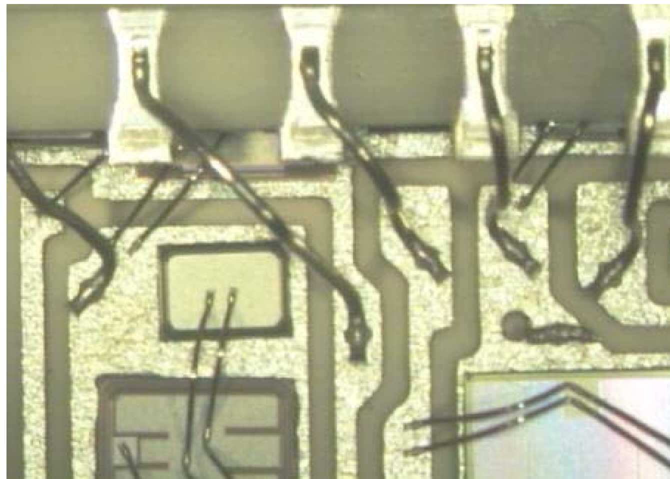

Figure 5-1 Twisted wires

5.1 Loop Profile

As mentioned throughout the text, one of the most important aspects in the virtual qualification is the determination of the wire geometry. Eq. 2-13 and Eq. 2-14 represent the wire profile in the two-dimensional plane, using two curves (Figure 2-2). In order to account for the effect of the width offset, the wire has to be represented in a three-dimensional co-ordinate system. One of the simplest methods in achieving the three dimensional effects would be to consider a linear variation of the wire on the Z-direction.

$$Z(x) = \frac{Wx}{D} \quad (5\text{-}1)$$

However, by doing so, the wires might be stressed more near the bond edge where there is significant amount of twisting as shown in Figure 5-2.

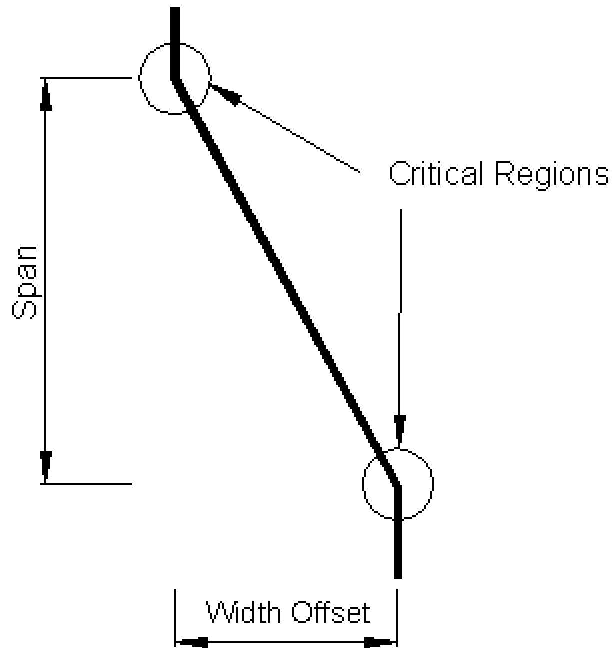

Figure 5-2 Critical regions in a twisted wire

Also, the wire may not prefer to stay in such a highly stressed state after a few fatigue cycles. Hence, it would be more appropriate and accurate, to determine the minimum energy configuration that the wire would prefer to occupy. The energy minimization explained earlier in Section 2.2.3 for a wire represented in a two-dimensional plane, has to be repeated for the wire profile represented in the Euclidean three space, R^3. However, unlike the earlier procedure, a parametric approach is used to represent the three dimensional wire profiles. The following section briefly explains the energy based minimization routine used to determine the three-dimensional wire profiles.

A piecewise parameterized cubic polynomial is used to represent the curves 1 and 2 of the wire profile (Figure 5-3).

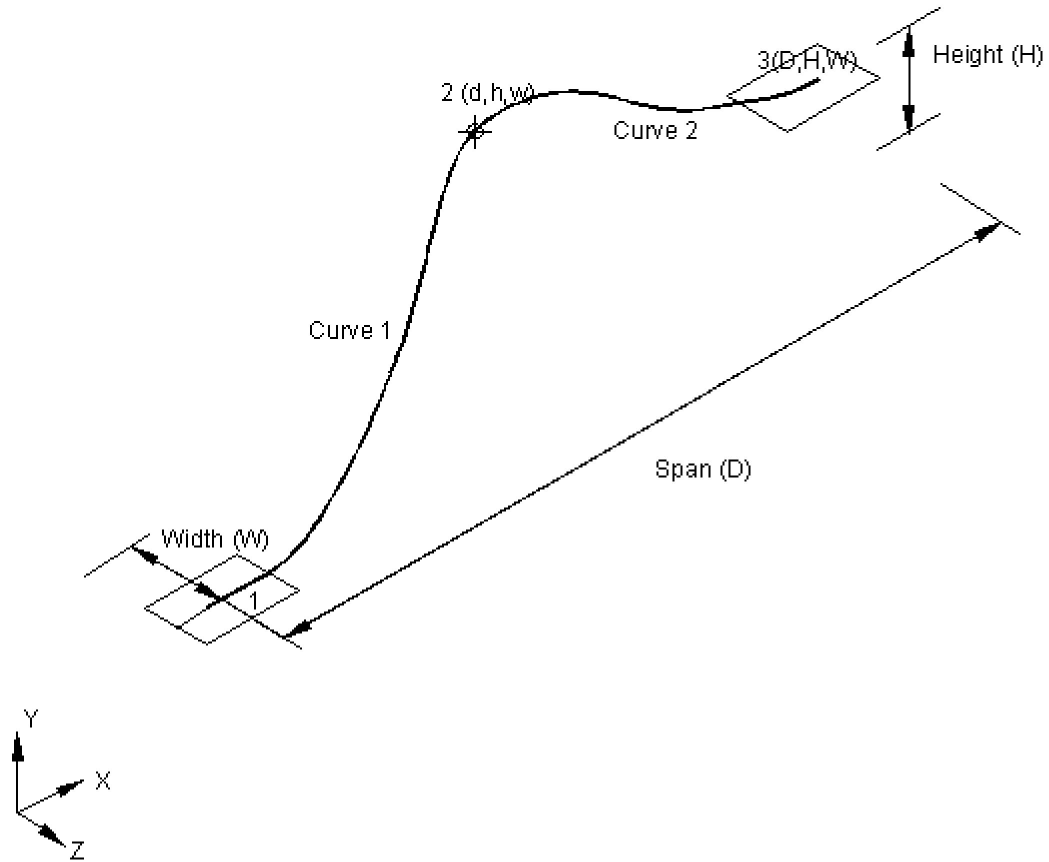

Figure 5-3 Wire profile with parameters

The curves α(u) and β(v) are used to map the parameters u and v to the curves 1 and 2 respectively shown in Figure 5-3. Let $\alpha,\beta: I \rightarrow R^3$ be differentiable curves parameterized by u and v respectively such that,

$$\alpha(u) = (X(u), Y(u), Z(u)) \qquad 5\text{-}2$$

$$\beta(v) = (X(v), Y(v), Z(v)) \qquad 5\text{-}3$$

X(u), Y(u), Z(u), X(v), Y(v) and Z(v) are all cubic polynomials of the form,

$$X(u)=A_0 + A_1u + A_2u^2 + A_3u^3 \qquad 5\text{-}4$$

$$Y(u)=B_0 + B_1u + B_2u^2 + B_3u^3$$

$$Z(u)=C_0 + C_1u + C_2u^2 + C_3u^3$$

where, A_i's, B_i's and C_i's are the coefficients of the cubic polynomial. Also, the wires should satisfy the length constraint. Therefore, any suitable wire geometry that is obtained should satisfy these admissibility conditions i.e. the boundary conditions and the length constraint. The bond point locations are given by points, 1(0, 0, 0) and 3(D, H, W). Point 2 is chosen to be arbitrary with co-ordinates (d, h, w). On imposing the boundary conditions a C^1 continuous curve representing the wire profile is obtained. A C^2 continuity is enforced by equating the slopes of curves 1 and 2 at point 2 (Figure 5-3). The coefficients are determined based on the boundary conditions, location and slopes of the curve at the bond pad. As mentioned earlier, the bond pads are aligned parallel to one another, but with a width offset. The zero slopes at the bond pads, i.e. $\frac{dY}{dX}, \frac{dZ}{dX} = 0$, are enforced by making Y_u (or dY/du) and Z_u (or dZ/du) zero while X_u (or dX/du) remains arbitrary. The arbitrary non-zero value is chosen to be a variable q. On application of the boundary conditions to Eq. 2-6, Eq. 2-7 and Eq. 5-4, the coefficients A_i's, B_i's and C_i's of the cubic polynomials are determined in terms of the unknown parameters d, h, w and q as,

$$\alpha(u) = \begin{Bmatrix} qu + (3d - \frac{3D}{4} - \frac{3q}{2})u^2 + (\frac{3D}{4} + \frac{q}{2} - 2d)u^3 \\ (3h - \frac{3H}{4})u^2 + (\frac{3H}{4} - 2h)u^3 \\ (3w - \frac{3W}{4})u^2 + (\frac{3W}{4} - 2w)u^3 \end{Bmatrix} \quad \text{5-5}$$

$$\beta(v) = \begin{Bmatrix} d + (\frac{3D}{4} - \frac{q}{2})v + (\frac{3D}{2} - 3d)v^2 + (2d - \frac{5D}{4} + \frac{q}{2})v^3 \\ h + \frac{3H}{4}v + (\frac{3H}{2} - 3h)v^2 + (2h - \frac{5H}{4})v^3 \\ w + \frac{3W}{4}v + (\frac{3W}{2} - 3w)v^2 + (2w - \frac{5W}{4})v^3 \end{Bmatrix} \quad \text{5-6}$$

For a regular parameterized curve, the curvatures $\kappa(u)$ and $\kappa(v)$ are given by,

$$\kappa(u) = \frac{\left|\alpha(u)' \wedge \alpha(u)''\right|}{\left|\alpha(u)'\right|^3} \qquad \kappa(v) = \frac{\left|\beta(v)' \wedge \beta(v)''\right|}{\left|\beta(v)'\right|^3} \quad \text{5-7}$$

Simplification of the above equations (Eq. 5-5, Eq. 5-6 and Eq. 5-7) leads to the solution for the curvatures $\kappa(u)$ and $\kappa(v)$. The detailed derivations have been omitted for the sake of simplicity.

5.1.1 Minimization of Strain Energy of the Cubic Spline

It is clearly evident from Eq. 5-5, Eq. 5-6 and Eq. 5-7 that the curvatures and the geometry are dependent on the unknown parameters d, h, w and q. Hence, an energy based approach, which leads to the minimum potential energy of the wire, is used to determine these unknown coefficients. The potential energy of the wire, represented by the piecewise cubic spline, is given by,

$$\Pi = \frac{EI}{2}\int_0^1 \kappa_1(u)^2 \left|\alpha'(u)\right| du + \frac{EI}{2}\int_0^1 \kappa_2(v)^2 \left|\beta'(v)\right| dv \quad \text{5-8}$$

where, EI is the flexural rigidity of the wire and κ_i's are the curvatures of wires 1 and 2. It is easy to see that a wire would always prefer to start off and terminate as smooth as possible. This can be easily understood with the example of a wire bonded without a height offset. The minimum energy profile would be a straight line passing through the points 1 and 3. Without any constraints provided, the loop height would always be less than or equal to the height offset of the wire. In reality, the wires are bonded with a loop height, which is greater than the bond pad height offset. Hence, the length of the wire is always provided as an input, which is introduced into the energy equation as an additional constraint equation. The lengths of the curves 1 and 2 respectively are given by L_1 and L_2 (=$L-L_1$). Other than the admissibility conditions, the dependent variables should also satisfy the constraint equation

$$G = L - (L_1 + L_2) = L - \left(\int_0^1 \left|\alpha'(u)\right| du + \int_d^1 \left|\beta'(v)\right| dv \right) = 0 \quad \text{5-9}$$

G = 0 is enforced through a Lagrange parameter λ. Therefore the new function to be minimized is Q where,

$$Q = \Pi + \lambda G \quad \text{5-10}$$

Q is minimized by seeking its stationary value,

$$\delta Q = 0 \quad \text{5-11}$$

$$\frac{\delta Q}{\delta d} = 0 \qquad \frac{\delta Q}{\delta h} = 0 \qquad \frac{\delta Q}{\delta w} = 0 \qquad \frac{\delta Q}{\delta q} = 0 \qquad \frac{\delta Q}{\delta \lambda} = 0 \qquad 5\text{-}12$$

The above set of non-linear equations are solved iteratively using the Levenberg-Marquardt algorithm to provide the location of the second point (d, h, w) which seeks to minimize the potential energy and also satisfies the length constraint. (Note: Alternatively, the energy minimization could also be solved using the optimization toolbox in Matlab). Substitution of d, h, w and q into Eq. 5-5 and Eq. 5-6 provides the wire geometry.

Considering the vast number of possibilities of locating the reference point 2, on a three-dimensional space, it is very essential to assign the proper upper and lower bounds for each one of the parameters. The program always tries to locate the point 2(d, h, w) such that the strain energy is minimum. Figure 5-4 represents one of the wire profiles determined for a span of 20 mm and width offset of 2 mm. Even though the curve is smooth, the program has located the point 2 outside the bounds (0, W). The reason for such a behavior is presence of several local minima. However, it is the objective of the program to determine the global minima. Enforcing the limits 0 to W for point 2 might still not resolve the problem of preventing the curve entering the –Z axis. However, it can be noted that the slope has to be positive in the interval ($0<x<D$), i.e. $\frac{dZ}{dX} > 0$.

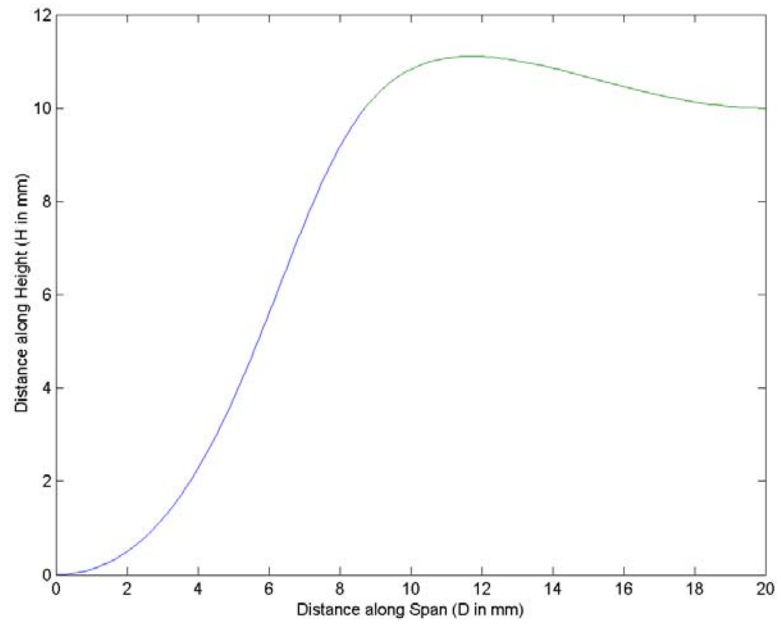

(a)

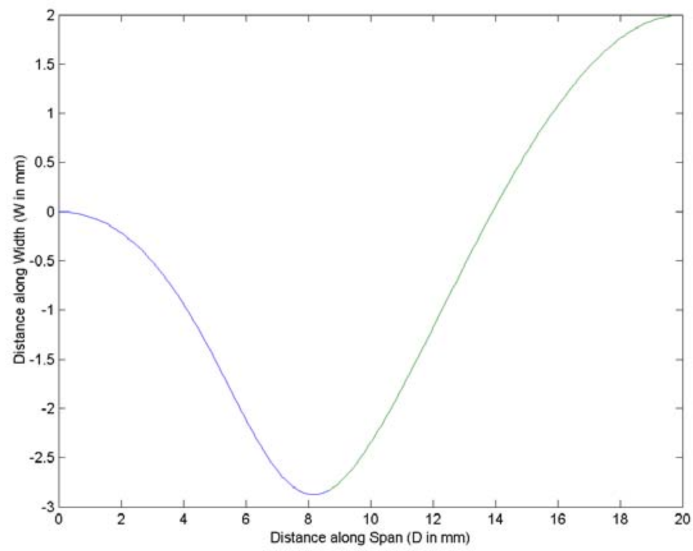

(b)

Figure 5-4 Wire profile for D=20, H=10 and W=2

$$\frac{dZ}{dX}=\frac{(6w-\frac{3W}{2})u+(\frac{9W}{4}-6w)u^{2}}{q+(6d-\frac{3D}{2}-3q)u+(\frac{9D}{4}+\frac{3q}{2}-6d)u^{2}} \qquad \text{5-13}$$

At u=0 the slope would be zero (one of the boundary conditions). But for any other point δu (Limit $u \rightarrow 0$) the slope should be positive.

$$\frac{dZ}{dX}=\frac{(6w-\frac{3W}{2})\delta u+(\frac{9W}{4}-6w)\delta u^{2}}{q+(6d-\frac{3D}{2}-3q)\delta u+(\frac{9D}{4}+\frac{3q}{2}-6d)\delta u^{2}}>0 \qquad \text{5-14}$$

Omitting the small terms δu^2 and using the fact that $q \gg \delta u$, results in the lower bound of w near the first bond pad. This procedure is repeated near the second bond pad (at v=1) to determine the upper bound for w. The simplification of the equations lead to the upper and lower bounds for the variable w as,

$$\frac{W}{4}<w<\frac{3W}{4} \qquad \text{5-15}$$

5.2 Case Study

A case study, based on finite element analysis, was performed to study the effect of wire twisting. Considering the vast number of parameters that could significantly affect the reliability of the wire/wirebonds, it is important to be able to isolate the effect of wire twist. A wirebond with zero width and height offset was chosen with span 20 mm and length 27 mm. The loop height was determined from the energy minimization

routine, explained earlier. Then a set of wires with width offsets of W=0, 2, 4, 6 and 8 mm were chosen with the same loop heights as the input.

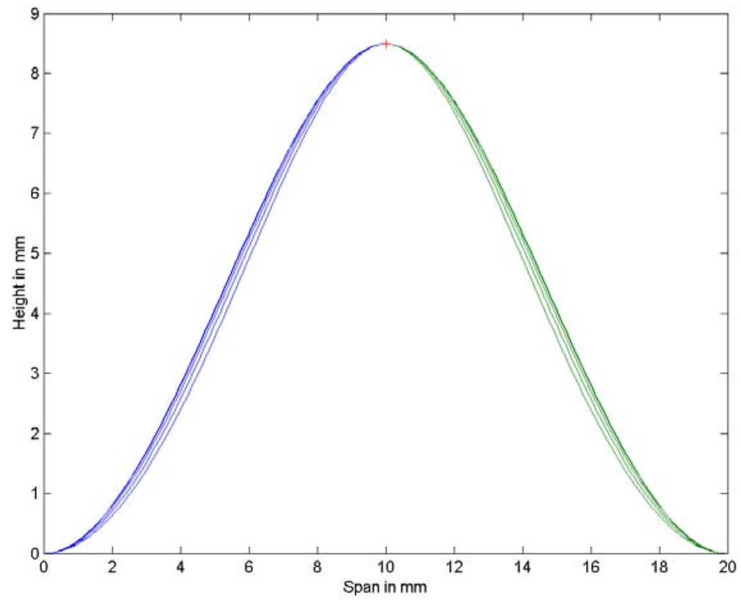

(a) X-Y Plane

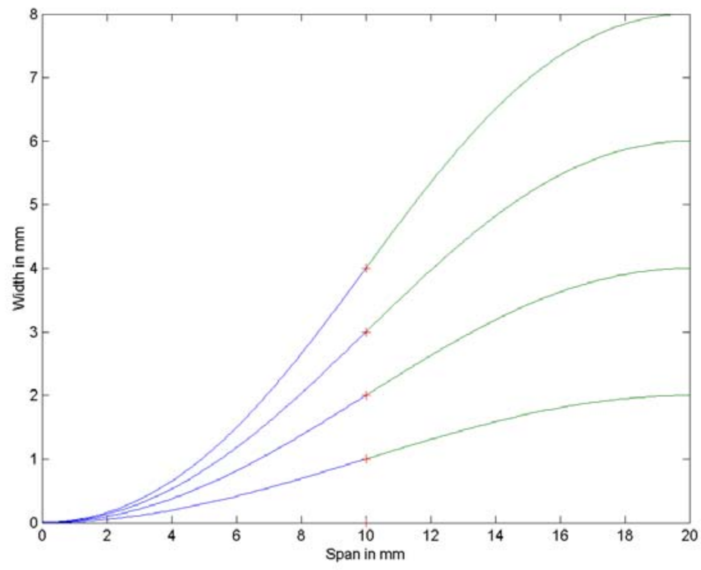

(b) X-Z Plane

Figure 5-5 Wire loop profile on the two dimensional plane

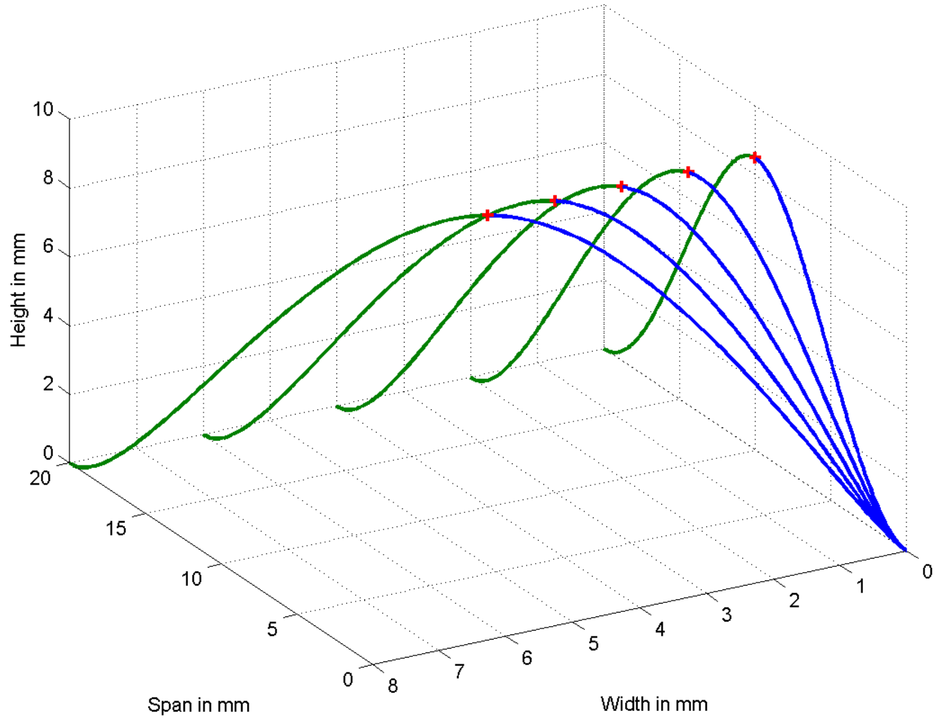

Figure 5-6 Three dimensional wire loop profile

The wire loop heights are maintained constant in all the designs while the length increases gradually as the width offset increases. Figure 5-5 (a), (b) and Figure 5-6 represent the wire profiles in the two-dimensional and three-dimensional planes respectively. It is observed that the curves satisfy the zero slope conditions near the bond pads.

A three-dimensional model of the minimum energy wire profile was built using ANSYS. Due to the presence of the skew-symmetry about the plane Z=W/2 for a non-zero width offset, the whole wire profile had to be modeled (Figure 5-3). A sum of 11905 twenty noded isoparametric hexahedral/brick elements along with 54226 nodes were used for each one of the designs. The wire is relatively thin near the region where it is bonded. The thinning is primarily due to the ultrasonic bonding. Hence, for more accurate modeling, the thinning of the wire along with the wire deformation due to ultrasonic bonding has been modeled. The wire deformation corresponds to 0.1 mm vertical motion of the tool downwards, explained in Section 4.7. Figure 5-7(a) shows the deformed wire profile near the edges. Figure 5-7(b) shows the underside of the deformed wire profile where the wire is ultrasonically welded to the bond pad.

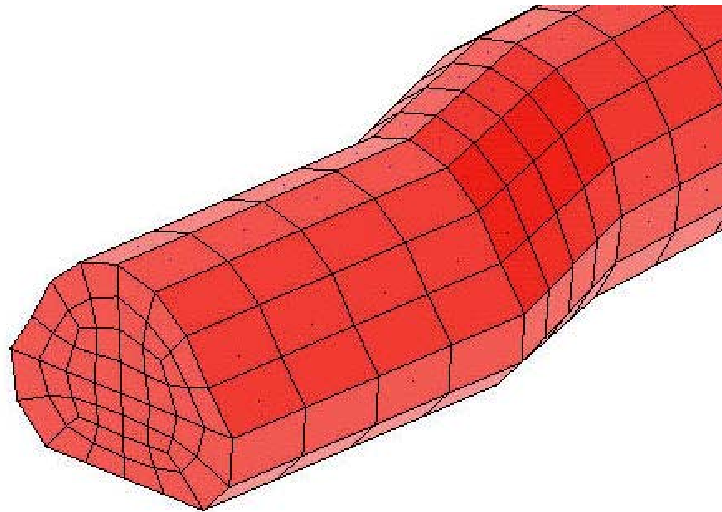

(a) Deformed Profile

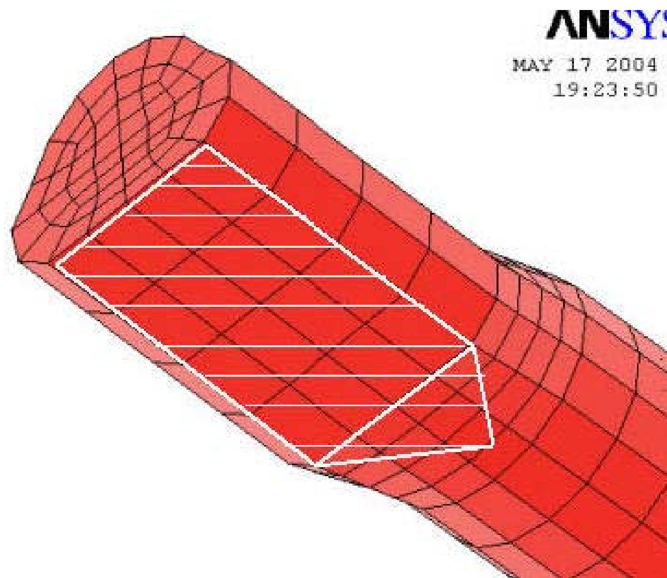

(b) Boundary Conditions

Figure 5-7 Deformed wire profile with boundary conditions

From the theory of beam bending, one would expect maximum bending stresses to occur at the top and bottom sections of the wire. The top section would be in compression while the bottom fibers would be in tension. However, considering the

boundary conditions shown in (Figure 5-7 (b)) the stresses at the bottom of the wire, near the heel, would be much higher in comparison to the top section. The heel near the bottom fibers of the wire (left bond pad) is highly constrained, increasing the stress while the heel near the top fibers of the wire (left bond pad) is surrounded by more compliant material reducing the stress. This has been demonstrated through Figure 5-8 for a wire bonded without a width offset, at the critical location where cracking would be expected to initiate. The maximum stress location was always identified to be at the same location even for wires that are bonded with a width offset. One of the reasons for this behavior was due to the similarity in the boundary conditions in all the problems and the point identified was adjacent to the place where the constraint was applied.

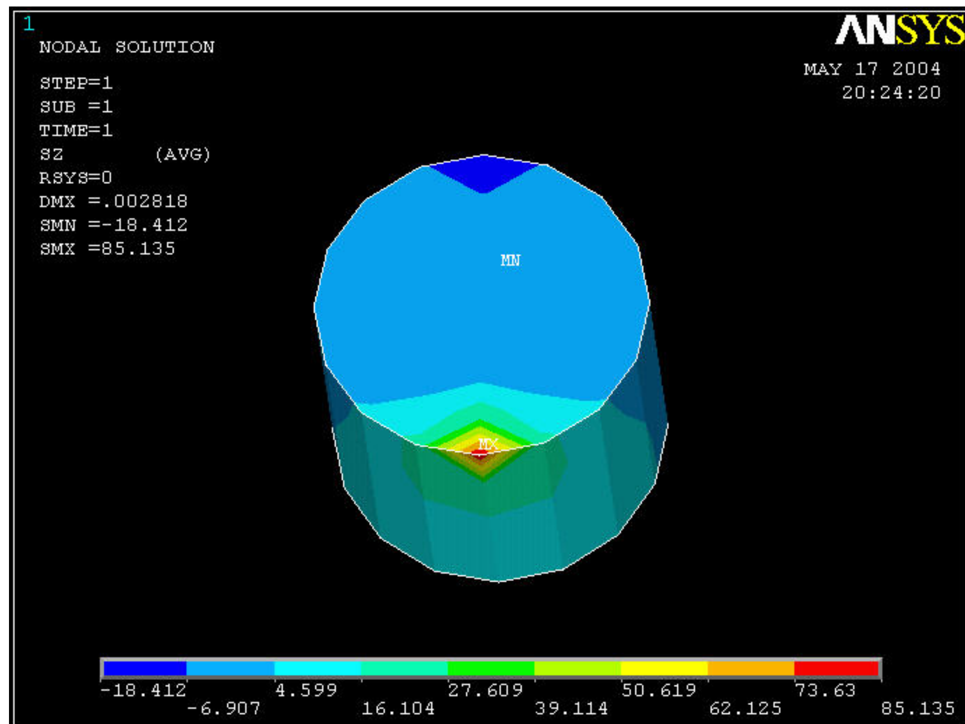

Figure 5-8 Maximum stresses near the heel for a wire with zero width offset

The maximum bending stresses at the heel of the wire have been identified in all the designs and are shown in Figure 5-9. It is very interesting to note that the bending stresses have reduced, though marginally, with the increase in twisting. The primary reason for this behavior is the reduction in the curvature near the heel of the wire with increase in twisting (Figure 5-10).

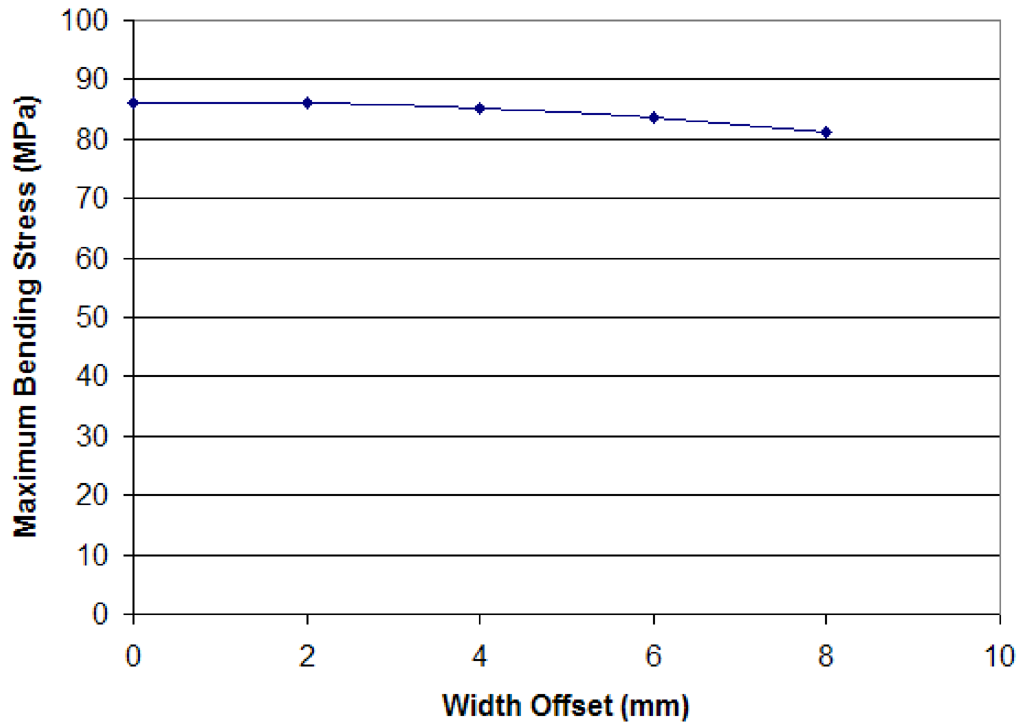

Figure 5-9 Maximum bending stresses at the heel

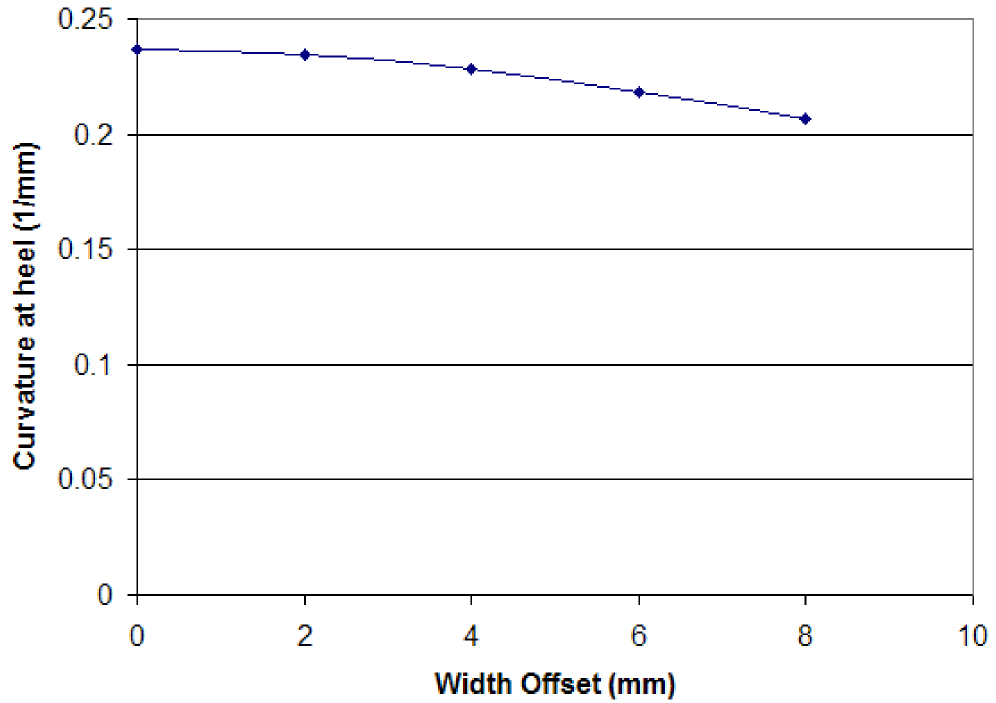

Figure 5-10 Curvature at the heel of the wire

Stresses have been plotted at the top, bottom, left and right sides of the wire along the wire span. This study has been performed primarily to see the effect of wire twisting on the bending stresses. Figure 5-11 shows a cross-section of the wire (the plot shows the normalized wire radius) with 4 points 1, 2, 3 and 4.

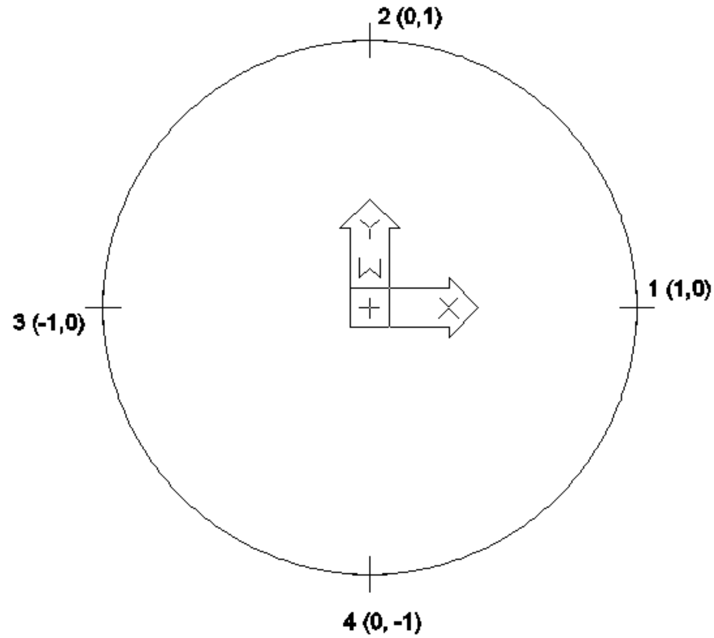

Figure 5-11 Sections of wire where stresses are plotted

If a wire with such a cross section were subjected to thermal cycling, maximum stresses would be observed at points 2 and 4. However, with twisting one would expect stresses to build up at points 1 and 3 also. Also, for any cross-section, away from the heel (twisted configuration), maximum stresses might be marginally offset from these four edges i.e. the neutral plane might not be located on the plane running through 1-3 as proved through the illustrations in Figure 5-12 for a wire, bonded with/without width offset.

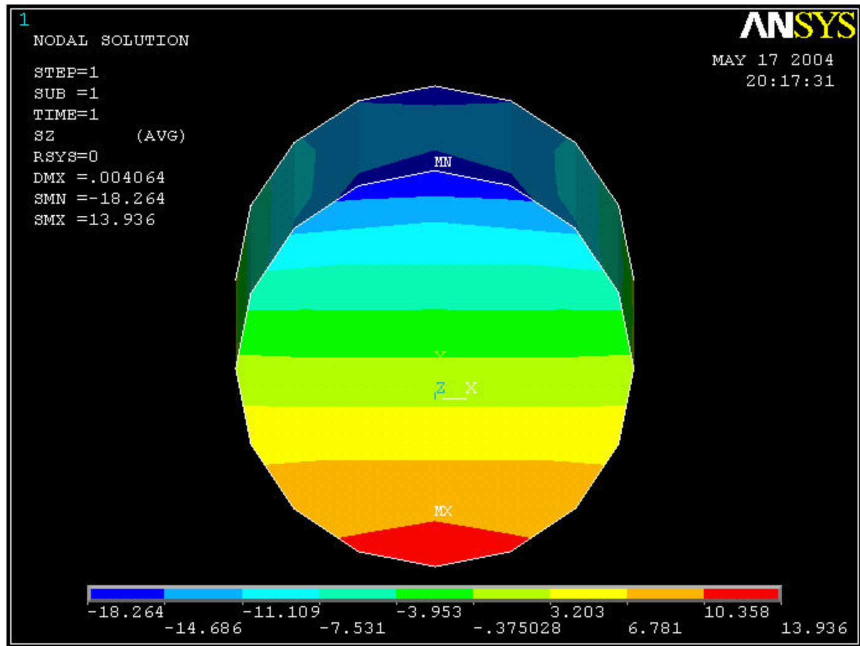

(a) Width offset of 0 mm

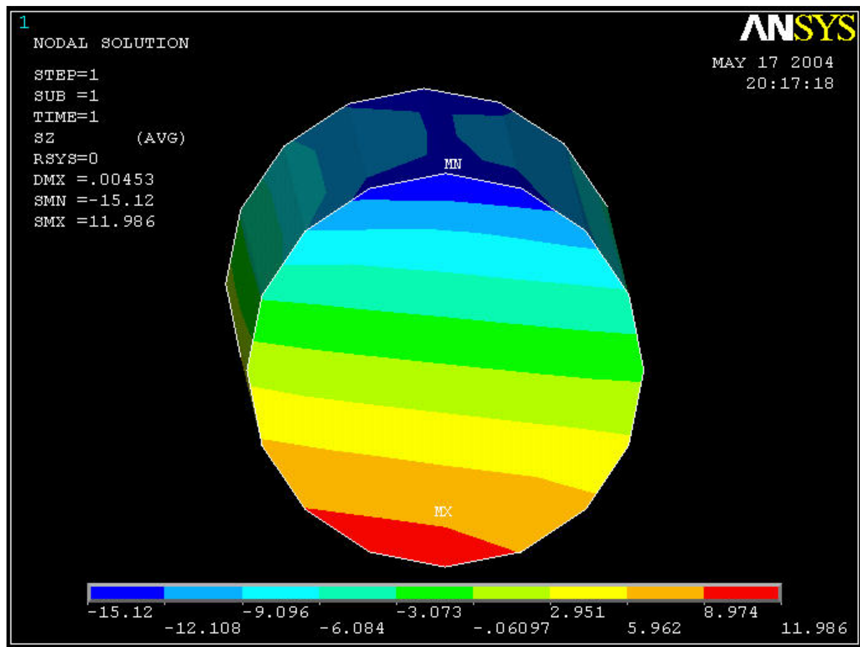

(a) Width offset of 8 mm

Figure 5-12 Stresses at cross section of wire away from the heel

Figure 5-13 and Figure 5-14 show the location of the neutral planes on the wires with and without width offset. The twisting of the neutral plane is observed in the wire bonded with a width offset. The neutral planes have been located using the contour band feature in ANSYS. All the stresses beyond ±0.5 MPa have been shaded gray while the rest of the low stressed regions have been marked with the banded contours.

Figure 5-15 and Figure 5-16 show the stresses at a layer of nodes on the top and bottom of the wire. It is observed that the stress patterns look identical. The bending stresses at the bottom of the wire are seen to fluctuate from a maximum tensile near the heel to compressive at mid span with zero stresses around a span of 15 mm.

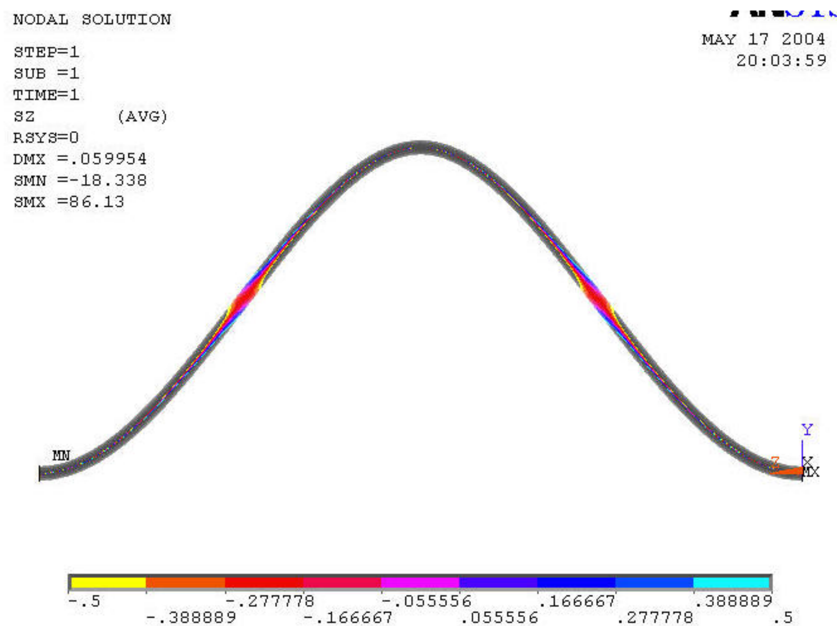

Figure 5-13 Location of neutral plane for width offset 0 mm

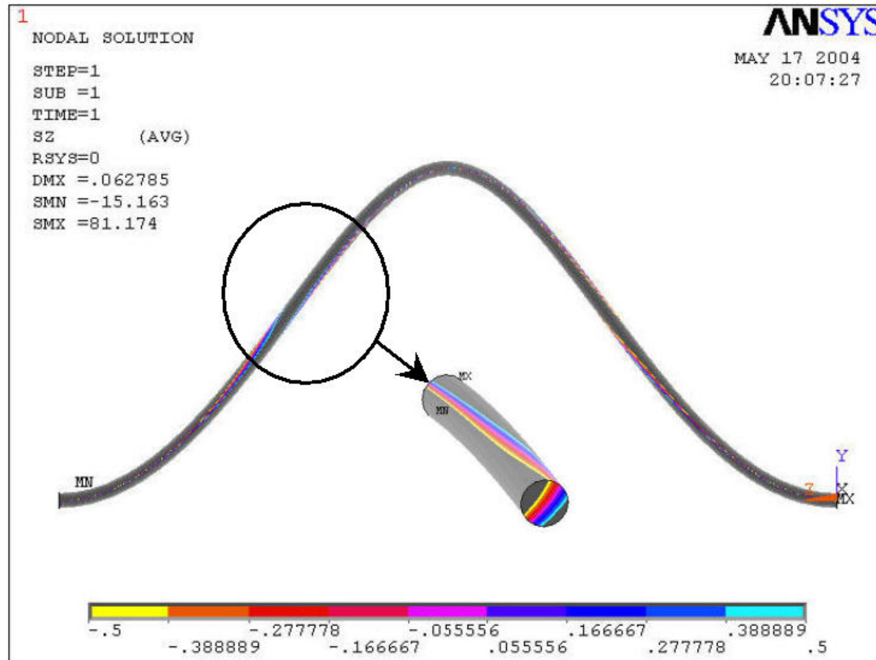

Figure 5-14 Location of neutral plane for width offset 8 mm

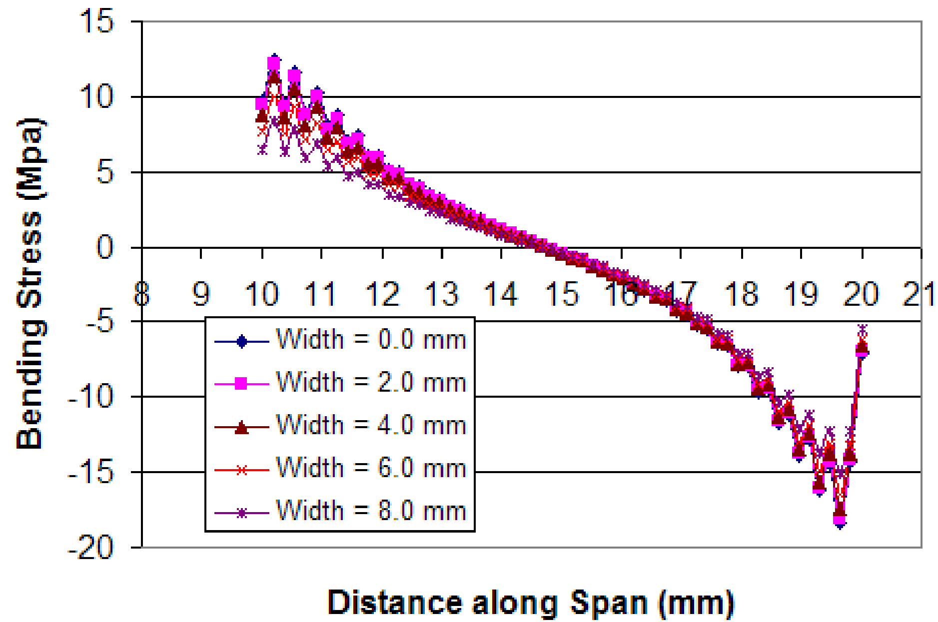

Figure 5-15 Stresses at nodes on the top side of wire

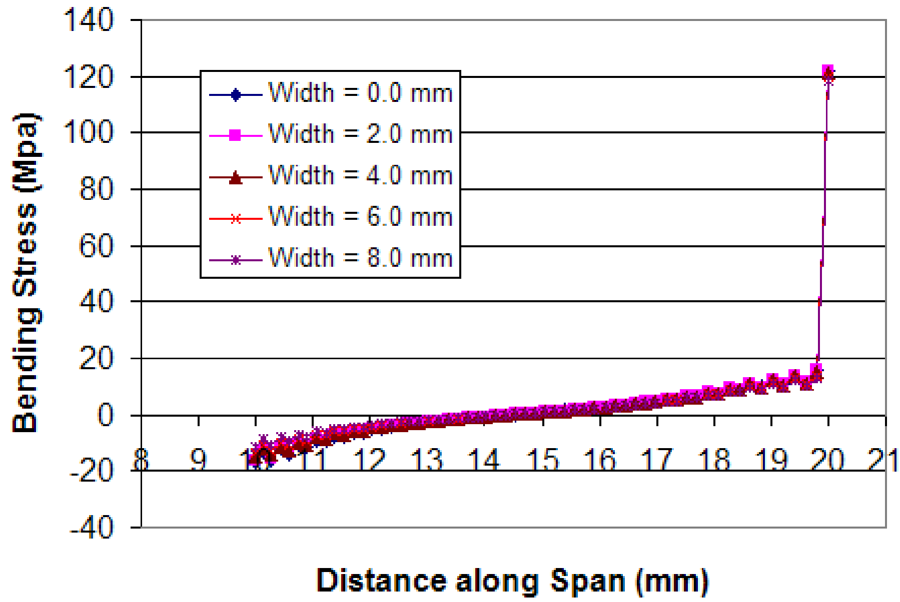

Figure 5-16 Stresses at nodes on the bottom side of wire

However, this trend is not observed for the stresses at a layer of nodes on the left and right side of the wire, shown in Figure 5-17 and Figure 5-18. The stresses are seen to increase with an increase in the amount of twisting. In spite of the stress variation in the left and right sides, the magnitude of the stresses are much lower in comparison to the stresses at the top and bottom sections of the wire. Hence, it can be concluded that the critical failure site is still the heel of the wire where there is insignificant change in stresses due to wire twisting.

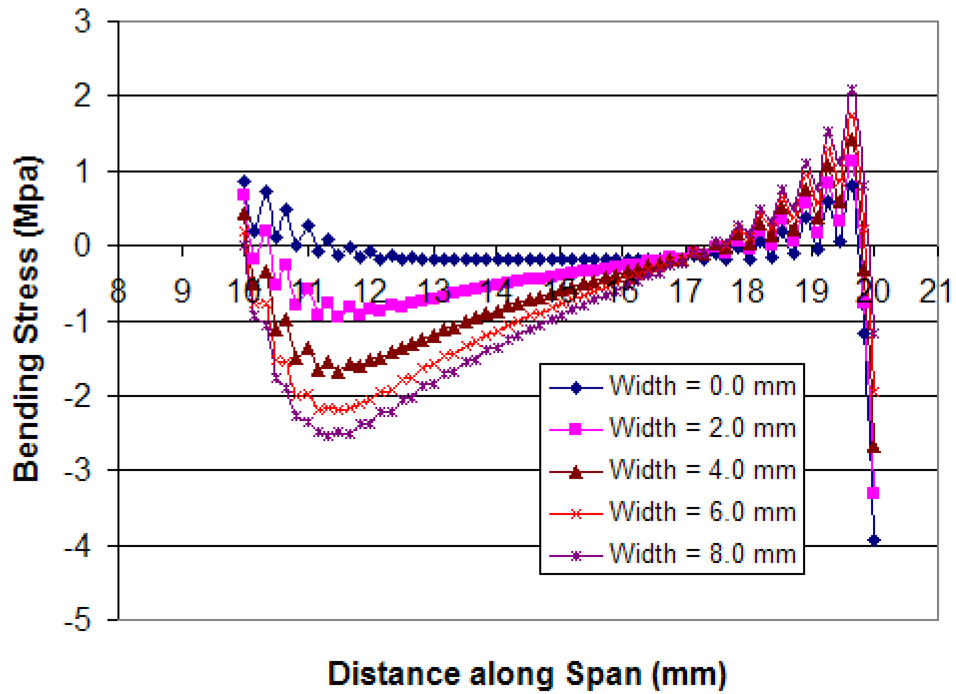

Figure 5-17 Stresses at nodes on the left side of the wire

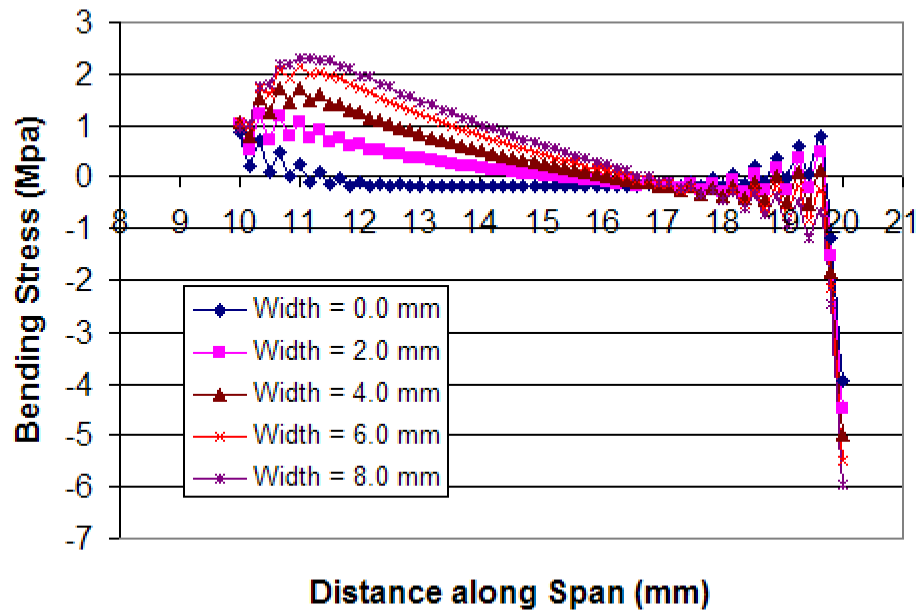

Figure 5-18 Stresses at nodes on the right side of the wire

This study is valid for wires that are bonded to pads that are aligned parallel, but with a width offset. The study reveals that wires, if properly bonded, will not be highly stressed by twisting effects near the heel. However, this model can be made more comprehensive by not imposing the constraint of parallel bond pads. Though one might not experience a drastic reduction in the stresses near the heel, there might be a reduction in stresses in the center of the wire where there is more twisting.

The model provides an approach to determine stresses in wires that are bonded with some width and height offset. The minimum energy wire geometry can be fed into the wirebonder to design reliable wirebonded interconnections regardless of the constraints.

Chapter 6: Contributions and Suggestions for Future Work

The major accomplishments and contributions of this dissertation are summarized in this chapter, along with suggestions for future work.

6.1 Major Accomplishments

The major contributions of this dissertation are listed below,

- The determination of minimum energy profiles for wires. The model predicts the minimum energy profile based on any type of constraints provided. This has been performed for a two dimensional case and a three dimensional case. The determination of the wire loop profile is critical to both finite element modeling as well as for the physics of failure based models. Also, these minimum energy profiles could be fed into the wirebonder for producing reliable wire interconnections.
- Development of a first order physics of failure based model to predict cycles to failure for asymmetrically bonded wires subjected to wire flexural fatigue. The model essentially consists of a load transformation model and a damage model. The load transformation model also includes a frame displacement model that is critical to wire flexural fatigue. The effect of wire thinning near the heel, which is not modeled in the Euler-Bernoulli beam equations are introduced in terms of a stress concentration parameter, K_s. The model developed can be used to assess the

reliability of an existing design i.e. as a good design evaluation tool. In addition, the model can also be used to design reliable wirebonded interconnection.

- A finite element investigation was used to prove the theory of perimeter bonding commonly observed in experiments. Wire deformation due to the wirebonding process was reproduced using finite element simulations. The process parameters that are critical for the wirebonding process are identified. In addition, the effect of wire thinning on the flexural stresses was determined by means of the finite element simulations.
- The effect of wire twisting is high only on regions away from the heel where high stresses are not seen in comparison to the heel stresses. Hence, it was concluded that wire twisting is not critical to the reliability of the wires.

The first order model employs an energy based method approach, using cubic splines, to fit the minimum energy wire profile with wire span, wire length, wire diameter and bond pad height offset as input parameters. The model combines both changes in the wire geometry and changes in frame geometry as a function of temperature cycling to calculate strains in the heel of the wire. The strains are converted to time to failure using elastic and plastic damage models. The damage model has an additional parameter, which accounts for the wire thinning. This stress concentration parameter, has been determined through finite element simulations.

The model can be used in evaluating the reliability for existing designs or also in designing new wirebonded interconnections. As mentioned in the contributions these

minimum energy profiles can be fed into the wire bonder for producing reliable wirebonded interconnections.

Some of the interesting conclusions of the parametric studies for designing reliable wirebonded interconnections are,

- Flexural stresses are low when the wire is thin. This is easily seen through Eq. 2-5. However, from electrical perspective thinner wires will have more resistance and hence more joule heating.
- Increase in height offset of wirebonds would always result in failure happening at the heel of the wire near the upper bond pad, provided the wire is bonded without any manufacturing defect. Hence, the height offset should be minimized as much as possible to circumvent this problem.
- There is an optimum wire length of wire, which can increase the mechanical reliability of the interconnection. The model helps one determine these optimum values. Also, for a wire designed with an optimum wire length, an increase in wire span helps reduce the heel stresses or strains.
- The frame displacements are critical to the wire flexure. Suitable frame properties can help alleviate the issue of high heel stresses.
- Wire deformation, due to wirebonding should be as small as possible in order to reduce the flexural stresses. However, this could lead to a shift in the failure mechanism from wire flexure to wire lift-off.

Based on these conclusions a test case has been considered for building reliable wirebonded interconnection. Based on imposed constraints of length, height and wire span a reliable wirebonded interconnection has been built in the Appendix D.

6.2 Suggestions for Future Work

Some of the suggestions for future work has been suggested in the following sections.

6.2.1 Effect of Wire Heating

The power modules had been subjected to rapid thermal cycling environments where they were exposed to temperature extremes for a short duration of time. The dwell time ensured that the entire wire profile attained a uniform temperature. The wire configuration after thermal cycling, which is needed for the determination of the strains, assumed uniform heating of the wire. However, power cycling causes localized heating in the wire thus causing higher localized temperature excursions, which has been omitted in the current analysis.

6.2.2 Effect of Silicone Gel Encapsulant

Some of the power modules had silicone gel encapsulants in them. The silicone gel used in power modules prevents moisture ingress and protects the die. However, it can inadvertently transfer the stresses onto the wires. Wires that are encapsulated with the

silicone gel are seen to fail much earlier than wires that are free to expand. This was observed through a study done on one of the power modules used in the study (Figure 6-1).

Hence, the model should be modified to include the effect of silicone gel encapsulant.

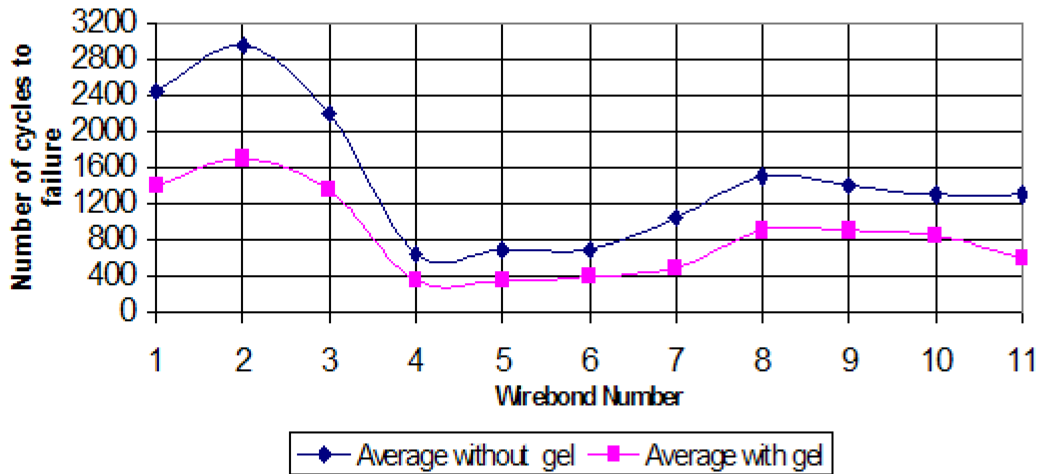

Figure 6-1 Cycles to failure with/without gel

6.2.3 Plastic Deformation of the Wire

For very high thermal cycling load, the wires would experience more plastic deformation and hence it was assumed that the total plastic strains used in the low cycle fatigue model would be approximately equal to the total strains. However, for more accurate modeling, the loading has to be applied in steps, which allows the strains to be decoupled into elastic and plastic strains.

6.2.4 Wire Twisting with no Constraints in the Three Dimensional Plane

The model assumes that the wire profiles are all two dimensional. Any three-dimensional wire profiles are all mapped onto a two dimensional plane. However, several wires are bonded with wire twisting due to constraints imposed on the design. An effort has been made to account for wire twisting in the model.

The model assumes the bond pads are aligned parallel but placed at an offset from one another. This model can be made more comprehensive by not imposing the constraint of parallel bond pads. As proved through the study in Chapter 5, with smooth wire profiles one might not see a drastic reduction in the heel stresses. However, this could prove to be the desired tool for a wirebonder to produce wires that are not improperly stressed at the heel.

6.2.5 Determination of Optimum Wirebonding Process Parameters

The optimum wire bonding process parameters were identified in Chapter 4 as, bonding force, geometry of bonding head, ultrasonic power, and the bonding time. Finite element simulations were performed to better understand the bonding process and also to see the effect of wire thinning on the heel stresses. The process parameters that were considered were, bonding force and the geometry of the bonding head. Future efforts could be directed in quantifying the contact area through the ultrasonic power and bonding time.

6.2.6 Characterization of Wire Material Properties for Low Cycle Fatigue

The fatigue constants are very critical to the damage model. The Basquin's, or the high cycle fatigue constants were determined for the 8-mil and 15-mil wires. However, the experiment could not be conducted for the low-cycle fatigue region since the wires could not be compressed (reduced cross-section). The Basquin's constant were close to the values reported in literature [Suresh, 1992] for annealed aluminum. Hence, the plastic constants used in the model are based on the properties reported in the literature for annealed aluminum [Suresh, 1992]. Considering the fact that the lifetime is based on a power law, it might be more prudent to develop a test setup where the wires can be cyclically loaded plastically in the tensile and compressive regions.

Appendix A

A.1 Frame Displacement Model

During the heating of the module, the frame expands and bows displacing the higher bond pads, thus placing additional strain on the wire. An analytical model has been developed to predict the frame displacements. The displacement due to CTE mismatch can be decoupled into a linear motion of the frame and a bending of the frame.

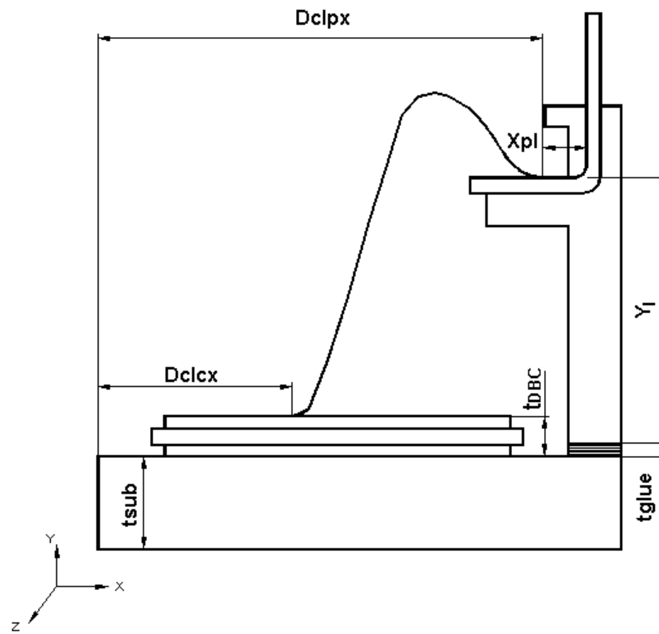

Figure A- 1 Frame geometry parameters

For linear displacement due to the rise in temperature ΔT, the span of the bond wire ($D_{x0} = D_{clpx}-D_{clcx}$) increases by:

$\delta x_1 = D_{x0}\alpha_{sub}\Delta T$ A-1

The bond pad height increases by:

$\delta y_1 = t_{glue}\alpha_{glue}\Delta T + y_1\alpha_{ply}\Delta T - t_{dbc}\alpha_{dbc}\Delta T$ A-2

where α_{sub}, α_{glue}, α_{ply} and α_{dbc} are the thermal expansion coefficients of the power module heat spreader, glue, plastic frame and DBC layers respectively.

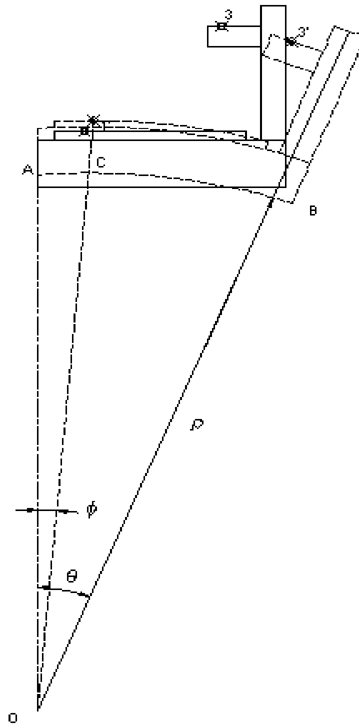

Figure A-2 Bowing of frame

In addition to the linear displacements, the frame also bows during temperature cycling due to the CTE mismatch of the heat spreader and the DBC layers as shown in Figure A-2. The points 1, 3 and 1', 3' shown in Figure A-2 represent the bond points

before and after cooling. The bowing will be significant, considering the length of the heat spreader and substrate and the CTE mismatch between the layers. The bowing in the frame and substrate has been calculated based on the thickness and corresponding material properties of the layers using the method of Timoshenko [Timoshenko, 1925] as applied by Neugebauer [Neugebauer et al., 1986]. The displacement in the center of the bow is given by:

$$Ss = \frac{3\left(D_{clpx} + x_{pl}\right)^2 \left(\alpha_{sub} - \alpha_{dbc}\right)\Delta T}{t_{sub}}(F) \qquad \text{A-3}$$

where,

$$F = \frac{(1+m)}{3(1+m)^2 + (1+mn)\left[m^2 + \frac{1}{mn}\right]} \qquad \text{A-4}$$

$$M = \frac{t_{dbc}}{t_{sub}} \qquad n = \frac{E_{dbc}}{1-\nu_{dbc}} \frac{1-\nu_{sub}}{E_{sub}} \qquad \text{A-5}$$

where, ν is the Poisson's ratio, E is the modulus of elasticity and t is the thickness of corresponding layers. Subscripts "dbc" and "sub" denote the DBC substrate and the heat spreader layers, respectively.

The radius of curvature of bowing of the frame is very large compared to the dimensions of the frame. Also, the bowed frame subtends a very small angle at the center, so the simplifying assumption can be made that $\cos(\theta)=1 - \theta^2/2$; $\sin(\theta)=\theta-\theta^3/6$). From the arc length, AB, shown in Figure A-2, it can be easily proved that,ψ

$$\theta = \frac{2Ss}{\text{Arc Length AB}} \qquad \rho = \frac{\text{Arc Length AB}}{\theta} \qquad \text{A-6}$$

$$\phi = \frac{\text{Arc Length AC}}{\rho} \qquad \text{A-7}$$

The net change in displacements due to bowing is given by:

δx_b=difference in x-coordinate of 3′&1′–difference in x-coordinate of 3&1 A-8

$$=[(\rho+t_{sub}+t_{glue}+y_l)\sin\theta - x_{pl}\cos\theta-(\rho+t_{sub}+t_{dbc})\sin\phi]-[D_{clpx}-D_{clcx}]$$

δy_b=difference in y-coordinate of 3′&1′–difference in y-coordinate of 3&1 A-9

$$=[(\rho+t_{sub}+t_{glue}+y_l)\cos\theta+x_{pl}\sin\theta-(\rho+t_{sub}+t_{dbc})\cos\phi]-[y_l+t_{glue}-t_{dbc}]$$

The displacements shown in Eq. A-1, Eq. A-2, Eq. A-8 and Eq. A-9 take into account the effect of movement of frame due to heating. The new values of D_f and H_f are given by,

$$D_f=D_i+\delta x_b+\delta x_l \qquad H_f=H_i+\delta y_b+\delta y_l \qquad \text{A-10}$$

Appendix B

B.1 Derivation of Wire Loop Profile using a Cubic Spline

The wire profile is represented by means of a cubic spline. The cubic spline has a unique feature of minimizing the strain energy for a given set of interpolating points. The following section would explain the derivation of the wire loop profile using the cubic spline approach.

As mentioned in the thesis earlier, the wire profile is represented by means of two cubic polynomial curves (Curve 1 and Curve 2) with three interpolating points (1, 2 and 3) as shown in Figure B-1.

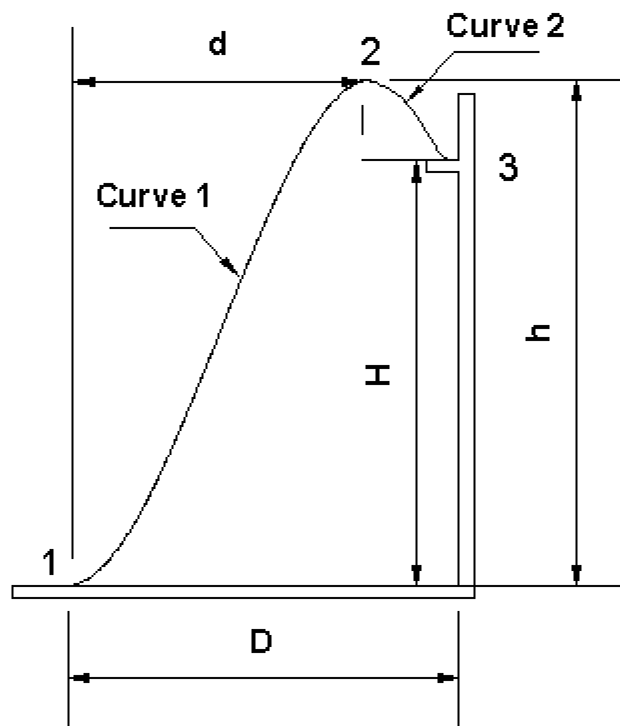

Figure B-1 Wire loop profile parameters

Point 1 and Point 3 are defined by co-ordinates (0, 0) and (D, H) where D and H are the wire span and height offset between the bond pads. Point 2 is the reference point defined by co-ordinates (d, h). A cubic polynomial between a set of two points with co-ordinates (x_0, y_0) and (x_1, y_1) and step size of h_0 can be written in terms of its reference co-ordinates and the slopes as,

$$P_0(x) = L(x) + \tilde{p}(x) \qquad \text{B-1}$$

$$P_0(x) = -\frac{y_0}{h_0}(x - x_1) + \frac{y_1}{h_0}(x - x_0) + \frac{s_0 - \tilde{s}_0}{h_0^2}(x - x_0)(x - x_1)^2 + \frac{s_1 - \tilde{s}_0}{h_0^2}(x - x_1)(x - x_0)^2 \qquad \text{B-2}$$

where s_0 and s_1 are the slopes at the reference points and $\tilde{s}_0$ is the gradient between the reference points. Repeating this procedure for another set of points (x_1, y_1) and (x_2, y_2) the equation for the other cubic polynomial is given by,

$$P_1(x) = -\frac{y_1}{h_1}(x - x_2) + \frac{y_2}{h_1}(x - x_1) + \frac{s_1 - \tilde{s}_1}{h_1^2}(x - x_1)(x - x_2)^2 + \frac{s_2 - \tilde{s}_1}{h_1^2}(x - x_2)(x - x_1)^2 \qquad \text{B-3}$$

The ultrasonic bonding process would enforce a zero slope condition at these points. Hence, s_0 and s_2, the slopes at the points 1 and 3, are given a zero value. Substituting the values for x0, y0, x1, y1, x2, y2, h0 and h1 by the wirebonding parameters, defined in Figure B-1, we get

$$(x_0, y_0)=(0, 0), (x_1, y_1)=(d, h), (x_2,y_2)=(D, H) \qquad \text{B-4}$$

$$h_0=d, h_1=D-d$$

$$\tilde{s}_0 = \frac{h}{d} \quad , \quad \tilde{s}_1 = \frac{H - h}{D - d}$$

The point and slope continuity at points 1, 2 and 3 provides C^1 continuity. A C^2 continuity is enforced by equating the second order derivatives at point 2 through the equation,

$$P_0''(x) = P_1''(x) \text{ at } x=x_1 \qquad \text{B-5}$$

The simplification of Eq. B-5 provides the solution to the unknown slope at point 2, i.e. the value of s_1 as,

$$s_1 = \frac{3}{2}\left[\frac{(H-h)d}{D(D-d)} - \frac{(d-D)h}{dD}\right] \qquad \text{B-6}$$

Applying the boundary conditions, the equations of the two curves defining the wire profile are given by,

$$P_0(x) = \frac{hx}{d} - \frac{\frac{h}{d}x(x-d)^2}{d^2} + \frac{S_1 - (\frac{h}{d})}{d^2}(x-d)x^2 \qquad \text{B-7}$$

$$P_1(x) = \frac{h(x-D)}{d-D} + \frac{H(x-d)}{D-d} + \frac{S_1 - \left(\frac{H-h}{D-d}\right)}{(D-d)^2}(x-d)(x-D)^2 - \frac{H-h}{(D-d)^3}(x-D)(x-d)^2 \qquad \text{B-8}$$

The curvatures at any point on the curve, defined by y=f(x), is given by,

$$\kappa = \frac{y''}{\left(1+y'^2\right)^{3/2}} \qquad \text{B-9}$$

Considering the fact that the slope, $y'$is zero at the reference points 1 and 3, the equation for the curvature at the reference points is given by,

$$\kappa = y'' = \frac{6h}{d^2} - \frac{2S_1}{d} \ @\ (0,0) \tag{B-10}$$

$$\kappa = y'' = \frac{\left[2(D-d)S_1 - 6(H-h)\right]}{(D-d)^2} \ @\ (D, H) \tag{B-11}$$

Appendix C

C.1 Simple Cubic Spline Model

The energy-based cubic spline model is an iterative solver, which runs on the Levenberg-Marquardt algorithm for solving a set of non-linear equations. In addition, the solver also makes use of numerical differentiation and integration. These steps help us obtain the best location of reference point 2 where the wire would store minimum potential energy. The main purpose for using a simple analytical model is lost if the computation time is very high. Hence, a series of tests were performed to study the patterns of reference point 2, based on various input bond parameters.

C.1.1 Location of Reference Point in Wire Geometry

The cubic spline would plot the best wire shape with minimum energy for a given reference point 2. The energy-based model goes a step further in locating the best reference point 2 on the domain, which would further reduce the energy of the curve. There are several minima's in the domain chosen and it is important to choose a good guess value for the solver for a quicker convergence. For a wire bonded without any height offset the reference point is always located in the middle of the wire span. Figure C-1 and Figure C-2 show the reference point locations for varying wire lengths and varying bond height offsets respectively. When the wire lengths are varied it is observed that the reference point tries to shift towards the mid-span whereas for a higher bond offset the point shifts towards the right bond pad. It is difficult to capture the trend in

terms of a single equation relating the wire lengths, height and the wire span simultaneously. However, a careful observation of the Figure C-1 and Figure C-2 reveals that the reference point is always located very close to the stationary point (point where the slope switches signs). Therefore, for the quicker version of the model, the reference point 2 is chosen where S_1 given in Eq. 2-12 is equal to zero.

$$\frac{(H-h)d}{D-d} = \frac{(d-D)h}{d} \quad \text{C-1}$$

Further simplification of Eq. C-1 along with the admissible solution provides the following relationship between d and h,

$$d = \frac{Dh}{H}\left[1-\sqrt{1-\frac{H}{h}}\right] \quad \text{C-2}$$

This gives the user the flexibility to provide the loop height if the wire lengths are not known. If the loop height, h, is provided the model determines d using Eq. C-2. If the wire length is provided, Eq. 2-17 along with Eq. C-2 can be used to determine the values of d and h.

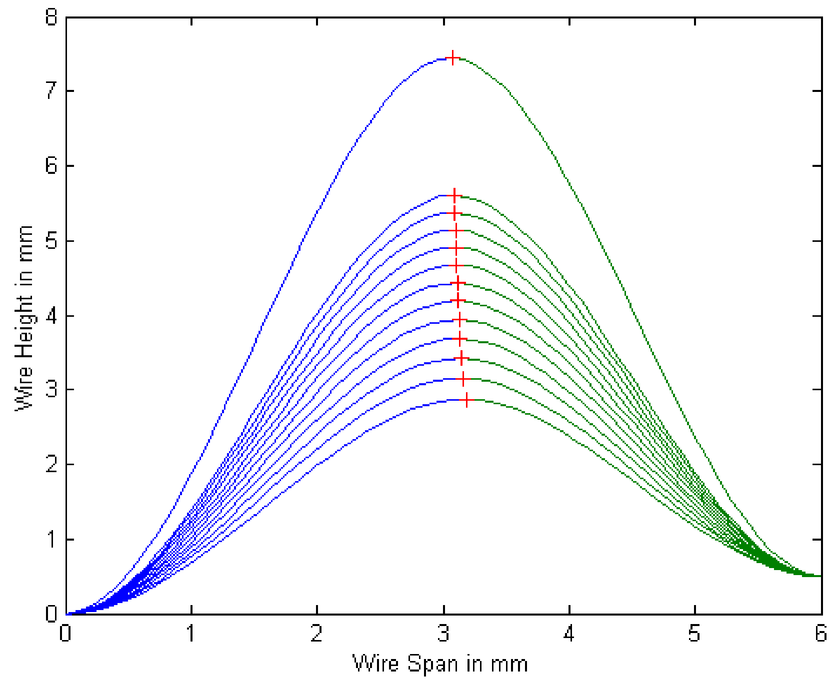

Figure C-1 Location of reference point for varying wire lengths

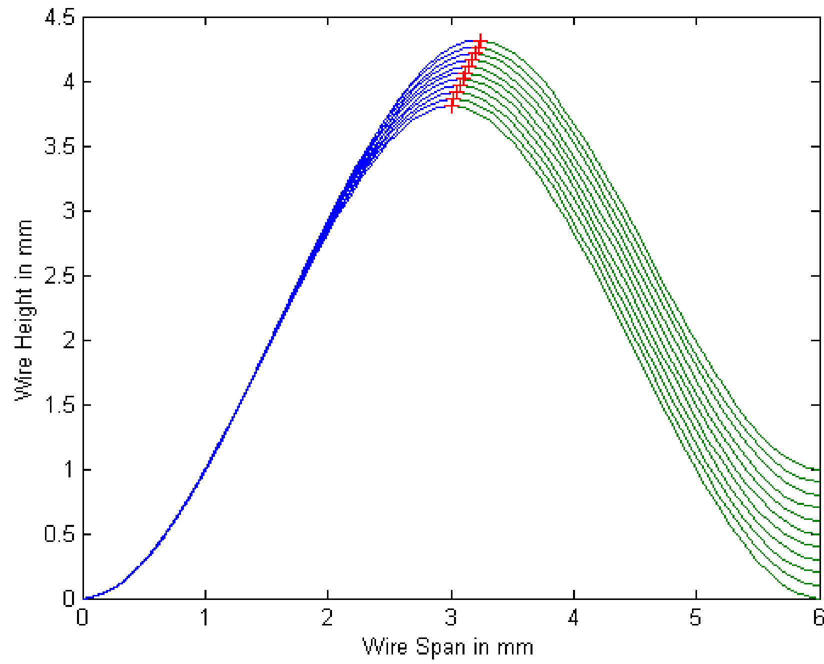

Figure C-2 Location of reference point for varying bond height offsets

The simpler version of the model assumes that the reference point 2 is located at the highest point, i.e. the point defining the loop height. Using the fact that S1 is equal to zero, the curvatures at points 1 & 3 after simplification are given are given by,

$$\kappa_{low} = \frac{6h}{d^2} \quad , \quad \kappa_{high} = \frac{6(h-H)}{(D-d)^2} \qquad \text{C-3}$$

It is quite interesting to note that these are precisely the same equations derived in the case of a hermite polynomial but for the fact that a second order continuity has been forced into these equations. Hence, it is sufficient to provide either the wire length or the loop height of the wire. This is quite unlike the hermite polynomial model where the reference point had to be provided (the x and y co-ordinates of point 2). This could be the reason for the sensitivity of the model to the location of reference point.

The curvature shown in Eq. C-3 is a good indication of what the strains would be on the critical section of the wire. For a non-zero height offset, using Eq. C-2 and Eq. C-3 the curvature of the wire in the heel near the lower bond pad is given by,

$$\kappa_{low} = \frac{6H^2}{D^2 h\left(2h - H - 2\sqrt{h^2 - Hh}\right)} \qquad \text{C-3}$$

Another very interesting behavior to be noted from Eq. C-3 is that an increase in span reduces the strains in the wire. This is the reason for the trend observed in Figure 3-11.

Appendix D

D.1 Modeling a Reliable Wirebonded Interconnection

This section explains the utility of the model as a design tool in developing reliable wirebonded interconnection. The objective of the current study would be to determine the optimum set of input parameters that can produce reliable wirebonds. Effects of wire twisting and wire thinning near the heel would be ignored. It is assumed that the optimum bond force, power and bonding time have been used to produce very strong bonds. The critical parameters that are considered for the study are,

- Wire Length
- Height Offset of bond pads
- Wire Span
- Wire Diameter

D.1.1 Imposed Constraints

As mentioned in the conclusion section of the dissertation, the wire diameter should be as small as possible to minimize the wire flexure problem. However, considering the applications and power ratings the wire diameter has been chosen to be15 mil (or 381 μm). The design of the power module prevents a zero height offset of the wirebonds. However, there is a maximum and minimum bound for each parameter, listed in Table D-1.

Table D-1Upper and lower bounds of geometric parameters

	Minimum (mm)	Maximum (mm)
Wire Span	8	12
Height Offset	3	5.5
Wire Length	18	22

D.1.1 Wire Flexural Stresses

When exposed to a temperature load cycle the wire flexes building stresses in the heel section. As mentioned in the dissertation earlier, the upper bond pad is always susceptible to higher magnitude of stresses whenever there is a bond pad height offset. Hence, only the flexural stresses at the upper bond pad would be plotted for various input parameters.

Figure D-1 shows the stress contours for various wire lengths and wire span for a wire bonded with a height offset of 3.0 mm. The stress contours suggest that the maximum span and a wire length of 12 mm and 18 mm produce the least flexural stresses (or the maximum cycles to failure).

Figure D-2 shows the stress contours for various height offsets varying from 3 mm to 5 mm in steps of 0.5 mm. As explained in the dissertation earlier, an increase in the height offset increases the flexural stresses at the upper bond pad.

The optimum set of parameters that can produce the maximum reliability for the current study has been identified to be a span of 12 mm, length of 18 mm and a height offset of 3 mm.

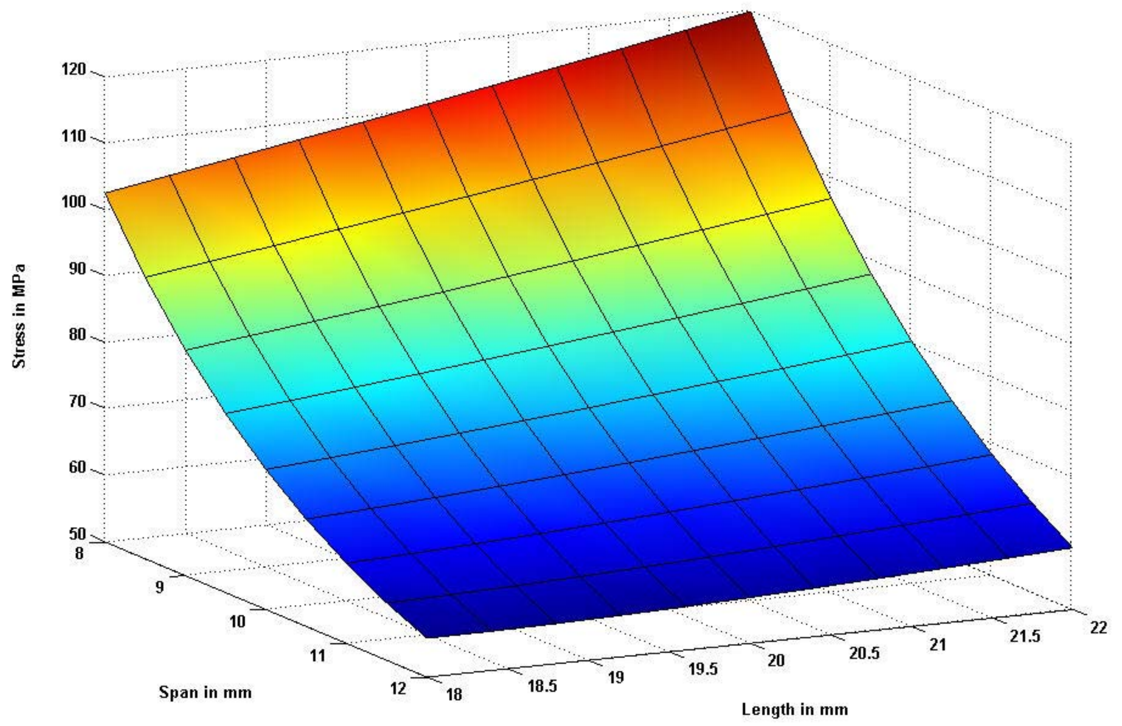

Figure D-1 Flexural stress for height offset of 3 mm

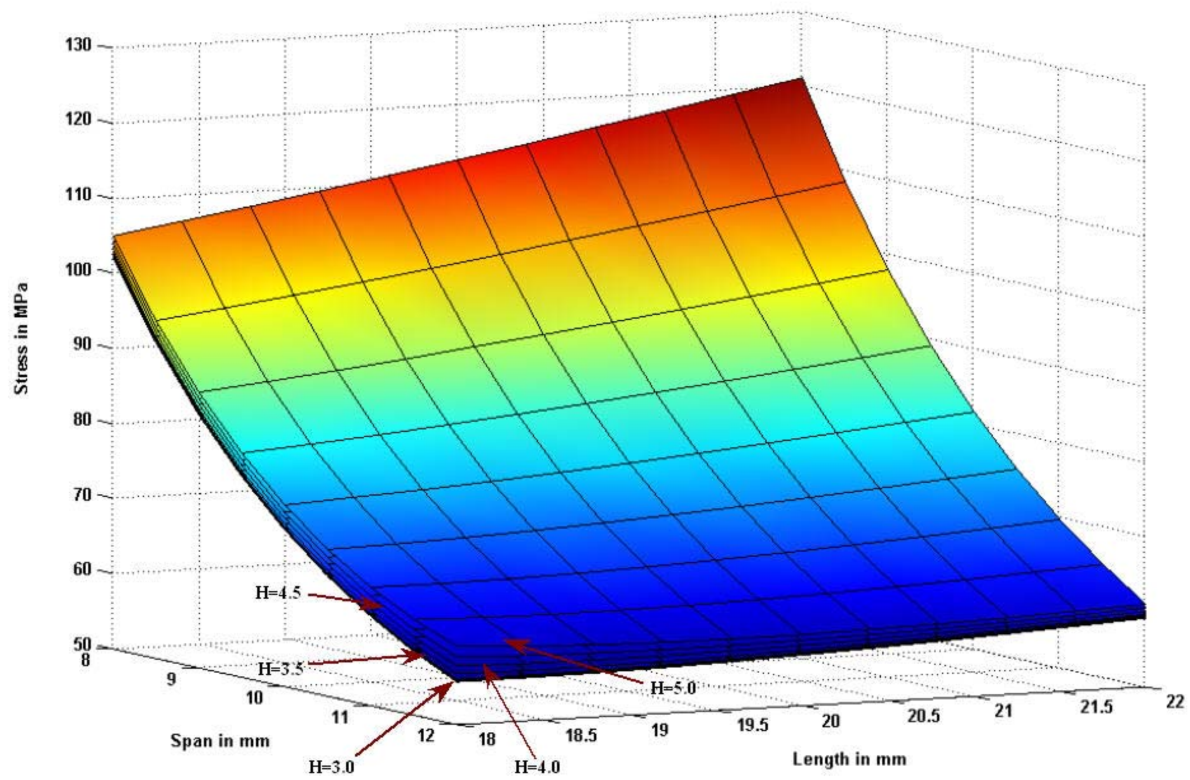

Figure D-2 Flexural stresses for various height offsets

References

1. Pecht, M., Handbook of Electronic Packaging, Marcel Dekker Inc., 1991

2. Yoshino, Y., Ohtsu, H., Shibata, T., “Thermally Induced Failure of Copper-Bonded Alumina Substrates for Electronic Packaging”, Journal of American Ceramic Society, Vol. 75, No. 12, pp. 3353-57, 1992

3. Mikkelsen, J., “Failure Analysis on Direct Bonded Copper Substrates after Thermal cycle in different Mounting conditions”, PCIM 2001 Europe, Nuremberg, Germany.

4. Chidambaram, N. V., "A Numerical and Experimental Study of Temperature Cycle Wire Bond Failure", CHMT/IEEE Conference, pp 877-882, May 13-15, 1991.

5. Harman, G., “Wire Bonding in Microelectronics Materials, Processes, Reliability and Yield”, Second Edition, McGraw Hill, 1997.

6. Chandrasekaran, A., “Effect of mold compound on Au-Al wirebond-bondpad intermetallic formation”, Masters Thesis 2004, University of Maryland-College Park

7. Large Wire bonding tools Catalog, Small Precision tool (SPT), Revised 02-96-3, 1996

8. Kulicke and Soffa, “Bonding Wire Products Catalogue”, 2003

9. Held, M., Jacob, P., Nicoletti, G., Scacco, P., Poech, M. H., “Fast Power Cycling Test for Insulated Gate Bipolar Transistor Modules in Traction Applications”, International Journal of Electronics, Vol. 86, No. 10, pp. 1193 – 1204, 1999.

10. Pecht, M., “A Corrosion Rate Equation for Microelectronic Die Metallization”, International Journal for Hybrid Microelectronics, Vol.13, No.2, p41-52, 1990.

11. Ramminger, S., Wachutka, G., “Wire Bond Failures in Power Modules”, Proceedings of the IMECE’03, Washington DC, Nov 15-21, 2003

12. Hu, J. M., Pecht, M., and Dasgupta, A., “A probabilistic approach for predicting thermal fatigue life of wire bonding in microelectronics”, Journal of Electronic Packaging, Vol. 113, pp 275-285, 1991.

13. Ravi, K. V., and Philofsky, E. M., ”Reliability Improvement of Wire Bonds Subjected to Fatigue Stresses,” 10th Annual Proceedings IEEE Reliability Physics Symposium, pp. 143-149, 1972

14. Pecht, M., Dasgupta, A., and Lall, P., “A failure prediction model for wire bonds”, ISHM proceedings, pp 607-613, 1989.

15. Ramminger, S., Seliger, N., Wachutka, G., “Reliability Model for Al Wire Bonds subjected to Heel Crack Failures”, Microelectronics Reliability, Vol. 40, pp 1521-1525, 2000.

16. Meyyappan, K., McCluskey, P., Hansen, P., "Wire Flexure Fatigue Model for Asymmetric Bond Height", InterPACK'03, Jul 6-11, 2003.

17. Spath, H., "Spline Algorithms for Curves and Surfaces", Utilitas Mathematica Publishing Inc, 1974.

18. Carl de Boor, "A Practical Guide to Splines- Revised Edition", Springer, 2001.

19. Meyyappan, K., McCluskey, P., Hansen, P., "Wire Fatigue Models for Power Electronic Modules", IMECE 2003, Washington DC, Nov 15-21, 2003

20. Manfredo P. Do Carmo, "Differential geometry of curves and surfaces", Prentice Hall, 1976

21. Suresh, S., "Fatigue of Materials", Cambridge University Press, 1992

22. Rowland, E. S., "Effect of Residual Stress on Fatigue", Proceedings of the 10th Sagamore Army Materials Research Conference, New York, pp. 229-244, Aug 13-16, 1963

23. Fox, A., "Effect of Temperature on Stress Relaxation of Several Metallic Materials", Proceedings of the 28th Sagamore Army Materials Research Conference, New York, pp. 181-203, Jul 13-17, 1981

24. The Aluminum Association, "Aluminum Standards and Data", New York, 1968

25. Coffin, L. F., “A study of the effects of cyclic thermal stresses on a ductile metal”, Transaction of the ASME, Vol. 76, pp 931-950, 1954

26. Manson, S. S., “Behavior of materials under conditions of thermal stress”, National Advisory Commission on Aeronautics: Report 1170, Cleveland: Lewis Flight Propulsion Laboratory, 1954

27. Deyhim, A., Yost, B., Lii, M. J., Li, C. Y., “Characterization of the fatigue properties of bonding wires”, Electronic Components and Technology Conference, pp 836-841, 1991

28. Crispi, F. J., Mailing, G. C., Rzant, A. W., “Monitoring Microinch Displacements in Ultrasonic Welding Equipment”, IBM Journal of Research and Development, 1972, pp 307-312.

29. Wilson, A. D., Martin, B. D., Strope, D. H., “Holographic Interferometry Applied to Motion Studies of Ultrasonic Bonders”, IEEE Transactions on Sonics and Ultrasonics, Vol. SU-19, No. 4, pp. 453-461, Oct 1972

30. Dushkes, S.Z., “A design Study of Ultrasonic Bonding Tips”, IBM Journal of Research and Development, Vol. 13, No. 3, pp. 230-235, May 1971

31. Joshi, K. C., “The Formation of Ultrasonic Bonds Between Metals”, IBM Journal of Research and Development, Welding Journal, pp 840-848, Dec 1971

32. Harman, G., Leedy, K. O., "An experimental model of the microelectronic ultrasonic wire bonding mechanism", 10th Annual proceedings Reliability Physics Symposium, pp. 72-77, 1972

33. Langenecker, B., "Effects of Ultrasound on Deformation Characteristics of Metals", IEEE Transactions on Sonics and Ultrasonics, Vol. SU-13, No. 1, Mar 1966

34. Hayes, G. A., Shyne, J. C., "The influence of Ultrasonic Energy on Kinetic Processes in Solids", IEEE Transactions on Sonics and Ultrasonics, Vol. SU-16, No. 2, pp. 68-75, Apr 1969

35. Krzanowski, J. E., "A Transmission Electron Microscopy Study of Ultrasonic Wire Bonding", IEEE Transactions on Components, Hybrids and Manufacturing Technology, Vol. 13, No. 1, Mar 1990

36. Ohga, K., "Failure Analysis of Bonding Wires in Power Transistor Modules", 17th International Symposium for testing & Failure Analysis, Los Angeles, CA, pp. 237-247, 11-15 Nov, 1991.

37. Wu, W., Held, M., Jacob, P., Scacco, P., Birolini, A., "Investigation on the Long Term reliability of Power IGBT Modules", Proceedings of the 7th International Symposium on Power Semiconductor Devices and ICs, Yokohama, pp. 443-448, May 23-25, 1995.

38. Harman, G., Albers, J., “The Ultrasonic Welding Mechanism as Applied to Aluminum and Gold Wire Bonding in Microelectronics”, IEEE Transactions on Parts, Hybrids and Packaging, Vol. PHP-13, No. 4, Dec 1977

39. Ultrasonic Bonding Wedges Catalogue, Small Precision tool (SPT), Revised 08-99-6, 1999

40. Takahashi, Y., Shibamoto, S., Inoue, K., “Numerical Analysis of the Interfacial Contact Process in Wire Thermocompression Bonding”, IEEE Transaction on Components, Hybrids and Manufacturing Technology, Part A, Vol. 19, No. 2, Jun 1996

41. Qin, I. W., Bereznycky, P., Doerr, D., "Wedge Bonding for Ultra Fine Pitch Applications," Proc. Advanced Packaging Technologies Seminar, SEMICON Singapore 2001

42. Timoshenko, S., “Analysis of Bi-Metal Thermostats”, Journal of Optical Society of America, Vol. 23, pp. 233-55, 1925

43. Neugebauer, C. A., Yerman, A. F., Carlson, R. O., Burgess, J. F., Webster, H. F., and Glascock, H. H., “The Packaging of Power Semiconductor Devices”, Gordon and Breach Science Publishers, Vol. 7, 1986

44. Jeon, I., Chung, Q., Hong, J., Byun, K., “The Effect of Ultrasonic Power on Bonding Pad and IMD Layers in Ultrasonic Wire Bonding”, IEEE International Symposium on Electronic Materials and Packaging, pp 235-242, 2001

45. Popov, E. P., “Engineering Mechanics of Solids”, Prentice-Hall Inc., 1998